Tailoring Optical and Thermal Properties of Nanostructured Materials for Passive Radiative Cooling

by

Hannah M. Kim

A dissertation submitted in partial fulfillment
of the requirements for the degree of
Doctor of Philosophy
(Chemical Engineering)
in the University of Michigan
2021

Doctoral Committee:

Assistant Professor Andrej Lenert, Chair
Professor Nicholas Kotov
Associate Professor Jeff Sakamoto
Associate Professor Anish Tutej

Hannah M. Kim

hanmkim@umich.edu

ORCID iD: 0000-0003-2885-4377

Dedication

This dissertation is dedicated to my amazing family for their love and support, and to my friends who have been a source of joy and encouragement.

Acknowledgments

My Ph.D. is a journey that has involved the support of numerous people. I would like to take this opportunity to express my gratitude to everyone who has contributed to the successful completion of my Ph.D. I would especially like to further recognize certain people who have made a noticeable impact to help me accomplish this extraordinary milestone.

First and foremost, I would like to thank my advisor, Andrej Lenert for accepting me as his first graduate student in his research group. His mentorship and guidance over the years have played a vital role in my growth as a researcher and individual. Andrej was always available when I needed help and has supported me to think critically and creatively. I am confident that I will continue to use the skillsets I developed working with Andrej well after graduate school.

To the members of the Lenert lab, Tobias Burger, Sean McSherry, Alex Hill, Zach Berquist, and Bosun Roy-Layinde, it has been an absolute pleasure and privilege to have worked with you all. It is amazing to see how our friendship has grown over the years and I will forever cherish the conversations and memories that we share. You all have played a critical role in my personal development and as a researcher. Thank you for all the times you have made me laugh, for cheering me up when I was down, and for being there when I needed help. I will miss working with you all, but our friendship will continue long after our time as graduate students has ended.

I would also like to recognize others outside the Lenert lab who have influenced my research journey. Thank you, Dr. Regina Garcia-Mendez (former Sakamoto member), for mentoring me my first year and being someone who I could rely on while I was figuring out how to set up a new lab and project. Thank you to all my other committee members, Professors Kotov, Sakamoto, and Tuteja, for your encouraging words, feedback, and support. Thank you to the staff workers at the Lurie Nanofabrication Facility (LNF) and Michigan Center for Materials Characterization (MC2) who trained and helped me on the instruments essential for my Ph.D. work. Thank you to the Chemical Engineering support staff, especially Kelly Raickovich, for helping me with numerous orders and organizing and scheduling events. Thank you to Susan Hamlin who assisted me and countless other graduate students in navigating the Ph.D. requirements.

I would like to recognize all my amazing friends who have brought joy into this memorable journey. To my Ann Arbor friends, I cannot fully express what your friendship has meant to me over the years. You were all there to cheer me on when things got tough, and you were there to celebrate when a milestone was reached. I cannot imagine this part of my life without you in it, so my Ph.D. work is dedicated to you all. To my lunch squad, sharing meals and conversations with you all was easily the best moments of my day. I would also like to thank the friends I made working with student organizations including the Optics Society at the University of Michigan (OSUM), Chemical Engineering Graduate Society (ChEGS), and Graduate Christian Fellowship (GCF). There are so many others who I would like to mention, but the list would be too long. To

my friends, thank you for your friendship up to this point, and I look forward to many more conversations, laughter, and activities with you all.

Lastly, I would like to convey my deepest gratitude to my parents and brother. Mom and Dad, you have always motivated me to be the best version of myself and to use my talents to benefit others. Your unconditional love and encouragement were an essential source of energy to get me through the toughest times. Thank you for all your sacrifice and for being my greatest inspiration. To my brother, thank you for being my role model and for always giving me advice when I needed it. You have supported me in so many ways throughout my life and I am so proud to be your sister. My family members are the most important people in my life, so this work is dedicated to them and the role they played in supporting my Ph.D. journey.

Table of Contents

List of Figures

List of Tables

Abstract

Passive radiative cooling has emerged as a promising way to reduce the amount of primary energy used for cooling. Specifically, cities could use passive radiative cooling to mitigate both urban heat island issues and electricity demand for air conditioning, which accounts for about 10% of electricity use in the U.S. according to the EIA. Decreasing energy consumption also plays an essential role in addressing global warming. For example, retrofitting 80% of commercial roofs in the U.S. could potentially reduce annual energy use by greater than 10 TWh and offset CO_2 emissions by about 6 Mt. "Passive radiative" refers to the concept of selectively emitting thermal radiation to Space through the "atmospheric window" (*i.e.*, $8 - 13$ µm) without the input of energy. Low atmospheric absorption (high transmission) in this wavelength band allows objects to directly radiate heat to outer space. This effectively uses Space (~3 Kelvin) as a heat sink, which enables sub-ambient cooling. For example, nighttime cooling is a common phenomenon for high emitting materials. On the other hand, daytime cooling is particularly challenging because solar heating on Earth is ~10 times greater than the heat emitted to outer space, but by designing materials to reflect sunlight and emit in the infrared, sub-ambient cooling during peak solar hours is achievable. This dissertation includes a discussion on the optical and thermal properties needed for daytime cooling and demonstrates the cooling performance with outdoor measurements. In addition, background information, radiative cooling mechanisms, and past works are presented.

This dissertation primarily focuses on materials with specific characteristic length scales that scatter solar radiation and enable emission in the infrared. First, the radiative and thermal transport

of three candidate materials (BaF$_2$, ZnS, and Polyethylene) with low absorption in the atmospheric window was modeled to predict the cooling performance of a nanoporous insulating layer. Physical morphology, intrinsic optical properties, and volume fraction are used as inputs to simultaneously solve the heat and radiative transfer equations and output the temperature profile of the nanoporous layer. This model offers a framework for radiative transport of nanoporous systems for potential design optimization. Polyacrylonitrile (PAN) nanofibers were fabricated and the scattering and transmission properties were investigated for electrospun fibers that feature spherical, ellipsoidal, and cylindrical morphologies. The nanofiber morphology was tailored by varying the polymer solution concentration used for electrospinning. The resulting PAN films (nanoPAN) with ellipsoidal morphologies achieve a solar reflectance ~95% while retaining >70% transmittance in the atmospheric window. These nanoPAN films can be paired with any emitting surface to promote radiative cooling, and outdoor measurements demonstrated a 50°C temperature reduction during the day when paired with a blackbody emitter compared to the blackbody control. The unique morphology and size distribution of PAN nanofibers can also be combined with existing radiative cooling emitter designs to further enhance the solar reflective properties. The addition of nanoPAN to a specularly reflective emitter enhanced the solar reflectance from 97% to 99% to more closely mimic nighttime radiative cooling conditions during the day. A ~5°C stagnation temperature and ~30 W/m^2 cooling power enhancement were observed during peak solar hours. Overall, the work presented in this thesis demonstrates the ability to tailor the optical and thermal properties of nanostructured materials to achieve passive radiative cooling.

Chapter 1: Introduction

1.1 Motivation

Before modern refrigeration systems, ancient Persian civilizations (~400 BCE) built "ice pits" where a shallow pool of water exposed to the open night sky would undergo passive radiative cooling.[1] This was done by losing heat to outer space through thermal emission, enabling ice formation. Modern passive radiative cooling systems utilize the same principles as the ice pits but seek to achieve cooling during the daytime to minimize energy used for thermal management.

The field of passive radiative cooling has become more prominent over the last decade as an energy-efficient and low-carbon alternative for cooling and a potential approach for directly mitigating global warming itself. Passive radiative cooling is defined as the ability to dissipate heat via thermal radiation without energy consumption. This dry and passive approach, as well as the diversity of materials used for radiative cooling, opens opportunities for personal, regional, and global cooling applications (Fig. 1.1). Rapid urbanization has posed a challenge of meeting increased electricity demands using renewable energy sources. However, energy management and reducing current energy use are just as important to achieving a sustainable future. Specifically, increasing demand for air conditioning, especially in countries with rapidly developing economies,[2] is leading to more global warming and local heating of urbanized areas known as "heat island effects".[3] Urban heat island effects are exacerbated by man-made materials that retain heat and are used to construct buildings, roads, and other infrastructure. Studies predict that the

demand for building cooling will be three times as high by 2050, at which point, 2/3 of all households will own an air conditioner.[2] While in developed countries (*e.g.*, U.S.) air conditioning alone can account for over 30% of residential electricity consumption during peak summer hours.[2] As a result, implementation of passive radiative cooling systems can significantly reduce peak electricity demand,[4] alleviate issues associated with urban heat island effects,[5,6] and reverse temperature rises due to global warming.[7] Passive radiative cooling has the potential to address these issues and provide cooling while reducing or eliminating energy consumption.

Personal Comfort   Urban Heat Island Effect   Global Warming
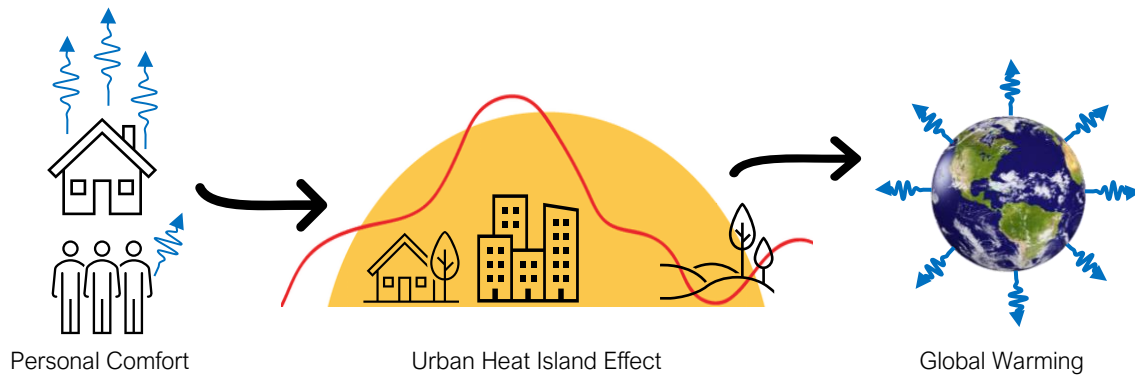
Figure 1.1. Applications for passive radiative cooling can vary in scale from personal comfort of individuals and homes, mitigating localized regional heating in urban and suburban areas, and reversing global warming.

1.2 Radiative Cooling Mechanism

The electromagnetic (EM) spectrum categorizes EM radiation into bands depending on the magnitude of their wavelength. Solar radiation ranges from approximately 0.25 – 3 μm and is comprised of the ultraviolet, visible, and near infrared bands (Fig. 1.2a,b). "Heat" (*i.e.*, thermal radiation) is primarily associated with the infrared region and ranges from 3 – 20 μm in wavelength (Fig. 1.2b). The Earth emits infrared photons to outer space, which is considered a heat sink due to its cold temperature. Some of these emitted photons are absorbed by the molecules that make

up the Earth's atmosphere, including nitrogen, oxygen, carbon dioxide, water, methane, ozone, etc. The absorption that occurs from these molecular bonds results in infrared opacity. In these regions, the absorption by the atmosphere gives rise to the greenhouse effect. However, in regions where the atmosphere does not absorb (*i.e.*, is transparent), heat from the Earth is rejected to outer space. This natural energy balance is what enables the Earth to be habitable to life. The "atmospheric transparency windows" are regions where thermal radiation is not absorbed by the atmosphere. The clarity of the atmospheric window is dependent on environmental conditions such as cloud coverage and humidity, where low clarity will reduce the potential for heat exchange with outer space.[8]

Passive radiative cooling is a naturally occurring phenomenon that enables the cooling of objects on the Earth's surface by using outer space as a heat sink. Passive radiative cooling can be described as a "reverse" greenhouse effect (Fig. 1.2c). The more familiar greenhouse effect occurs when the solar radiation incident on the Earth is absorbed by the molecules that make up the atmosphere. For objects to take advantage of passive radiative cooling, they must block the competing effects of solar heating through reflection with heat rejection by emission. In space, the standard solar spectrum can be approximated using the AM0 which has an integrated power of 1366.1 W/m^2. For terrestrial applications, the AM1.5G spectrum for flat plates is used and integrates to 1000 W/m^2 (Fig. 1.2a), and the heat rejected from the surface of the Earth to outer space via the atmospheric window is ~ 100 W/m^2. Since the work presented in this thesis focuses on cooling applications on the Earth's surface, the AM1.5G spectrum is used for any modeling scenarios. For a clear sky day, the magnitude of incident solar radiation depends on the solar angle (*i.e.*, location and seasons). Some of the radiation is reflected off the Earth while a portion is

absorbed by the atmosphere. If the Earth is now considered the heat source, it also radiates heat as a blackbody following Planck's law into outer space in regions where the atmosphere is transparent. The key to daytime radiative cooling is to emit heat to space while preventing absorption from solar radiation.
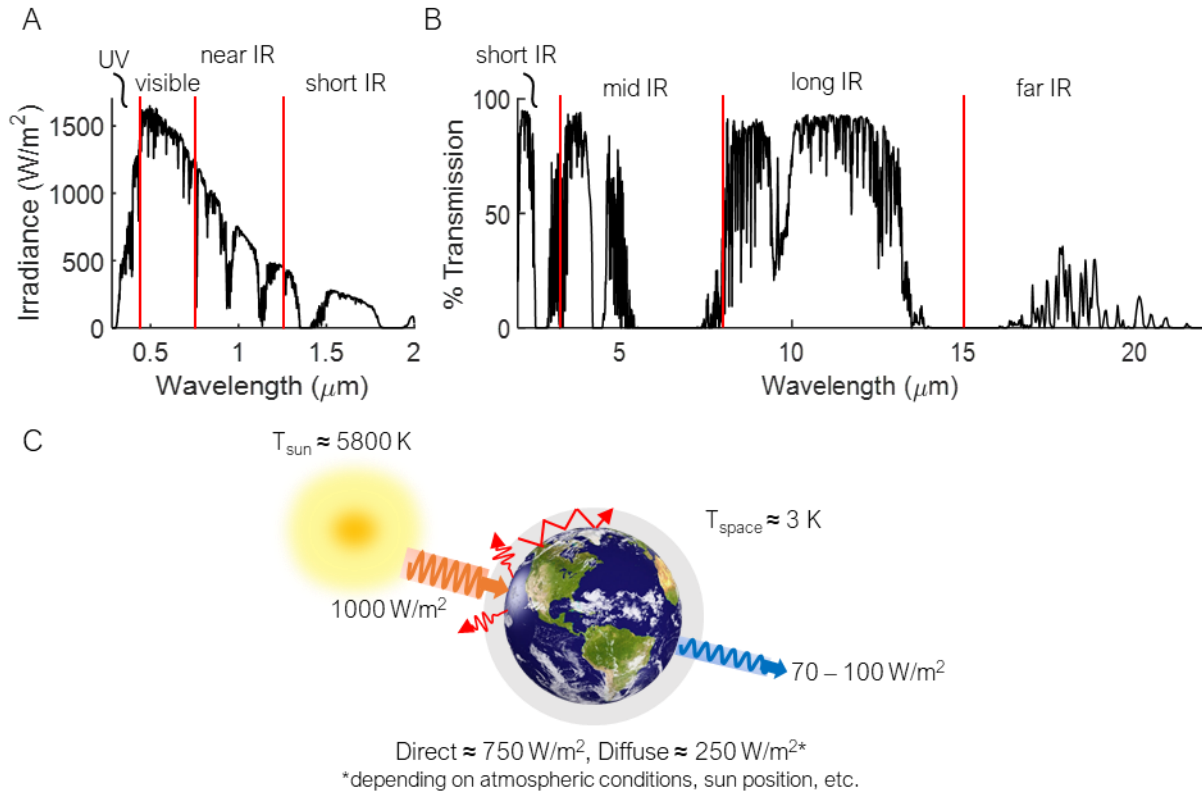
Figure 1.2. The electromagnetic spectrum concerning daytime radiative cooling is comprised of the (A) solar and (B) infrared (IR) regions. The solar spectrum is comprised of the UV, visible, and portions of the IR. The atmospheric windows are defined by the regions of transparency in the IR. (C) Opacity in the IR region is what enables the greenhouse effect while areas of transparency allow heat to be rejected to outer space.

An example is nighttime cooling that results in dew formation in desert and arid environments. Achieving sub-ambient daytime cooling is exceptionally more difficult due to heating from solar radiation. As a result, understanding and designing materials with high solar reflectance while

maintaining heat exchange with outer space is essential for daytime passive radiative cooling. This requires insight into the optical properties of materials ranging from the ultraviolet to the infrared regions of the electromagnetic spectrum. This thesis will focus on understanding interactions of micro/nanoscale materials to achieve spectral selectivity and thermal management concentrating on applications for cooling and energy management.

1.3 Solar Properties

99% of the solar spectrum given by the AM1.5G standard ranges from 300 nm – 3000 nm in wavelength. As such, materials with high reflectance in this range are required to minimize solar heating for daytime cooling. As seen in Fig. 1.2a, the solar spectrum is comprised of three relevant bands of the electromagnetic spectrum: ultraviolet (100 – 400 nm), visible light (400 – 700 nm), and infrared (>700 nm). Depending on atmospheric conditions, sun position, etc., ~85% of the irradiance can be from direct radiation compared to ~15% from diffuse radiation.[9] For a one sun concentration, the peak irradiation occurs at ~500 nm. However, since solar radiation extends into the IR region, it is essential to block both the short-wavelength (higher energy) and longer wavelength (lower energy) portions of the spectrum up to ~3 μm. The broad reflectance of a material can be assessed using the total solar reflectance weighted by the AM1.5G spectrum, which will be abbreviated as SR.[10] The "total solar reflectance" in this case refers to the specular and diffuse reflectance of a material across the solar spectrum. The SR is calculated by the following equation:

$$SR(\%) = \frac{\int I_{sol} R_{eff} \, d\lambda}{\int I_{sol} \, d\lambda} \qquad \text{(Eq. 1.1)}$$

Where I_{sol} is the AM1.5 solar irradiance, R_{eff} is the total reflectance of the material of interest (*i.e.*, emitter or cover), and λ, is the wavelength.

1.4 Specular vs. Diffuse Reflectance

Reflectance can be broadly categorized as specular or diffuse reflection. Specular reflection typically occurs on smooth surfaces where the light reflects with a definite angle, such as mirrors (Fig. 1.3a). Diffuse reflection occurs on rough or textured surfaces where the trajectory of light deviates to all directions, which is also commonly referred to as scattering (Fig. 1.3b). Materials with high solar scattering properties will visibly appear as opaque white surfaces, which is favorable for outdoor applications due to reduced glare. Both methods of reflection can be used to mitigate solar heating, however, the overall device must also be designed with infrared emissivity necessary for heat exchange with outer space.
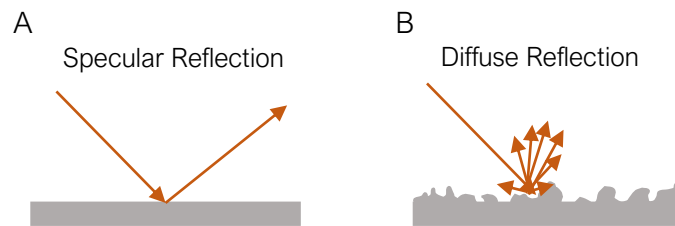
Figure 1.3. (A) Specular reflection occurs on smooth mirrored surfaces while (B) diffuse reflection occurs on rough surfaces.

1.5 Sub-Ambient vs. Near Ambient Radiative Cooling

The emitted spectral radiant flux (*i.e.*, irradiance) of a blackbody (BB) surface at a given temperature can be approximated using Planck's law.[11,12] For near ambient temperatures (~300 K), a BB will emit primarily in the visible and infrared regions. Since a BB absorbs all incident radiation, it will also have high emissivity power across the spectral range. This follows Kirchhoff's law of thermal radiation that states the amount of radiation absorbed by a surface

equals the emission at thermal equilibrium. In addition to absorption, incident light on an object can also be either reflected or transmitted where the total absorbed, reflected, and transmitted radiation sums to 100% ($100\% = Abs. + Ref. + Trans.$). For radiative cooling, a material with low reflectance in the infrared is desired.

In contrast to having high emissivity across the infrared spectrum, sub-ambient temperatures can be reached by selectively emitting radiation in the atmospheric transparency windows ($3.4 - 4.1$ and $8 - 13$ μm) to outer space (~3 K).[3,13] The Earth's atmosphere has low absorption over these wavelength bands, allowing heat to radiate through the atmosphere and directly into space. Net cooling is achieved when the emitted radiation to outer space is greater than the energy absorbed from the ambient surroundings. Modes of parasitic heating include absorbed atmospheric and solar radiation. These contributions decrease the overall cooling power, and therefore, should be minimized to enable high cooling power and low temperatures.[11,14]

The following example illustrates the impact of selective radiative heat transfer on cooling performance and motivates the need for a spectrally selective radiator if cooling at sub-ambient temperatures is desired. A cooling power curve is a tool that is used to illustrate and compare the cooling performance of various approaches. For a blackbody emitter at 290 K (Fig. 1.4a), high cooling power is achieved due to the broad emission across the infrared spectrum, however, sub-ambient temperatures may not necessarily be reached due to the absorbed radiation from the atmosphere. In contrast, for a radiator that preferentially emits in wavelength bands of high atmospheric transparency (*i.e.*, when radiative exchange is restricted to the $8 - 13$ um band) the emitted radiation is greater than the absorbed radiation (Fig. 1.4b), resulting in sub-ambient

cooling. Figures 1.4c,d further illustrates that an "ideal" emitter that selectively emits in the atmospheric windows can achieve lower temperatures than an emitter that broadly emits across the IR.
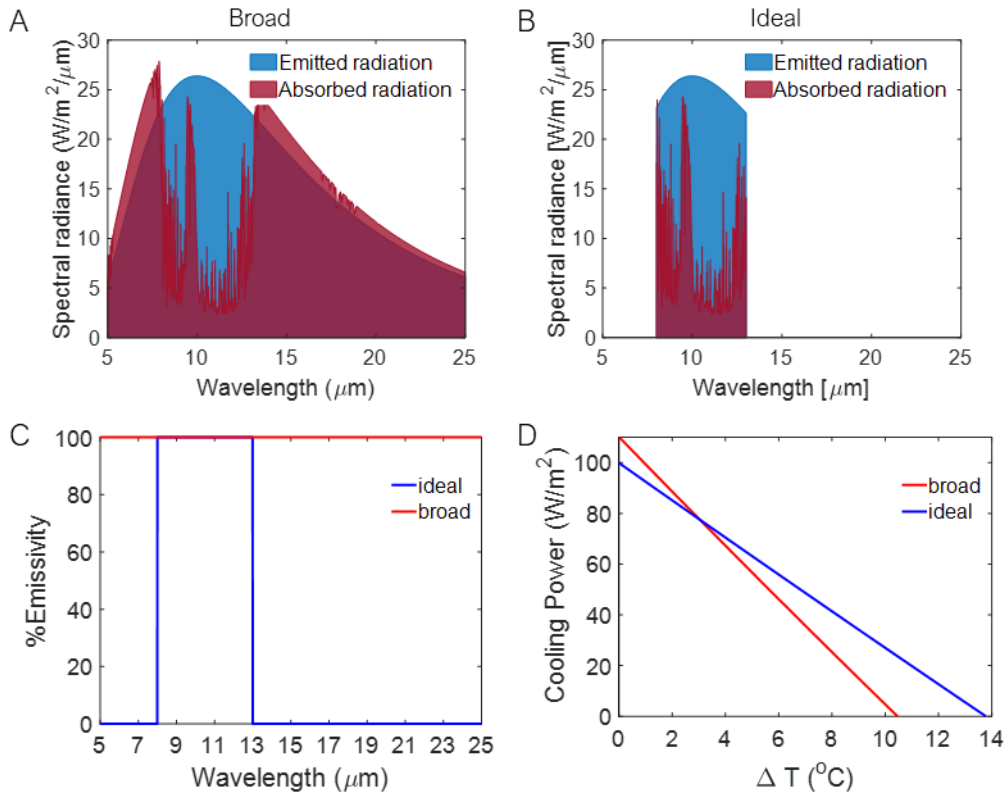
Figure 1.4. (A) Spectral radiance of broadband blackbody emitter at 290K compared to (B) an ideal emitter that selectively emits in the $8 - 13$ μm atmospheric window. (C) and (D) illustrate the cooling performance of a broad versus ideal emitter with a heat transfer coefficient of 5 $W/m^2/K$ and no solar absorption.

1.6 Components of Passive Radiative Cooling Systems

A simple and effective way to block direct solar radiation is to use a directional approach by shading the emitter.[15] Typically, highly reflective materials such as polished metal are used in either a stationary or tracking configuration to shade the emitter.[14–16] Solar shades are effective in blocking sunlight, however, there can be drawbacks if the shading material restricts the view of

the emitter to the open sky. In addition, sunshades become impractical for large-scale applications, so other ways of blocking solar radiation are needed.

Passive radiative cooling systems are primarily comprised of three components: (1) emitter, (2) IR transparent insulating layer, (3) convective cover (Fig. 1.5).
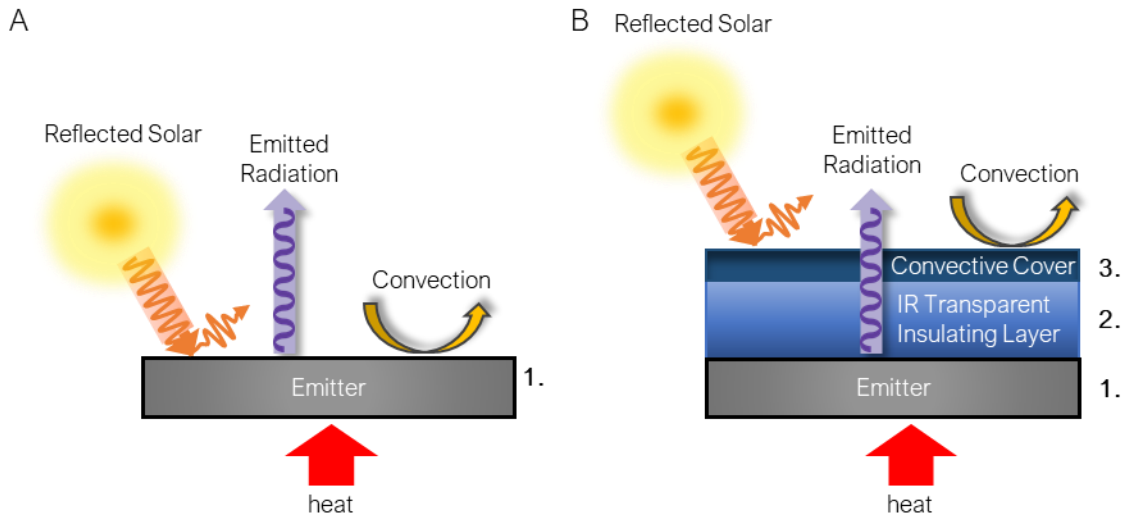
Figure 1.5. (A) A radiative cooling emitter can be designed to directly reflect solar radiation. (B) The use of an IR transparent insulating layer and/or convective cover spatially decouples the emitter from solar heating.

1.6.1 Emitters

Emitters are designed to have high emissivity throughout the atmospheric windows and generally require conduction of heat between the emitter and object to be cooled (Fig. 1.5a).[17] The first reported device that demonstrated sub-ambient cooling under direct sunlight consisted of a photonic design of alternating layers of HfO_2 and SiO_2 on a silver mirror.[18] The emitter boasted a solar reflectance of ~97% while simultaneously having an average emittance of 60% in the 8 – 13 μm band, enabling a daytime temperature reduction of 5°C below ambient.[18] Since then, daytime passive radiative cooling has generated a growing amount of interest.[11,19–24] Significant progress

has been made in developing emitters using active emitting materials including PDMS,[25,26] other polymers (*e.g.*, TPX[27,28], P(VdF-HFP),[29,30] PET/ECDL pairs with ECDEL,[31,32] and cellulose[33,34]), oxides (*e.g.*, alumina,[35] silicon dioxide,[36–38] silicon dioxide embedded in nanofibers,[39,40] hafnium dioxide[18]), phosphates,[41] nitrides,[14] carbides,[42] alternating germanium and aluminum layers,[43] and various paint formulations.[44–46] One disadvantage with selective emitters is its direct exposure to solar radiation (Fig. 1.5a) which results in parasitic heating. As such, stringent requirements of high solar reflectance are essential to maintain daytime cooling power.

1.6.2 IR Transparent Insulators

IR transparent insulators can be used to minimize both radiative and non-radiative heating from the surrounding (Fig. 1.5b). The insulating layer has a low thermal conductivity and is transparent in the infrared to enable radiation from the bottom emitter to reach the open sky. These layers range from airgaps, to vacuum, and nanoporous systems. Although airgaps are the simplest to implement, it provides low radiative resistance. The first reported daytime radiative cooling setup in 2014 included an airgap to insulate their emitter, and since then, has been the most common way to reduce atmospheric heating.[18] A vacuum layer can also significantly reduce atmospheric radiation and parasitic heat loss to enable low stagnation temperatures, however, maintaining low pressure is impractical and requires energy to operate the vacuum pump.[14] Nanoporous materials can be tailored to achieve low thermal conductivities while also scattering solar radiation. The complexity of using nanoporous insulators is designing materials that are both visibly opaque and IR transparent.[47] Leroy et al. developed polyethylene aerogels with low thermal conductivities of 28 mW/mK while maintaining IR transparency to mitigate parasitic heating of the emitter and

enable high cooling performance.[48] As such, pairing an IR transparent insulator with an emitter is beneficial for sub-ambient and near-ambient cooling, which is further discussed in chapters 2-3.

1.6.3 Convective Covers

Convective covers are placed over the emitting surface and spatially decouples convective heating of the emitter (Fig. 1.5b). Like IR transparent insulators, convective covers must be transparent in the atmospheric windows to allow heat transfer between the emitter and outer space. The convective cover can also serve a dual purpose of blocking solar radiation if designed to be opaque in the solar region. This decoupling allows heating to occur at the cover rather than the emitter, enabling higher cooling powers.[10] Convective covers predominantly rely on conventional IR window materials such as chalcogenides,[49,50] but the most common materials used are thin polyethylene (PE) films (*i.e.*, plastic wrap).[17,51,52] The simple chemistry of PE $(C_2H_4)_n$ means that absorption peaks only occur for $C-H$ and $C-C$ bonds, resulting in high transmission in the IR. In particular, recent approaches have focused on porous PE to act both as a convective cover and scatter solar radiation.[17,48,53,54] Nevertheless, the choice of materials used for convective covers remains limited compared to radiative cooling emitters.

1.7 Cooling Performance Sensitivity to Solar and Atmospheric Gain

The cooling power is plotted as a function of emitter temperature (or change in emitter temperature relative to the ambient) and is a function of the emitter optical properties, ambient temperature, solar irradiance, atmospheric clarity, and non-radiative environmental conditions. The temperature when cooling power is equal to zero is referred to as the stagnation temperature.
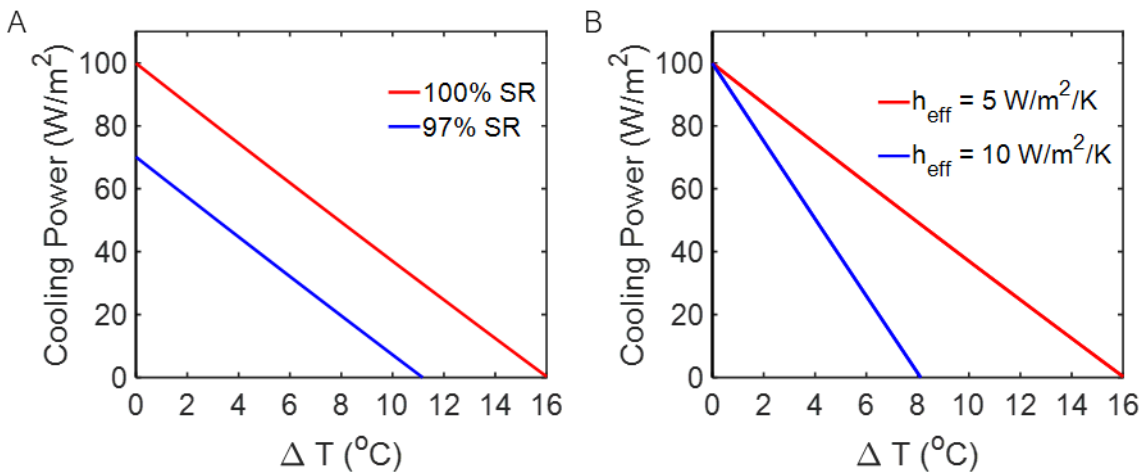
Figure 1.6. (A) Compares the drop in cooling power when the solar reflectance is reduced by 3%. (B) Illustrates the effects of heat transfer coefficient (*i.e.*, insulation) on the achievable stagnation temperature. The emissivity of the emitters was assumed to be ideal in the 8 – 13 μm range for this sensitivity analysis and the ambient temperature was set to 30°C.

Since incident solar radiation is ~10x greater than emission in the infrared, a 1% gain in solar absorption can lead to a loss of ~10 W/m^2 in cooling power. For example, an emitter with 97% solar reflectance would be expected to have a drop in cooling performance of 30 W/m^2 compared to a perfect solar reflector (Fig. 1.6a). During winter months when the zenith angle is closer to the horizon, the incident radiation will be lower, however, additional cooling is typically not favorable in the winter. In the summer when cooling is desirable, the solar intensity reaches its peak, which presents challenges for passive radiative cooling modules. Solar heating would also negatively affect the achievable stagnation temperature, however, thermally decoupling the emitter from the solar rays by way of insulation can minimize heating.

The effective atmospheric heating from the ambient surroundings can be represented by the heat transfer coefficient (h_{eff}). This is the rate of heat transfer per unit area per unit temperature

difference, typically due to conduction and convection. Lowering the h_{eff} prevents parasitic heating of the emitter from the surrounding, enabling lower stagnation temperatures. This parameter is also what determines the slope of the cooling power curve, therefore, a lower h_{eff} would result in larger temperature reductions. For example, an emitter paired with an insulator with $h_{eff} = 5\frac{W}{m^2 K}$ would reach temperatures nearly 2x cooler than an insulator with $h_{eff} = 10\frac{W}{m^2 K}$ (Fig. 1.6b). When it comes to achieving optimal daytime cooling performance, it is important to thermally decouple the emitter from atmospheric and solar heating by having low h_{eff} while also maintaining high solar reflectance.

1.8 Thesis Outline

This dissertation begins in *Chapter 1* with the motivation for energy management in moving towards a sustainable future, specifically with thermal management. The concept and mechanism of passive radiative cooling were introduced to provide electricity-free thermal management by tailoring the optical and thermal properties of nanostructured materials.

Chapter 2 discusses modeling optical and thermal properties to design nanoporous materials for sub-ambient radiative cooling. Optical modeling using the Rayleigh method is introduced and paired with the radiative transfer equation (RTE) to predict the radiative cooling performance of various materials and designs. Solutions to the RTE are fed into the HTE and energy balances, which are then used to relate the thermal properties to radiative cooling. The HTE in tandem with the RTE model serves as a foundation to predict the cooling performance for insulating porous materials.

Chapter 3 details the use of controlled nanofiber morphology to selectively reflect solar radiation while retaining transparency in the infrared for use as a radiative cooling cover. Hierarchical morphological control is achieved by electrospinning varying concentrations of polyacrylonitrile. Experimental and optical modeling confirms broad solar reflectance because of the desired hierarchical beaded morphology and polydispersity. Outdoor measurements were also conducted to test the cooling performance of the radiative cooling covers.

Chapter 4 builds on chapter 3 to optimize the size and distribution of the nanofibers. The nanofibers are paired with a specular reflective mirrored emitter to enhance the solar reflectance to near 100%. Cooling power and stagnation temperature were both measured outdoors and compared to a current state-of-the-art reflective emitter.

Chapter 5 includes a summary of this thesis' work as well as recommendations for future work.

1.9 References

(1)   Hosseini, B.; Namazian, A. An Overview of Iranian Ice Repositories, An Example of Traditional Indigenous Architecture. *METU JFA* **2012**. https://doi.org/10.4305/METU.JFA.2012.2.10.

(2)   The Future of Cooling https://www.iea.org/reports/the-future-of-cooling.

(3)   Smith, G. B.; Granqvist, C. G. Coolness: High-Albedo Surfaces and Sky Cooling Devices. In *Green Nanotechnology: Solutions for Sustainability and Energy in the Built Environment*; CRC Press, 2011; pp 303–359.

(4)   Fernandez, N.; Wang, W.; Alvine, K. J.; Katipamula, S. *Energy Savings Potential of Radiative Cooling Technologies*; PNNL--24904; Pacific Northwest National Laboratory (PNNL), Richland, WA (US), 2015.

(5)   Rosenfeld, A. H.; Akbari, H.; Romm, J. J.; Pomerantz, M. Cool Communities: Strategies for Heat Island Mitigation and Smog Reduction. *Energy Build.* **1998**, *28* (1), 51–62. https://doi.org/10.1016/S0378-7788(97)00063-7.

(6)   Oleson, K. W.; Bonan, G. B.; Feddema, J. Effects of White Roofs on Urban Temperature in a Global Climate Model. *Geophys. Res. Lett.* **2010**, *37* (3). https://doi.org/10.1029/2009GL042194.

(7)   Munday, J. N. Tackling Climate Change through Radiative Cooling. *Joule* **2019**, 1–3. https://doi.org/10.1016/j.joule.2019.07.010.

(8)   Khedari, J.; Waewsak, J.; Thepa, S.; Hirunlabh, J. Field Investigation of Night Radiation Cooling under Tropical Climate. *Renew. Energy* **2000**, *20* (2), 183–193. https://doi.org/10.1016/S0960-1481(99)00104-4.

(9)   Watson, A.; Watson, D. Direct, Diffuse and Reflected Radiationitle https://www.ftexploring.com/solar-energy/direct-and-diffuse-radiation.htm#:~:text=When the sky is clear,10° above the horizon.

(10)   Kim, H.; McSherry, S.; Brown, B.; Lenert, A. Selectively Enhancing Solar Scattering for Direct Radiative Cooling through Control of Polymer Nanofiber Morphology. *ACS Appl. Mater. Interfaces* **2020**, *12* (39), 43553–43559. https://doi.org/10.1021/acsami.0c09374.

(11)   Hossain, M. M.; Gu, M. Radiative Cooling: Principles, Progress, and Potentials. *Adv. Sci.* **2016**, *3* (7), 1–10. https://doi.org/10.1002/advs.201500360.

(12)   Catalanotti, S.; Cuomo, V.; Piro, G.; Ruggi, D.; Silvestrini, V.; Troise, G. The Radiative Cooling of Selective Surfaces. *Sol. Energy* **1975**, *17* (2), 83–89. https://doi.org/10.1016/0038-092X(75)90062-6.

(13)   *Solar Heat Technologies: Fundamentals and Applications (Passive Cooling)*; Cook, J., Ed.; The MIT Press: Cambridge, 1989.

(14)   Chen, Z.; Zhu, L.; Raman, A.; Fan, S. Radiative Cooling to Deep Sub-Freezing Temperatures through a 24-h Day-Night Cycle. *Nat. Commun.* **2016**, *7*, 1–5. https://doi.org/10.1038/ncomms13729.

(15)   Bhatia, B.; Leroy, A.; Shen, Y.; Zhao, L.; Gianello, M.; Li, D.; Gu, T.; Hu, J.; Soljačić, M.; Wang, E. N. Passive Directional Sub-Ambient Daytime Radiative Cooling. *Nat. Commun.* **2018**, *9* (1), 5001. https://doi.org/10.1038/s41467-018-07293-9.

(16)   Zhou, L.; Song, H.; Liang, J.; Singer, M.; Zhou, M.; Stegenburgs, E.; Zhang, N.; Xu, C.; Ng, T.; Yu, Z.; Ooi, B.; Gan, Q. A Polydimethylsiloxane-Coated Metal Structure for All-Day Radiative Cooling. *Nat. Sustain.* **2019**, *2* (August). https://doi.org/10.1038/s41893-019-0348-5.

(17)   Torgerson, E.; Hellhake, J. Polymer Solar Filter for Enabling Direct Daytime Radiative Cooling. *Sol. Energy Mater. Sol. Cells* **2020**, *206*, 110319. https://doi.org/10.1016/j.solmat.2019.110319.

(18)   Raman, A. P.; Anoma, M. A.; Zhu, L.; Rephaeli, E.; Fan, S. Passive Radiative Cooling below Ambient Air Temperature under Direct Sunlight. *Nature* **2014**, *515* (7528), 540–544. https://doi.org/10.1038/nature13883.

(19)   Family, R.; Mengüç, M. P. Materials for Radiative Cooling: A Review. *Procedia Environ. Sci.* **2017**, *38*, 752–759. https://doi.org/10.1016/j.proenv.2017.03.158.

(20)   Vall, S.; Castell, A. Radiative Cooling as Low-Grade Energy Source: A Literature Review. *Renew. Sustain. Energy Rev.* **2017**, *77*, 803–820. https://doi.org/10.1016/j.rser.2017.04.010.

(21)   Zeyghami, M.; Goswami, D. Y.; Stefanakos, E. A Review of Clear Sky Radiative Cooling Developments and Applications in Renewable Power Systems and Passive Building Cooling. *Sol. Energy Mater. Sol. Cells* **2018**, *178*, 115–128. https://doi.org/10.1016/j.solmat.2018.01.015.

(22)   Zhao, B.; Hu, M.; Ao, X.; Chen, N.; Pei, G. Radiative Cooling : A Review of Fundamentals , Materials , Applications , and Prospects. *Appl. Energy* **2019**, *236*, 489–513. https://doi.org/10.1016/j.apenergy.2018.12.018.

(23)   Zhao, D.; Aili, A.; Zhai, Y.; Xu, S.; Tan, G.; Yin, X.; Yang, R. Radiative Sky Cooling: Fundamental Principles, Materials, and Applications. *Appl. Phys. Rev.* **2019**, *6* (2), 021306. https://doi.org/10.1063/1.5087281.

(24)   Chen, J.; Lu, L. Development of Radiative Cooling and Its Integration with Buildings: A Comprehensive Review. *Sol. Energy* **2020**, *212* (November), 125–151. https://doi.org/10.1016/j.solener.2020.10.013.

(25)   Jeong, S. Y.; Tso, C. Y.; Wong, Y. M.; Chao, C. Y. H.; Huang, B. Daytime Passive Radiative Cooling by Ultra Emissive Bio-Inspired Polymeric Surface. *Sol. Energy Mater. Sol. Cells* **2019**, *206*, 110296. https://doi.org/10.1016/j.solmat.2019.110296.

(26)   Kou, J. long; Jurado, Z.; Chen, Z.; Fan, S.; Minnich, A. J. Daytime Radiative Cooling Using Near-Black Infrared Emitters. *ACS Photonics* **2017**, *4* (3), 626–630. https://doi.org/10.1021/acsphotonics.6b00991.

(27)   Yang, J.; Gao, X.; Wu, Y.; Zhang, T.; Zeng, H.; Li, X. Nanoporous Silica Microspheres–Ploymethylpentene (TPX) Hybrid Films toward Effective Daytime Radiative Cooling. *Sol. Energy Mater. Sol. Cells* **2019**, No. 1295, 110301. https://doi.org/10.1016/j.solmat.2019.110301.

(28)   Zhai, Y.; Ma, Y.; David, S. N.; Zhao, D.; Lou, R.; Tan, G.; Yang, R.; Yin, X. Scalable-Manufactured Randomized Glass-Polymer Hybrid Metamaterial for Daytime Radiative Cooling. *Science (80-.).* **2017**, *355* (6329), 1062–1066. https://doi.org/10.1126/science.aai7899.

(29)   Mandal, J.; Jia, M.; Overvig, A.; Fu, Y.; Yu, N.; Yang, Y.; Mandal, J.; Jia, M.; Overvig, A.; Fu, Y.; Che, E.; Yu, N. Porous Polymers with Switchable Optical Transmittance for Optical and Thermal Regulation. *Joule* **2019**, 1–12. https://doi.org/10.1016/j.joule.2019.09.016.

(30)   Mandal, J.; Fu, Y.; Overvig, A.; Jia, M.; Sun, K.; Shi, N.; Zhou, H.; Xiao, X.; Yu, N.; Yang, Y. Hierarchically Porous Polymer Coatings for Highly Efficient Passive Daytime Radiative Cooling. *Science (80-.).* **2018**, *362* (6412), 315–319. https://doi.org/10.1126/science.aat9513.

(31)   Goldstein, E. A.; Raman, A. P.; Fan, S. Sub-Ambient Non-Evaporative Fluid Cooling with the Sky. *Nat. Energy* **2017**, *2* (9), nenergy2017143. https://doi.org/10.1038/nenergy.2017.143.

(32)   Gentle, A. R.; Smith, G. B. A Subambient Open Roof Surface under the Mid-Summer Sun. *Adv. Sci.* **2015**, *2* (9). https://doi.org/10.1002/advs.201500119.

(33)   Li, T.; Zhai, Y.; He, S.; Gan, W.; Wei, Z.; Heidarinejad, M.; Dalgo, D.; Mi, R.; Zhao, X.; Song, J.; Dai, J.; Chen, C.; Aili, A.; Vellore, A.; Martini, A.; Yang, R.; Srebric, J.; Yin, X.; Hu, L. A Radiative Cooling Structural Material. *Science (80-.).* **2019**, *364* (6442), 760–763. https://doi.org/10.1126/science.aau9101.

(34)   He, S.; Chen, C.; Li, T.; Song, J.; Zhao, X.; Kuang, Y.; Liu, Y.; Pei, Y.; Hitz, E.; Kong, W.; Gan, W.; Yang, B.; Yang, R.; Hu, L. An Energy-Efficient, Wood-Derived Structural Material Enabled by Pore Structure Engineering towards Building Efficiency. *Small Methods* **2019**, *4* (1). https://doi.org/10.1002/smtd.201900747.

(35)   Fu, Y.; Yang, J.; Su, Y. S.; Du, W.; Ma, Y. G. Daytime Passive Radiative Cooler Using Porous Alumina. *Sol. Energy Mater. Sol. Cells* **2019**, *191*, 50–54. https://doi.org/10.1016/j.solmat.2018.10.027.

(36)   Alden, J. D.; Atiganyanun, S.; Vanderburg, R.; Lee, S. H.; Plumley, J. B.; Abudayyeh, O. K.; Han, S. M.; Han, S. E. Radiative Cooling by Silicone-Based Coating with Randomly Distributed Microbubble Inclusions. *J. Photonics Energy* **2019**, *9* (03), 1. https://doi.org/10.1117/1.jpe.9.032705.

(37)   Atiganyanun, S.; Plumley, J.; Han, S. J.; Hsu, K.; Cytrynbaum, J.; Peng, T. L.; Han, S. M.; Han, S. E. Effective Radiative Cooling by Paint-Format Microsphere-Based Photonic Random Media. *ACS Photonics* **2018**, *5* (4), 1181–1187. https://doi.org/10.1021/acsphotonics.7b01492.

(38) Bao, H.; Yan, C.; Wang, B.; Fang, X.; Zhao, C. Y.; Ruan, X. Double-Layer Nanoparticle-Based Coatings for Efficient Terrestrial Radiative Cooling. *Sol. Energy Mater. Sol. Cells* **2017**, *168* (November 2016), 78–84. https://doi.org/10.1016/j.solmat.2017.04.020.

(39) Xiao, R.; Hou, C.; Yang, W.; Su, Y.; Li, Y.; Zhang, Q.; Gao, P.; Wang, H. Infrared-Radiation-Enhanced Nanofiber Membrane for Sky Radiative Cooling of the Human Body. *ACS Appl. Mater. Interfaces* **2019**, *11* (47), 44673–44681. https://doi.org/10.1021/acsami.9b13933.

(40) Wang, X.; Liu, X.; Li, Z.; Zhang, H.; Yang, Z.; Zhou, H.; Fan, T. Scalable Flexible Hybrid Membranes with Photonic Structures for Daytime Radiative Cooling. *Adv. Funct. Mater.* **2020**, *30* (5), 1–9. https://doi.org/10.1002/adfm.201907562.

(41) Huang, X.; Li, N.; Wang, J.; Liu, D.; Xu, J.; Zhang, Z.; Zhong, M. Single Nanoporous MgHPO4·1.2H2O for Daytime Radiative Cooling. *ACS Appl. Mater. Interfaces* **2020**, *12* (2), 2252–2258. https://doi.org/10.1021/acsami.9b14615.

(42) Rephaeli, E.; Raman, A.; Fan, S. Ultrabroadband Photonic Structures to Achieve High-Performance Daytime Radiative Cooling. *Nano Lett.* **2013**, *13* (4), 1457–1461. https://doi.org/10.1021/nl4004283.

(43) Hossain, M. M.; Jia, B.; Gu, M. A Metamaterial Emitter for Highly Efficient Radiative Cooling. *Adv. Opt. Mater.* **2015**, *3* (8), 1047–1051. https://doi.org/10.1002/adom.201500119.

(44) Li, Y.; Xue, X.; Yang, Z.; He, Z.; Qin, J.; Qu, J.; Zhang, W.; Xu, L. Generic Method for Creating Waterborne Coatings with Sub-Ambient Daytime Cooling–Part I: Optical Properties and Rooftop Cooling Effect Measurements. *Sol. Energy Mater. Sol. Cells* **2020**, *204* (October 2019), 110205. https://doi.org/10.1016/j.solmat.2019.110205.

(45) Harrison, A. W.; Walton, M. R. Radiative Cooling of TiO2 White Paint. *Sol. Energy* **1978**, *20* (2), 185–188. https://doi.org/10.1016/0038-092X(78)90195-0.

(46) Li, X.; Peoples, J.; Huang, Z.; Zhao, Z.; Qiu, J.; Ruan, X. Full Daytime Sub-Ambient Radiative Cooling in Commercial-like Paints with High Figure of Merit. *Cell Reports Phys. Sci.* **2020**, *1* (10), 100221. https://doi.org/10.2139/ssrn.3652325.

(47) Kim, H.; Lenert, A. Optical and Thermal Filtering Nanoporous Materials for Sub-Ambient Radiative Cooling. *J. Opt.* **2018**, *20* (084002). https://doi.org/https://doi.org/10.1088/2040-8986/aacaa1.

(48) Leroy, A.; Bhatia, B.; Kelsall, C. C.; Castillejo-Cuberos, A.; Di Capua, M. H.; Zhao, L.; Zhang, L.; Guzman, A. M.; Wang, E. N. High-Performance Subambient Radiative Cooling Enabled by Optically Selective and Thermally Insulating Polyethylene Aerogel. *Sci. Adv.* **2019**, *5* (eaat9480). https://doi.org/10.1126/sciadv.aat9480.

(49) Nilsson, T. M. J.; Niklasson, G. A.; Granqvist, C. G. A Solar Reflecting Material for Radiative Cooling Applications: ZnS Pigmented Polyethylene. *Sol. Energy Mater. Sol. Cells* **1992**, *28* (2), 175–193. https://doi.org/10.1016/0927-0248(92)90010-M.

(50) Cai, L.; Song, A. Y.; Li, W.; Hsu, P.-C.; Lin, D.; Catrysse, P. B.; Liu, Y.; Peng, Y.; Chen, J.; Wang, H.; Xu, J.; Yang, A.; Fan, S.; Cui, Y. Spectrally Selective Nanocomposite Textile for Outdoor Personal Cooling. *Adv. Mater.* **2018**, *30* (35). https://doi.org/10.1002/adma.201802152.

(51) Peng, Y.; Chen, J.; Song, A. Y.; Catrysse, P. B.; Hsu, P.-C.; Cai, L.; Liu, B.; Zhu, Y.; Zhou, G.; Wu, D. S.; Lee, H. R.; Fan, S.; Cui, Y. Nanoporous Polyethylene Microfibres for Large-Scale Radiative Cooling Fabric. *Nat. Sustain.* **2018**, *1* (2), 105–112. https://doi.org/10.1038/s41893-018-0023-2.

(52) Gentle, A. R.; Dybdal, K. L.; Smith, G. B. Polymeric Mesh for Durable Infra-Red Transparent Convection Shields: Applications in Cool Roofs and Sky Cooling. *Sol. Energy Mater. Sol. Cells* **2013**, *115*, 79–85. https://doi.org/10.1016/j.solmat.2013.03.001.

(53) Liu, C.; Cai, L.; Song, A. Y.; Wu, P.; Peng, Y.; Zhou, C.; Fan, S.; Yang, A.; Chen, J.; Catrysse, P. B.; Hsu, P.-C.; Zhou, C.; Cui, Y.; Liu, Y. Warming up Human Body by Nanoporous Metallized Polyethylene Textile. *Nat. Commun.* **2017**, *8* (1). https://doi.org/10.1038/s41467-017-00614-4.

(54) Yang, M.; Zou, W.; Guo, J.; Qian, Z.; Luo, H.; Yang, S.; Zhao, N. Bioinspired " Skin " with Cooperative Thermo-Optical Effect for Daytime Radiative Cooling. *ACS Appl. Mater. Interfaces* **2020**. https://doi.org/10.1021/acsami.0c03897.

Chapter 2: Optical and Thermal Filtering Nanoporous Materials for Sub-Ambient Radiative Cooling

2.1 Motivation

Previous efforts to demonstrate sub-ambient passive radiative cooling have broadly focused on selective surfaces and convection covers. The stringent requirement of high solar reflectance, however, limits the daytime cooling power of selective surfaces. To thermally insulate the emitter from the surroundings, infrared transparent convection covers such as polyethylene films,[1–4] structured polyethylene,[5,6] polyethylene with embedded particles for enhanced scattering,[7–9] and semi- conductor windows[10–14] have been considered. For example, Chen et al. utilized a thick ZnSe window to enclose a vacuum-insulated solar-shaded design, which achieved 40°C below ambient.[10] Since the selective emitter was comparable to their previous work,[1] the improved performance may be attributed to a combination of vacuum insulation and a sunshade that eliminated direct solar radiation, effectively mimicking nighttime conditions. Although this design illustrates the potential of radiative cooling in near idealized conditions, a rooftop vacuum chamber and a thick crystalline infrared (IR) cover preclude its use for large area applications. Previous work on scalable convection covers has focused on either enhancing the properties of polymeric films or fabricating robust covers with voids larger than the long wavelength edge (13 μm) of the atmospheric window. For example, scattering particle films of ZnSe,[8] ZnS,[11,12] and CdS[13] were used to achieve high solar reflectance while retaining high transmittance in the IR. Meshes and corrugated structures have also been fabricated using high-density polyethylene foils to provide a

20

robust convection cover.[5,6] Nevertheless, robust, scalable and selective covers with high transmittance in the atmospheric window have yet to be demonstrated.

In this section, we investigate the use of IR-transparent nanoporous materials as insulating convective covers for high-performance daytime and nighttime radiative cooling (Fig. 2.1). The ideal nanoporous cover transmits radiation in the 8–13 μm band while blocking radiation below 8 μm (mostly solar) and above 13 μm (mostly atmospheric). Unlike selective emitter designs, heat transfer with Space originates from selective transmission through a thermally insulating nanoporous cover. The approach is fundamentally different because spatial regions shielding the emitter from solar and atmospheric heat are thermally decoupled from spatial regions that emit to Space. Such a cover would also allow the use of a broadband emitter or decrease the stringent requirements imposed on a selective emitter. Unlike previous works on convection covers, the pores are much smaller than the short-wavelength edge (8 μm) of the atmospheric window. Further, we explore the use of materials that are absorptive at long wavelengths (>13 μm) to provide additional shielding from atmospheric heating.
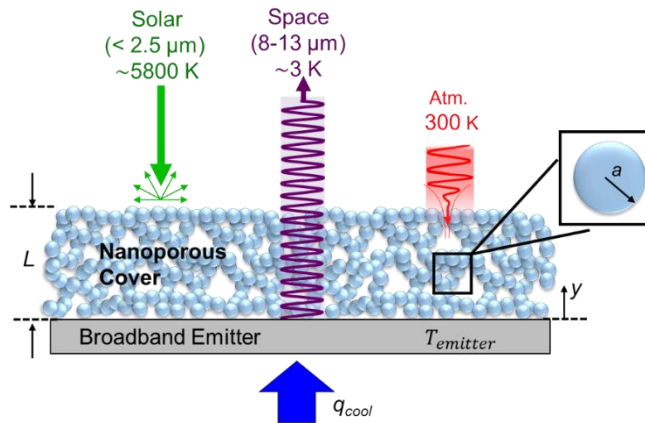
Figure 2.1. Selectively transparent nanoporous cover: schematic of our modeled radiative cooling system consisting of a thermally insulating nanoporous cover and a broadband emitter that radiates heat to Space. Critical dimensions of the cover are shown, including cover thickness (*L*) and scatterer radius (*a*).

The effects of scattering radius cover thickness and cover material on the optical and thermal characteristics of the cover and its radiative cooling performance at sub-ambient temperatures are presented. The temperature profiles and cooling performance are determined by modeling coupled radiative and conductive heat transport in the cover. In addition, the effects of structural parameters (particle radius and cover thickness) on the cooling performance are investigated. Finally, the material effects on the cooling performance are discussed by comparing three case studies: BaF_2, ZnS, and polyethylene (PE).

2.2 Radiative Cooling Energy Balance

Net cooling is achieved when more heat is rejected than absorbed by the emitter. This can be broken down into a simple energy balance represented below:

$$q_{net} = q_e - q_{sol} - q_{amb-rad} - q_{amb-nrad} \qquad \text{(Eq. 2.1)}$$

Here, q_e is the emitted radiation from the emitter, q_{sol} is the absorbed AM1.5G solar radiation by the emitter, and $q_{amb-rad}$ and $q_{amb-nrad}$ represents the radiative and non-radiative heat transfer with the ambient, respectively.

The emitted power is a function of both temperature and wavelength as given by:

$$q_e = 2\pi \int_0^\infty \int_0^{\pi/2} \varepsilon_{eff}(\lambda) I_b(T_e, \lambda) cos\theta sin\theta \; d\theta \; d\lambda \qquad \text{(Eq. 2.2)}$$

λ, θ, T_e, and ε_{eff} are the wavelength, polar angle, emitter temperature, and effective emissivity of the emitter and cover assembly. I_b is the blackbody intensity given by Planck's law:

$$I_b(T, \lambda) = \frac{2hc^2}{\lambda^5 (e^{hc/\lambda k_B T} - 1)} \qquad \text{(Eq. 2.3)}$$

where h, c, and k_B, is Planck's constant, speed of light, and Boltzmann's constant, respectively.

The solar contribution considers the reflective properties of both the emitter and cover, as given by:

$$q_{sol} = \int_0^\infty \varepsilon_{eff}(\lambda) H_{AM1.5}(\lambda) \cos\theta_s \, d\lambda$$

(Eq. 2.4)

where $H_{AM1.5}(\lambda)$ is the AM1.5G[15] spectral irradiance (which integrates to 1000 W/m^2) and θ_s is the angle between the incident solar rays and the surface normal of the emitter.

The radiative atmospheric heating term, $q_{amb-rad}$, is given by:

$$q_{amb-rad} = 2\pi \int_0^\infty \int_0^{\pi/2} \varepsilon_{amb}(\lambda,\theta) \varepsilon_{eff}(\lambda) I_b(T_{amb},\lambda) \cos\theta \sin\theta \, d\theta \, d\lambda$$

(Eq. 2.5)

The emissivity of the ambient (ε_{amb}) is determined assuming Kirchoff's law where the angle-dependent emissivity is $\varepsilon_{amb}(\lambda) = 1 - \tau_{atm}(\lambda)^{1/\cos\theta}$ and τ_{atm} is the zenith direction atmospheric transmittance.[16]

The non-radiative heating term, $q_{amb-nrad}$, is given by:

$$q_{amb-nrad} = h_{eff}(T_{amb} - T_e)$$

(Eq. 2.6)

where h_{eff} is the effective conductive and convective heat transfer coefficient between the emitting surface and the surroundings.

2.3 Heat Transfer (HTE)

Our thermal transport model considers both conductive and wavelength-dependent radiative heat transfer. A steady-state one-dimensional HTE (Eq. 2.7) was numerically solved to obtain the temperature profile of the cover,

23

$$0 = k_{eff} \frac{d^2T}{dy^2} - \nabla q_r \qquad \text{(Eq. 2.7)}$$

where k_{eff} is the effective thermal conductivity, T is the temperature of the cover as a function of position y, and q_r is the radiative heat flux. For the bottom boundary condition ($y = 0$), we set the temperature of the emitter: $T(y = 0) = T_{emitter}$. For the top boundary condition ($y = L$), we equated the heat flux to the convective heat transfer between the top of the cover and the surroundings: $q(y = L) = U(T(y = L) - T_{amb})$, where U=10 W/m²/K and T_{amb}= 300 K. The effective thermal conductivity (k_{eff}) was set to 0.02 W/m/K to be consistent with nanostructured materials with high porosity, such as silica aerogels.[17,26,27] Such materials have structural features that are smaller than the mean free path of the thermal energy carriers (*i.e.*, molecules and phonons), resulting in low thermal conductivity.[17] Since our focus is on radiative transport, a detailed simulation of thermal conductivity is beyond the scope of this study.

The radiative heat flux, q_r, was calculated using the radiative transfer equation (RTE) which describes scattering, emission, and absorption within the cover.[25] The cooling power (q_{cool}) was determined from steady-state temperature profiles by calculating the heat flux leaving the emitter due to conductive and radiative contributions. The divergence of the radiative heat flux was calculated and substituted into the HTE (Eq. 2.7) to determine a new temperature profile. This procedure was repeated until the resulting temperature profile converged to within 10^{-6} of the input temperature profile to the RTE. Both the RTE and the heat equation were solved numerically. A flow diagram illustrating the overall algorithm is provided in Fig. 2.2.
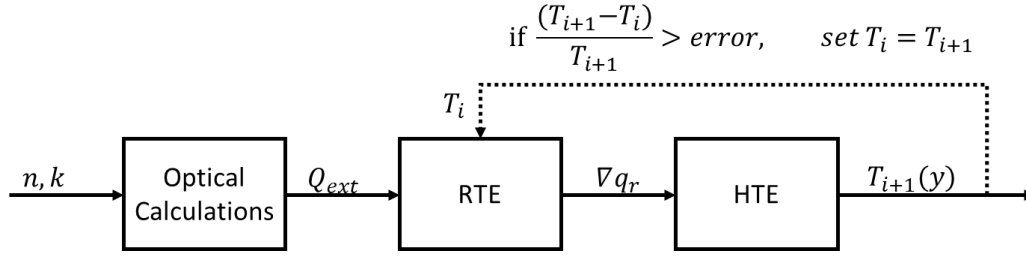
Figure 2.2 Flow chart of optical and thermal modeling used to calculate the temperature profile of a porous cover and cooling power.

2.4 Modeling Optical Properties of Scattering Particles

To determine the radiative properties of the nanoporous cover, we describe it as a collection of independently scattering nanoparticles. This method has been used to describe materials with a similar microstructure, such as silica aerogels, and agrees well with experimental results for transmittance.[17–20] We focus on materials with a low volume fraction of solids because we are interested in high porosity covers with low thermal conductivity. The nanoparticles range in radius (*a*) from 50 to 300 nm.

Most of the thermal radiation (>98%) from the emitter, cover, Space, and atmosphere occurs at long wavelengths ($\lambda > 3$ μm) relative to the size of the nanoparticles. Since the size parameter is small for this spectral region ($x = \frac{2\pi a}{\lambda} \ll 1$), we model the particles as Rayleigh scatterers.[21,22] We assume that all solar radiation is scattered near the top of the cover since the particles are comparable in size to the wavelength and the thickness of the cover is much greater than the penetration depth of wavelengths associated with solar radiation.[21] This effectively mimics nighttime conditions and allows us to explore the limits of radiative cooling.

The optical model describes the absorption and scattering of electromagnetic radiation by small particles. In the Rayleigh scattering regime, the scattering efficiency (Q_{sca}), absorption efficiency (Q_{abs}), and extinction efficiency (Q_{ext}) can be determined using Eq. 2.8 – 2.10,[21]

$$Q_{sca} = \frac{8}{3}x^4 \left| \frac{m^2 - 1}{m^2 + 2} \right|^2 \tag{Eq. 2.8}$$

$$Q_{abs} = 4xIm\left\{ \frac{m^2 - 1}{m^2 + 2} \right\} \tag{Eq. 2.9}$$

$$Q_{ext} = Q_{sca} + Q_{abs} \tag{Eq. 2.10}$$

$m = \frac{N_{particle}}{N_{medium}}$ represents the effective refractive index of the particle in the medium, where $N_{particle}$ and N_{medium} are the complex refractive indices of the particle and medium, respectively. The extinction coefficient (β) increases linearly with the volume fraction (f_v) according to Eq. 2.11.

$$\beta = f_v \frac{3}{4a} Q_{ext} \tag{Eq. 2.11}$$

Material optical properties were obtained from the literature and the real and imaginary parts of the refractive index are plotted in Fig. 2.3.[23] The outputs of the optical calculation are the scattering and absorption efficiencies, which are used as inputs in the radiative transfer equation (RTE).
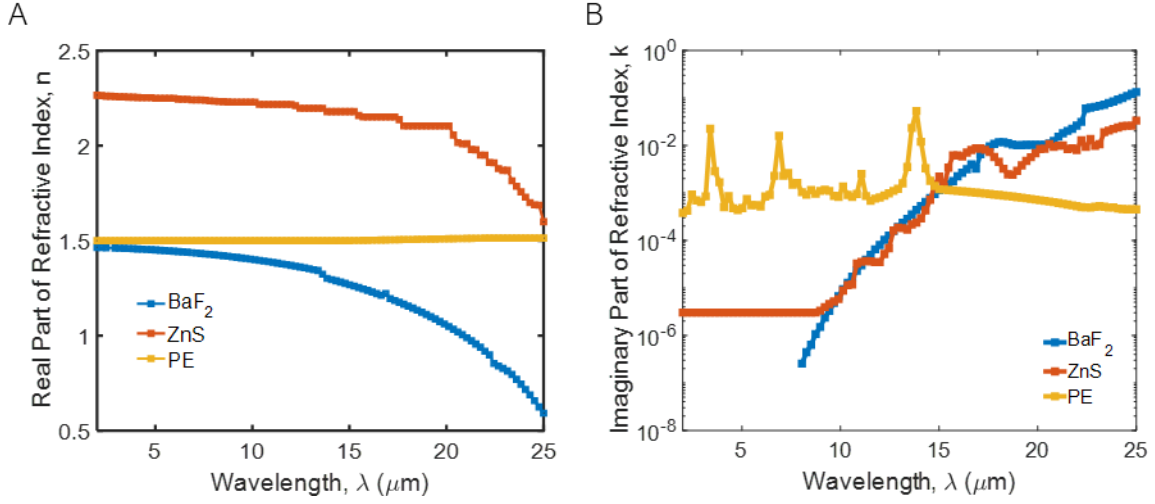
Figure 2.3. (A) Real part and (B) imaginary part of the refractive index for BaF₂, ZnS, and PE.[24]

2.5 Radiative Transfer (RTE)

The radiative transfer equation (RTE) and the heat transfer equation (HTE) are solved iteratively to determine the steady-state temperature profile and the radiative heat flux within the cover. Both the RTE and the HTE were solved numerically.

Our RTE model assumes a one-dimensional plane-parallel medium with diffuse boundary surfaces and isotropic sources (Eq. 2.12). The solution procedure closely follows the description by Modest for the relevant simplifications and a specified temperature profile.[25]

$$q_r(\tau) = 2J_1 E_3(\tau) - 2J_2 E_3(\tau_L - \tau) + 2\pi \int_0^\tau S(\tau') E_2(\tau - \tau') d\tau'$$

$$- 2\pi \int_\tau^{\tau_L} S(\tau') E_2(\tau' - \tau) d\tau'$$

(Eq. 2.12)

$E_\eta(x)$ is an integral of order η (Eq. 2.13), J is the radiosity of the surface (Eq. 2.14), τ is the optical thickness ($\tau = \int_0^y \beta dy$), and $S(\tau')$ is an internal source of radiation due to emission and scattering at a location specified by τ' (Eq. 2.15).

$$E_\eta(x) = \int_0^1 \mu^{\eta-2} e^{-x/\mu} d\mu \qquad \text{(Eq. 2.13)}$$

$$J = \pi I_b \qquad \text{(Eq. 2.14)}$$

$$S(\tau') = (1 - \omega)I_b(\tau) + \frac{\omega}{4\pi} G(\tau) \qquad \text{(Eq. 2.15)}$$

The direction of a ray relative to the normal is specified by $\mu = \cos(\theta)$. ω is the albedo. $I_b(\tau)$ is the intensity of thermal emission given by Planck's law (Eq. 2.16). $G(\tau)$ is the irradiation at a given location (Eq. 2.17).

$$I_b(\tau) = \frac{2hc^2}{n^2\lambda^5(e^{hc/\lambda k_B T} - 1)} \qquad \text{(Eq. 2.16)}$$

$$G(\tau) = 2J_1 E_2(\tau) + 2J_2 E_2(\tau_L - \tau) \qquad \text{(Eq. 2.17)}$$

$$+ 2\pi \int_0^\tau S(\tau')E_1(\tau - \tau')d\tau' + 2\pi \int_\tau^{\tau_L} S(\tau')E_1(\tau' - \tau)d\tau'$$

Three wavelength bands were used to account for the spectral dependence (see Fig. 2.4): Band I ($\lambda < 8\ \mu m$), Band II ($8\ \mu m < \lambda < 13\ \mu m$), and Band III ($\lambda > 13\ \mu m$). Planck's law was integrated to determine the fraction of black body intensity within each band depending on the temperature. Spectral properties were also averaged to solve the RTE within each band.
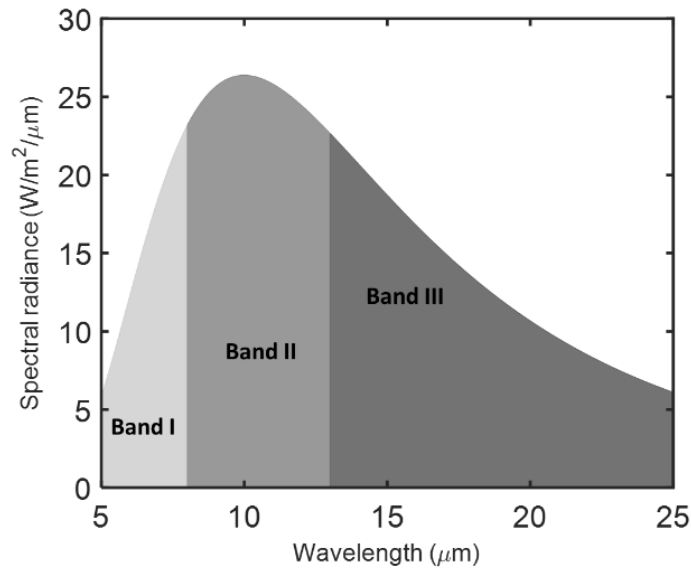
Figure 2.4. The RTE wavelength dependence is divided into three bands: Band I ($\lambda < 8\ \mu m$), Band II ($8\ \mu m < \lambda < 13\ \mu m$), and Band III ($\lambda > 13\ \mu m$).

Here, we set $\omega = 0$ because Band I accounts for a small fraction of radiative power relative to the total (~15%) at temperatures relevant for radiative cooling (~295 K). Rigorously solving for scattering in Band I would significantly increase the computational time and complexity. The attenuation in Band I is dominated by the size of the particle. As seen in Fig. 2.5, decreasing the particle radius below 150 nm has a negligible effect on the net cooling power. However, the effect on the optical thickness within Band I is significant. This indicates that a more rigorous treatment of scattering would have a negligible effect on the cooling power. We chose not to consider particle radii below 0.05 µm (50 nm) to ensure low transmittance in the solar region (below 2.5 µm) since our RTE model does not take into account solar contributions.
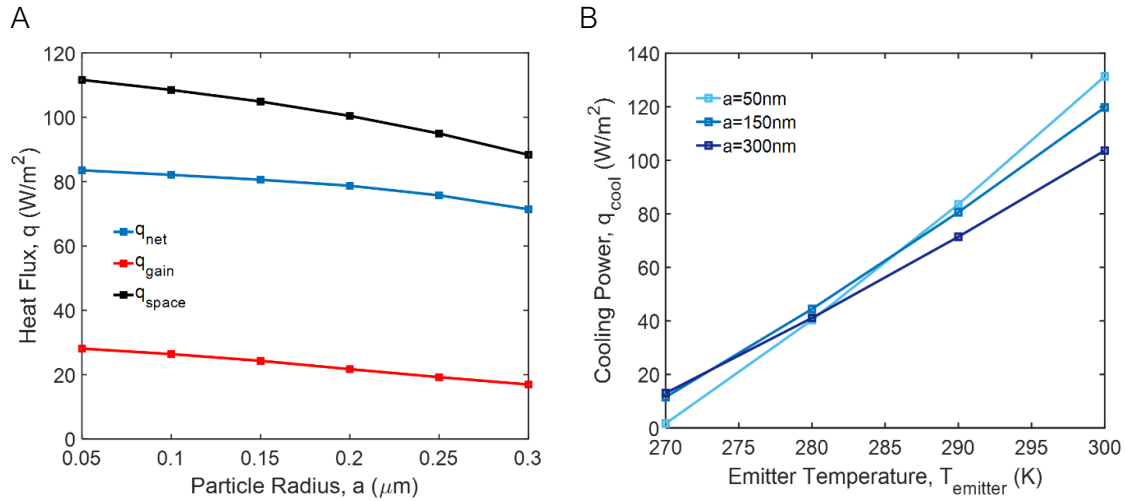
Figure 2.5. The effect of particle size on (A) the breakdown of heat fluxes and (B) the net cooling power for a 3 cm thick BaF_2 cover (0.01 volume fraction, $T_{emitter}$ = 290 K (ΔT = 10 K)). A small effect on heat flux is observed for particles sizes below 150 nm.

As inputs, the RTE requires the optical thickness of the cover at each wavelength, determined from the optical calculation, and the temperature profile within the cover. An initial guess was made for the temperature profile within the cover to solve the RTE. The radiative source term was divided into three bands according to the fraction of emissive power in each band for a black body at a given temperature. The emitter was modeled as a black, diffuse surface to determine the upward propagating radiosity. Thermal emission from the atmosphere and Space at 300 K and 3 K, respectively, were mixed according to a standard atmospheric transmittance to determine the downward propagating radiosity.[16]

2.6 Effects of Morphology and Cover Thickness

We used the model described above to investigate the effects of the particle radius (a) and cover thickness (L) on the transmittance and radiative cooling performance. The transmittance of the cover depends on the direction of the incident radiation and scattering albedo.[20,25] We show an approximate transmittance as $exp\,(-\beta L)$ in Fig. 2.6a,b, based on the Beer–Lambert law at normal incidence. As a baseline, we chose a 3 cm thick cover with a fixed volume fraction ($f_v = 0.01$) of 150 nm BaF$_2$ particles. We then varied the particle size and cover thickness.

An increase in particle size or an increase in cover thickness leads to decreased transmittance. Fig. 2.6c shows the optical thickness in terms of its scattering and absorptive contributions. As the particle size increases, the transmittance decreases at short wavelengths due to increased scattering (Fig. 2.6a). In contrast, increasing the cover thickness leads to attenuation across all wavelengths (Fig. 2.6b,d)); as a consequence, the transmittance decreases in both the desirable (8-13 µm) and undesirable bands.
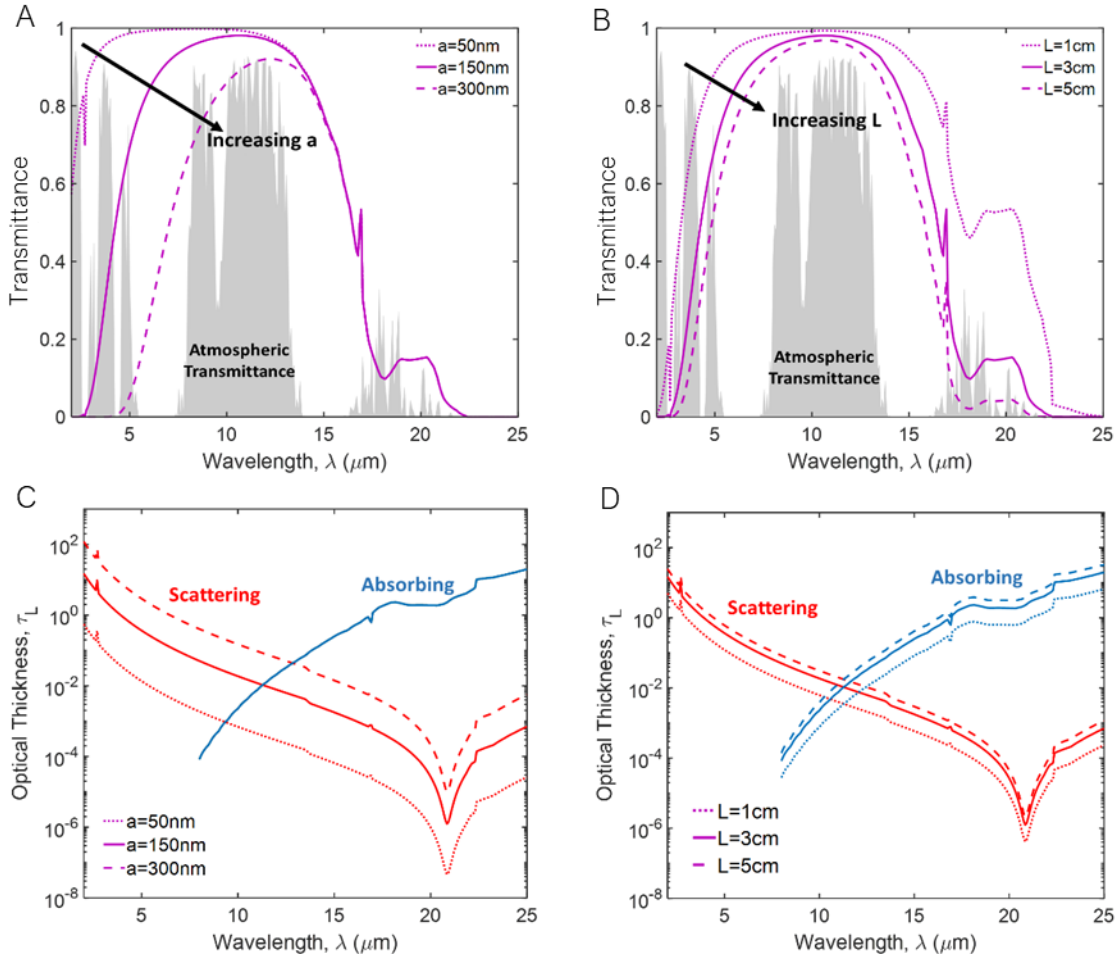
Figure 2.6. Radiative properties of a nanoporous cover: the effects of (A), (C) particle radius and (B), (D) cover thickness on the transmittance (approximated as $(exp\,(-\beta L))$) and the optical thickness due to (scattering and absorption) as a function of wavelength. The cover contains 1% BaF$_2$ (by volume). Atmospheric transmittance is shown in gray.[16]

To gain insight into the transport mechanisms within the cover and how they relate to the cooling power, we analyzed the steady-state temperature profiles (Fig. 2.7a) and the corresponding cooling power as a function of emitter temperature (Fig. 2.7b). At the top of the cover, convection is the dominant form of heat transfer, maintaining the surface temperature near the ambient temperature (300 K). A slight reduction from ambient temperature near the top is observed when the emitter is below ambient. Within the cover, conduction appears to be the dominant form of heat transfer

since the temperature profiles are approximately linear (Fig. 2.7a). However, there is some curvature in the profile near the top and bottom of the cover, indicating that radiative transfer in a participating medium is also an important transport mechanism.
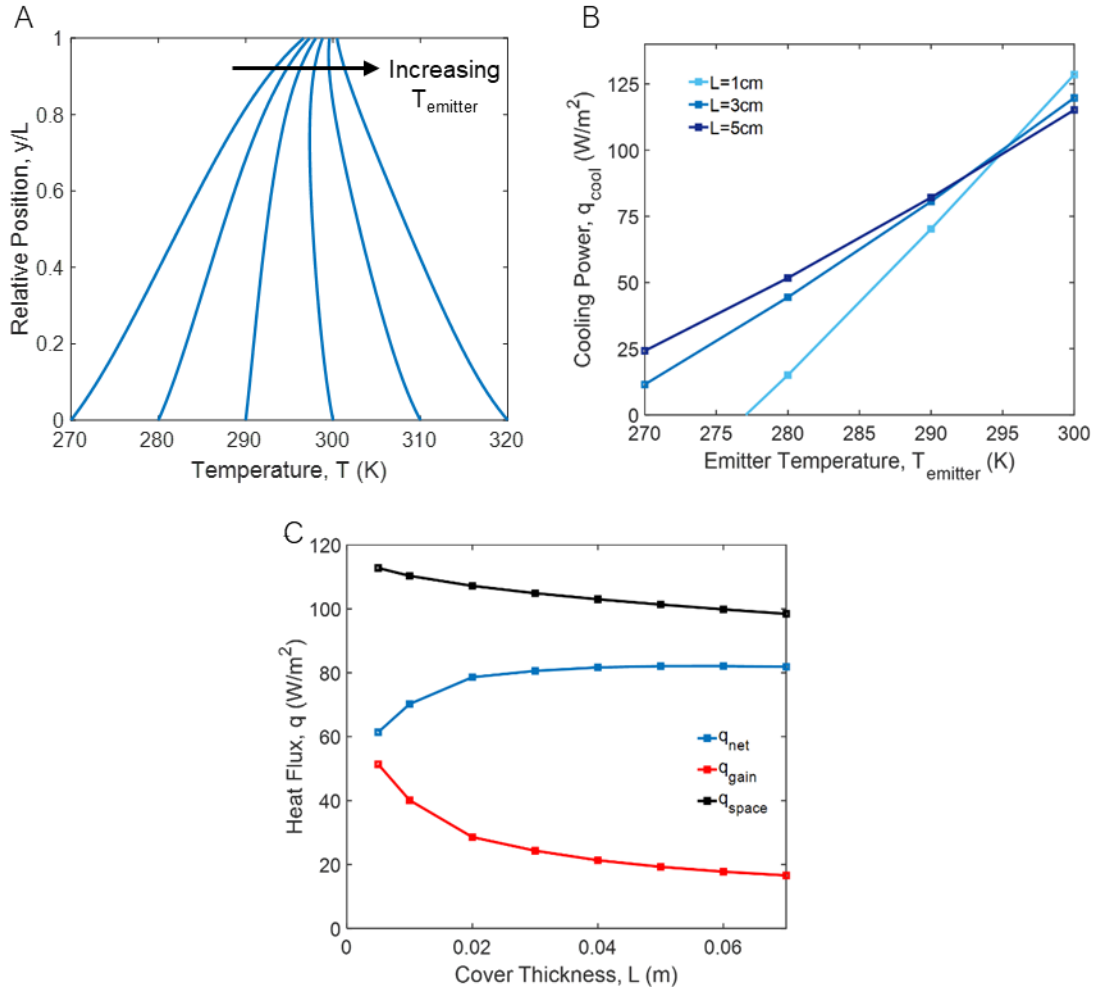
Figure 2.7. Temperature profiles and the effect of cover thickness. Temperature profiles (A) and cooling power (B) for a BaF$_2$ cover (150 nm radius particles, 1% by volume) as a function of emitter temperature ($T_{emitter}$). (C) Net cooling power (q_{net}), heat rejected to Space (q_{space}), and ambient heating (q_{gain}) as a function of cover thickness for $T_{emitter}$ = 290 K.

Cooling power increases approximately linearly with increasing emitter temperature (Fig. 2.7b). For a 3 cm thick BaF$_2$ cover, the maximum cooling power is ~120 W/m^2 (*i.e.*, the cooling power when $T_{emitter} = T_{amb} = 300$ K). When the emitter temperature is below ambient, heat absorbed

33

from the atmosphere competes with heat rejected to Space. The lowest achievable temperature (*i.e.*, stagnation temperature) occurs when heat absorbed from the atmosphere and the surroundings exactly balances heat rejection to Space, resulting in net-zero cooling power. The lowest achievable temperature, in this case, is ~265 K, corresponding to a maximum temperature reduction of ~35 K.

Changes in the thickness of the cover have opposite effects on the maximum cooling power and the stagnation temperature as shown in Fig. 2.7b. Increasing the cover thickness improves the thermal resistance between the emitter and the ambient by increasing the conduction path and by blocking downward radiation from the atmosphere. This thermal resistance appears to be the key feature when the emitter temperature is below ~295 K, since increasing L results in greater cooling power. Conversely, when the emitter temperature is above ~295 K, increasing L results in lower cooling power. Thus, we conclude it is advantageous to reduce the cover thickness when the emitter temperature is at or near ambient to maximize the transmission of radiation to Space. In the case when the emitter temperature is greater than ambient, a thick cover is undesirable because it prevents the ambient from cooling the hot emitter.

These observations suggest that the cover thickness can be optimized for the desired emitter temperature. In Fig. 2.7c, the cooling power (q_{net}), the heat rejected to Space (q_{space}), and the ambient heating (q_{gain}) are plotted as a function of cover thickness for $T_{emitter}$= 290 K. As L increases, the transmittance of the cover decreases according to $\sim exp\,(-L)$, decreasing the amount of desirable thermal emission that reaches Space (q_{space}). On the other hand, as L increases, the cold emitter is more thermally insulated from the surroundings since nonradiative

heating (q_{gain}) decreases according to $\sim 1/L$, following the dependence of the thermal conductance of the cover ($\sim k_{eff}/L$)). These two competing mechanisms result in an optimal cover thickness at which q_{cool} is maximized. However, in the case of BaF$_2$, the decrease in q_{space} is small with increasing cover thickness. In turn, q_{cool} does not reach a clear maximum for a range of practical cover thicknesses; instead, it plateaus. For design and cost purposes, one would likely choose the thinnest cover without compromising cooling performance at a desired operating temperature. Similarly, the cooling power of ZnS and BaF$_2$ at 290 K plateaus around 3 cm (Fig. 2.7b,c, 2.8b,c); hence we set the cover thickness to 3 cm when comparing materials.

2.7 Material Effects on Cooling Performance

In this section, we discuss how the choice of material affects the cooling performance. The effects of particle size and cover thickness were illustrated for BaF$_2$ in the previous section; we observe similar effects and trends for ZnS and polyethylene (PE) (Fig. 2.8d,e, 2.9d,e).

These materials were chosen because of their low IR absorption in the 8–13 μm range. Vibrational modes are responsible for absorption in the IR for all three materials; however, each material has different vibrational modes. Absorption peaks in PE are a result of IR absorption in C–C, and C–H bonds. For BaF$_2$, weak multi-phonon absorption typically occurs in the 8–13 μm band, giving rise to high transparency in that region.[28] Single-phonon absorption marks the opaque region and dominates above 13 μm, which means BaF$_2$ absorbs strongly at long wavelengths, as seen in Fig. 2.6. ZnS, like BaF$_2$, has multi-phonon and single-phonon absorption modes, but the single-phonon

mode is shifted to longer wavelengths.[29] Therefore, ZnS absorbs less overall thermal radiation than BaF$_2$ in Band III.
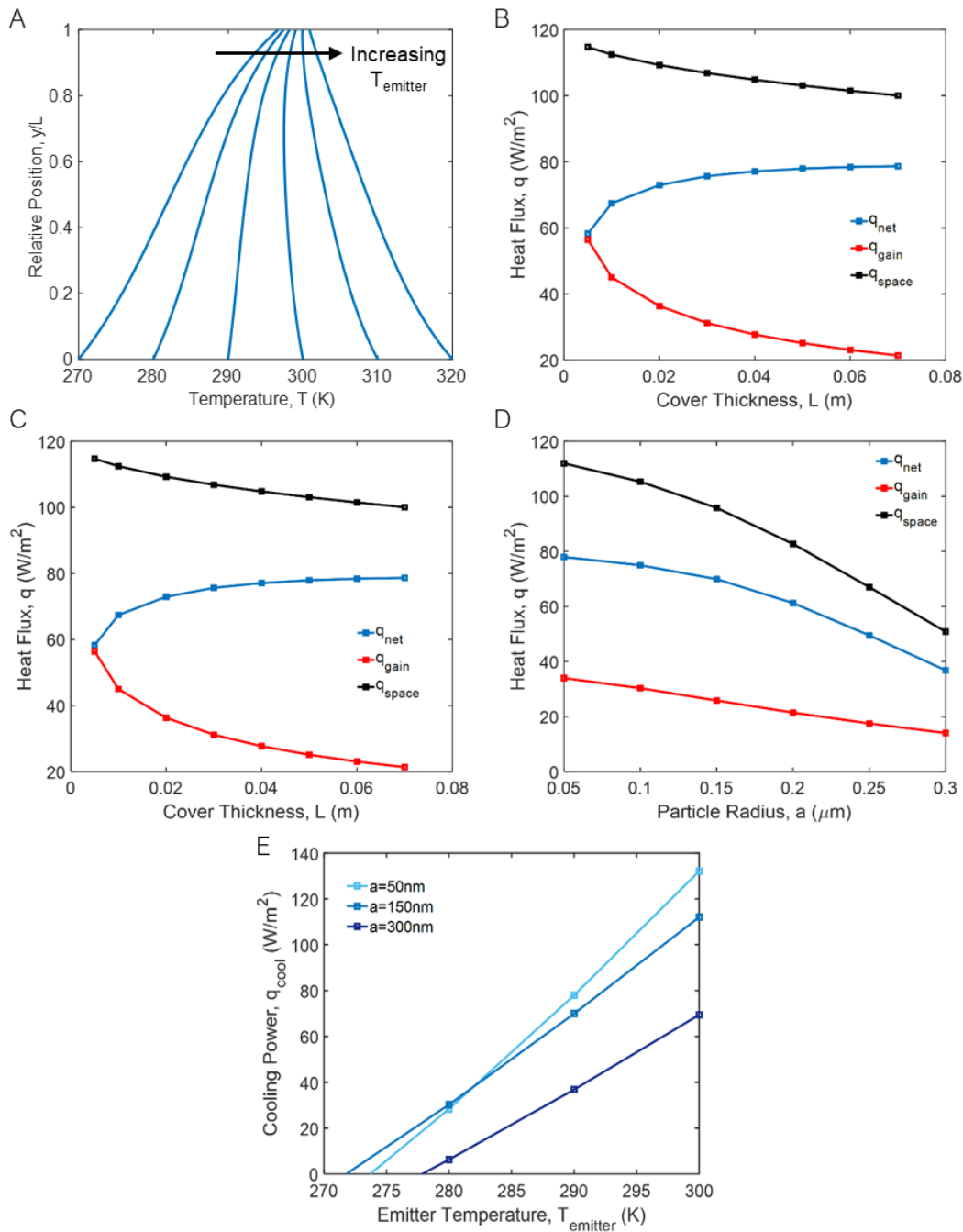
Figure 2.8. (A) Temperature profiles for a 3 cm thick ZnS cover with varying T$_{emitter}$ (90 nm particle radius, 0.01 volume fraction). Net cooling power (B) and heat flux breakdown (C) for varying ZnS cover thickness. (D) Heat flux for 3 cm ZnS cover with various particle sizes (T$_{emitter}$ = 290 K (ΔT = 10K)). (E) Net cooling power for varying ZnS particle sizes for a 3 cm thick cover.

36
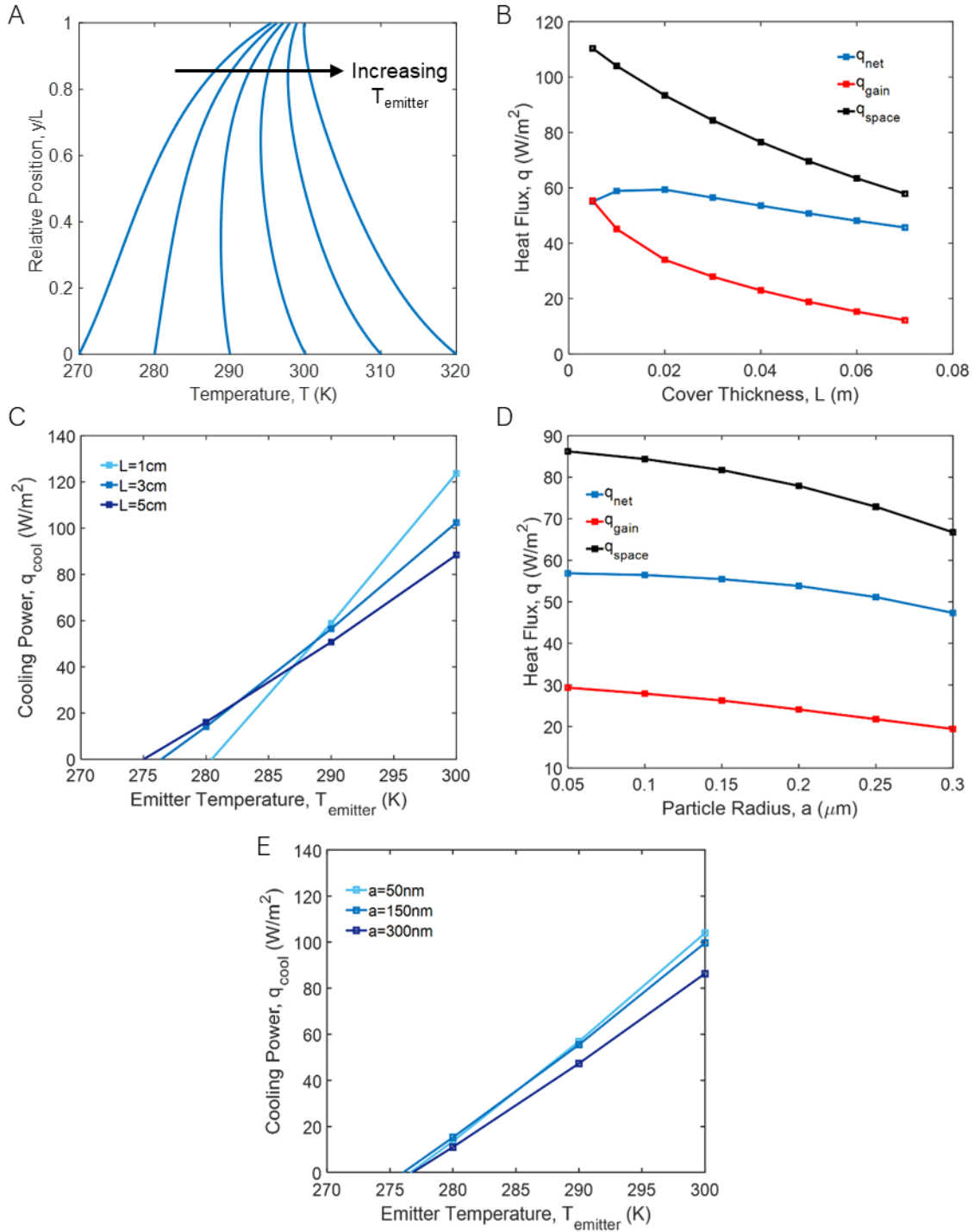
Figure 2.9. (A) Temperature profiles for a 3 cm thick PE cover with varying $T_{emitter}$ (100 nm particle radius, 0.01 volume fraction). Net cooling power (B) and heat flux breakdown (C) for varying PE cover thickness. (D) Heat flux for 3 cm PE cover with various particle sizes ($T_{emitter}$ = 290 K (ΔT = 10K)). (E) Net cooling power for varying PE particle sizes for a 3 cm thick cover.

Of the three materials considered here, BaF_2 shows the best overall performance with a stagnation temperature below 270 K and a maximum cooling rate of ~120 W/m² (Fig. 2.10a). We also observe that the approximate transmittance of BaF_2 qualitatively matches the atmospheric transmittance better than either PE or ZnS (Fig. 2.10b). We attribute the superior performance of BaF_2 at low temperatures to the relatively high absorption coefficient at long wavelengths (>13 µm). This leads to the absorption of downward atmospheric radiation in regions near the top of the cover that is insulated from the emitter at the bottom. However, at higher temperatures (near ambient), ZnS has a slightly higher cooling rate than BaF_2 due to higher transmittance at long wavelengths (>13 µm), leading to improved heat rejection through the low-transmittance bands of the atmosphere. The broadband transmittance of PE (Fig. 2.10b) results in the worst performance of the three materials. Further, the absorption coefficient for PE in the desired band is higher than ZnS and BaF_2 leading to a more pronounced decrease in q_{space} with increasing thickness (Fig. 2.9b).
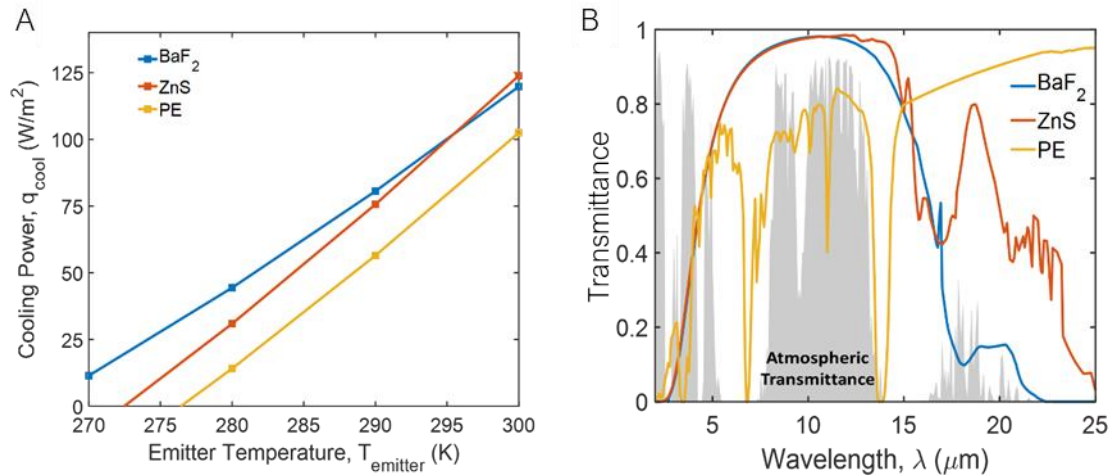
Figure 2.10. Materials effects on cooling power: (A) cooling power and (B) approximate spectral transmittance for BaF_2, ZnS, and PE. For BaF_2, $a = 150$ nm and $L = 3$ cm. For ZnS, $a = 90$ nm and $L = 3$ cm. For PE, $a = 100$ nm and $L = 3$ cm. Atmospheric transmittance is shown in gray.[16]

2.8 Conclusions

We modeled the radiative cooling performance of nanoporous covers that are selectively transparent in the atmospheric window by coupling optical properties and thermal transport. We observed that for wavelengths below 8 μm, scattering is the dominant form of extinction, while absorption dominates above 13 μm. We observed a trade-off between desirable transmittance and thermal insulation with increasing cover thickness. Thicker covers provide better thermal insulation by shielding the emitter from parasitic heat gains but are less transparent in the desired band. Out of the three materials we considered, BaF_2 transmits the most in the 8–13 μm band and absorbs the strongest at long wavelengths (above 13 μm). We show that a 3 cm BaF_2 cover with 99% porosity and a 150 nm scattering radius achieves the best overall cooling performance with a stagnation temperature of ~265 K and a maximum cooling rate of ~120 W/m^2. This study offers design guidelines for radiative cooling using nanoporous covers, and a framework for future materials optimization. Nanoporous materials may eliminate the need for a sunshade and a selective surface while providing high-performance radiative cooling at deep sub-ambient temperatures.

2.9 References

(1)   Raman, A. P.; Anoma, M. A.; Zhu, L.; Rephaeli, E.; Fan, S. Passive Radiative Cooling below Ambient Air Temperature under Direct Sunlight. *Nature* **2014**, *515* (7528), 540–544. https://doi.org/10.1038/nature13883.

(2)   Addeo, A.; Monza, E.; Peraldo, M.; Bartoli, B.; Coluzzi, B.; Silvestrini, V.; Troise, G. Selective Covers for Natural Cooling Devices. *Nuovo Cim. C* **1978**, *1* (5), 419–429. https://doi.org/10.1007/BF02507668.

(3)   Berdahl, P.; Martin, M.; Sakkal, F. Thermal Performance of Radiative Cooling Panels. *Int. J. Heat Mass Transf.* **1983**, *26* (6), 871–880. https://doi.org/10.1016/S0017-9310(83)80111-2.

(4)   Addeo, A.; Nicolais, L.; Romeo, G.; Bartoli, B.; Coluzzi, B.; Silvestrini, V. Light Selective Structures for Large Scale Natural Air Conditioning. *Sol. Energy* **1980**, *24* (1), 93–98. https://doi.org/10.1016/0038-092X(80)90024-9.

(5)   Gentle, A. R.; Dybdal, K. L.; Smith, G. B. Polymeric Mesh for Durable Infra-Red Transparent Convection Shields: Applications in Cool Roofs and Sky Cooling. *Sol. Energy Mater. Sol. Cells* **2013**, *115*, 79–85. https://doi.org/10.1016/j.solmat.2013.03.001.

(6)   Nilsson, N. A.; Eriksson, T. S.; Granqvist, C. G. Infrared-Transparent Convection Shields for Radiative Cooling: Initial Results on Corrugated Polyethylene Foils. *Sol. Energy Mater.* **1985**, *12* (5), 327–333. https://doi.org/10.1016/0165-1633(85)90002-4.

(7)   Naghshine, B. B.; Saboonchi, A. Optimized Thin Film Coatings for Passive Radiative Cooling Applications. *Opt. Commun.* **2018**, *410* (October 2017), 416–423. https://doi.org/10.1016/j.optcom.2017.10.047.

(8)   Nilsson, T. M. J.; Niklasson, G. A. Radiative Cooling during the Day: Simulations and Experiments on Pigmented Polyethylene Cover Foils. *Sol. Energy Mater. Sol. Cells* **1995**, *37* (1), 93–118. https://doi.org/10.1016/0927-0248(94)00200-2.

(9)   Nilsson, T. M. J.; Niklasson, G. A.; Granqvist, C. G. A Solar Reflecting Material for Radiative Cooling Applications: ZnS Pigmented Polyethylene. *Sol. Energy Mater. Sol. Cells* **1992**, *28* (2), 175–193. https://doi.org/10.1016/0927-0248(92)90010-M.

(10)   Chen, Z.; Zhu, L.; Raman, A.; Fan, S. Radiative Cooling to Deep Sub-Freezing Temperatures through a 24-h Day-Night Cycle. *Nat. Commun.* **2016**, *7*, 1–5. https://doi.org/10.1038/ncomms13729.

(11)   Bosi, S. G.; Bathgate, S. N.; Mills, D. R. At Last! A Durable Convection Cover for Atmospheric Window Radiative Cooling Applications. *Energy Procedia* **2014**, *57*, 1997–2004. https://doi.org/10.1016/j.egypro.2014.10.064.

(12)   Bathgate, S. N.; Bosi, S. G. A Robust Convection Cover Material for Selective Radiative Cooling Applications. *Sol. Energy Mater. Sol. Cells* **2011**, *95* (10), 2778–2785. https://doi.org/10.1016/j.solmat.2011.05.027.

(13)   Benlattar, M.; Oualim, E. M.; Mouhib, T.; Harmouchi, M.; Mouhsen, A.; Belafhal, A. Thin Cadmium Sulphide Film for Radiative Cooling Application. *Opt. Commun.* **2006**, *267* (1), 65–68. https://doi.org/10.1016/j.optcom.2006.06.050.

(14)   Benlattar, M.; Oualim, E. M.; Harmouchi, M.; Mouhsen, A.; Belafhal, A. Radiative Properties of Cadmium Telluride Thin Film as Radiative Cooling Materials. *Opt. Commun.* **2005**, *256* (1–3), 10–15. https://doi.org/10.1016/j.optcom.2005.06.033.

(15)   ASTM. Reference Solar Spectral Irradiance: Air Mass 1.5.

(16)   Berk, A.; Anderson, G. P.; Acharya, P. K.; Bernstein, L. S.; Muratov, L.; Lee, J.; Fox, M.; Adler-Golden, S. M.; Chetwynd, Jr., J. H.; Hoke, M. L.; Lockwood, R. B.; Gardner, J. A.; Cooley, T. W.; Borel, C. C.; Lewis, P. E.; Shettle, E. P. ModTran 5: 2006 Update. In *Proc SPIE Int Soc Opt Eng*; 2006; Vol. 6233, pp 62331F-62331F – 8. https://doi.org/10.1117/12.665077.

(17)   Tang, G. H.; Bi, C.; Zhao, Y.; Tao, W. Q. Thermal Transport in Nano-Porous Insulation of Aerogel: Factors, Models and Outlook. *Energy* **2015**, *90*, 701–721. https://doi.org/10.1016/j.energy.2015.07.109.

(18)   Strobach, E.; Bhatia, B.; Yang, S.; Zhao, L.; Wang, E. N. High Temperature Annealing for Structural Optimization of Silica Aerogels in Solar Thermal Applications. *J. Non. Cryst. Solids* **2017**, *462*, 72–77. https://doi.org/10.1016/j.jnoncrysol.2017.02.009.

(19)   McEnaney, K.; Weinstein, L.; Kraemer, D.; Ghasemi, H.; Chen, G. Aerogel-Based Solar Thermal Receivers. *Nano Energy* **2017**, *40* (May), 180–186. https://doi.org/10.1016/j.nanoen.2017.08.006.

(20)   Zhao, L.; Yang, S.; Bhatia, B.; Strobach, E.; Wang, E. N. Modeling Silica Aerogel Optical Performance by Determining Its Radiative Properties. *AIP Adv.* **2016**, *6* (2). https://doi.org/10.1063/1.4943215.

(21)   Bohren, C. F.; Huffman, D. R. Absorption and Scattering of Light by Small Particles. *Research supported by the University of Arizona and Institute of Occupational and Environmental Health New York Wiley Interscience 1983*. 1983. https://doi.org/10.1017/S0263574798270858.

(22)   Drolen, B. L.; Tienf, C. L. Independent and Dependent Scattering in Packed-Sphere Systems. *J. Thermophys. Heat Transf.* **1987**, *1* (1), 63–68. https://doi.org/10.2514/3.8.

(23)   Palik, E. *Handbook of Optical Constants of Solids: Index*; 1998.

(24)   Thomas, M. E.; Tropf, W. J. *Handbook of Optical Constants of Solids*; 1997. https://doi.org/10.1016/B978-012544415-6.50125-4.

(25)   Modest, M. F. Radiative Heat Transfer. In *Radiative Heat Transfer (Second Edition)*; 2003. https://doi.org/10.1016/B978-012503163-9/50023-0.

(26)   Soleimani Dorcheh, A.; Abbasi, M. H. Silica Aerogel; Synthesis, Properties and Characterization. *J. Mater. Process. Technol.* **2008**, *199* (1), 10–26. https://doi.org/10.1016/j.jmatprotec.2007.10.060.

(27)   Günay, A. A.; Kim, H.; Nagarajan, N.; Lopez, M.; Kantharaj, R.; Alsaati, A.; Marconnet, A.; Lenert, A.; Miljkovic, N. Optically Transparent Thermally Insulating Silica Aerogels for Solar Thermal Insulation. *ACS Appl. Mater. Interfaces* **2018**, *10* (15), 12603–12611. https://doi.org/10.1021/acsami.7b18856.

(28)   Thomas, M. E.; Tropf, W. J. Barium Fluoride (BaF2). *Handb. Opt. Constants Solids* **1997**, 683–699. https://doi.org/http://dx.doi.org/10.1016/B978-012544415-6.50125-4.

(29)   Palik, E. D.; Addamiano, A. Zinc Sulfide (ZnS). In *Handbook of Optical Constants of Solids*; 2012; Vol. 1, pp 597–619. https://doi.org/10.1016/B978-0-08-054721-3.50032-0.

Chapter 3: Enhanced Solar Scattering Through Controlled Nanofiber Morphology

3.1 Motivation

Since solar irradiation outweighs the power density of near-ambient thermal emission, achieving high levels of spectral selectivity, specifically solar reflectance, is necessary to observe a net cooling effect during the daytime. Whereas selective emitters generally require conduction of heat between the emitter and the object to be cooled,[1] the use of selective covers has been referred to as *direct* radiative cooling because it allows the object to directly radiate heat to Space (assuming the object has sufficient thermal emittance such as the human skin or a body of water) (Fig. 3.2a). To achieve the desired spectral selectivity, selective covers typically consist of materials that have been nanostructured to impart solar reflectance but are otherwise inherently transparent in the long-wave IR (LW-IR).[1–4] One potential advantage of using a selective cover is that solar and atmospheric heating can be spatially decoupled from infrared emission.[5] This decoupling allows for parasitic heating to occur at the cover rather than the radiator, resulting in a theoretical cooling power advantage when comparing a selective cover to a selective emitter given the same level of selectivity and parasitic heating (see Fig. 3.1). This advantage was recently proposed[5] and experimentally demonstrated using a polyethylene (PE) aerogel,[2] resulting in record-low stagnation temperatures for a non-evacuated system.
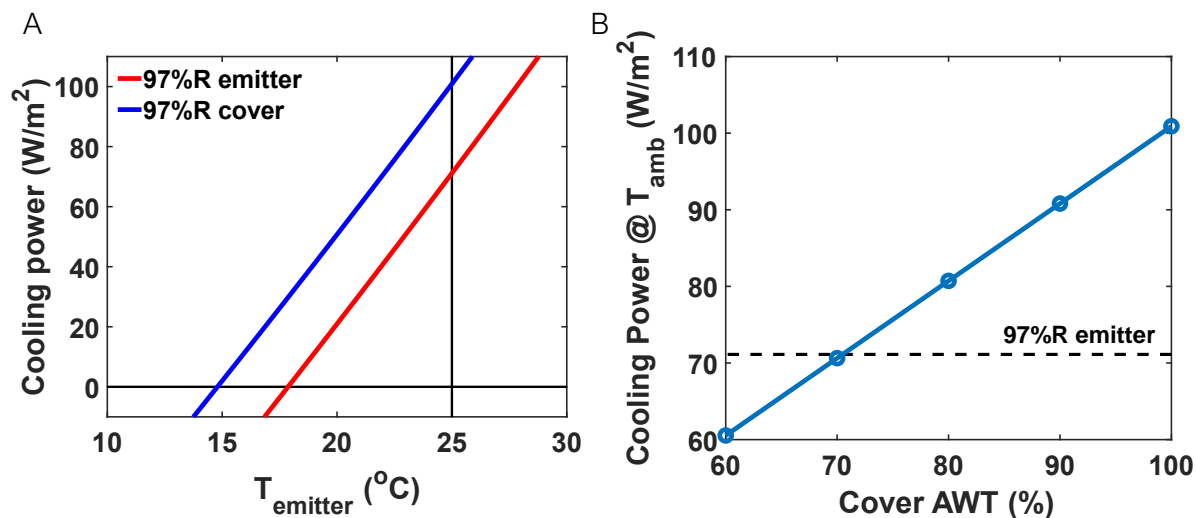
Figure 3.1. (A) Simulated cooling power comparing a selective emitter with 97% solar weighted AM1.5G reflectance (SR) (remaining 3% is absorbed) and blackbody thermal emittance, versus a selective cover with the same solar properties and 100% atmospheric-window-weighted total transmittance (AWT), paired with a blackbody emitter. (B) Simulated cooling power as a function of cover AWT. At ambient temperature, the cooling power linearly decreases as the cover transmittance is decreased. Above the dashed line, the selective cover can achieve better cooling performance than the selective emitter. T_{air}=25°C, h_{eff}=5 W/m²K, and solar irradiance are assumed to be normally incident at 1000 W/m².

Despite the potential advantages of selective covers, achieving precise control over the morphology of nanostructures remains challenging. Current approaches primarily rely on the extraction of a sacrificial phase (*i.e.*, immiscible liquids[2] or solid nanoparticles[1]) to leave behind nanoscale voids. However, because of the high-volume fraction of the sacrificial phase needed to impart solar reflection and the intrinsic difficulty in controlling the size of voids introduced during drying/extraction, these methods have produced films with a wide range of void sizes, and in turn, undesirable scattering/reflection in the LW-IR.

Here, we control the morphology of polyacrylonitrile (PAN) nanofibers via electrospinning and investigate how the scattering and absorption properties of PAN nanofiber covers (nanoPAN) depend on fiber morphology. We chose PAN because of its electrospinning compatibility, which

44
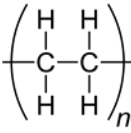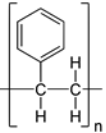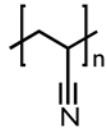
allows us to fabricate fibers with suitable structure length scales for solar scattering (0.2 – 1 μm mean diameter) while tuning their morphology to include spherical, ellipsoidal, and cylindrical features. These experimental studies are complemented by electromagnetic simulations to elucidate scattering mechanisms. The ellipsoidal beaded nanofibers (5 wt% PAN) exhibit the best combination of radiative properties for direct radiative cooling because of their additive dielectric resonances. NanoPAN covers based on this fiber morphology achieve >95% solar weighted AM1.5G reflectance (SR) and >70% atmospheric-window-weighted total transmittance (AWT). Through outdoor cooling experiments, we demonstrate that nanoPAN covers can cool black surfaces, which have minimal solar reflectance. This result is significant for alleviating urban heat island effects and seasonal radiative cooling since many relevant surfaces have unfavorable solar reflectance but good thermal emittance (*e.g.*, concrete, asphalt, human skin, water, etc.).[6] Equally important is that our work on tailoring nanofiber morphology to enhance solar scattering may enable the use of unconventional materials and lower purity feedstocks, such as recycled PE, in direct radiative cooling applications.

3.2 Choosing Polymers for Radiative Cooling Covers

From Chapter 2, we realize that candidate materials for radiative cooling covers must have high transparency (*i.e.*, low absorption) in infrared regions. Several chalcogenide materials possess low extinction coefficients in the IR, allowing them to be used as convective covers. Introducing opacity to scatter solar radiation is challenging with chalcogenide covers, therefore, they typically do not function as a dual convective cover and solar shield.[7,8] On the other hand, polymers can be designed with pores or scattering particles with characteristic length scales to block solar radiation, however, most polymers absorb in the infrared due to their molecular structure.[9]

Absorption in polymers is caused by stretching and bending between molecular bonds of primarily, carbon, hydrogen, nitrogen, and oxygen. The various combination of bonds which include single, double, and triple bonds, gives rise to functional groups. Each functional group has characteristic absorption peaks in the IR, hence, polymers with multiple side chains and functional groups will typically absorb more. For example, polyethylene (PE) is not only the most common polymer used for convective covers, but overall, the most commonly used material for convective covers because of its cost, abundance, and favorable optical properties.[10] PE is only comprised of C-H and C-C bonds, which enables retention of high transmission in the IR.

In addition to intrinsic optical properties, a polymer that can be designed to have a specific scattering diameter is desirable to scatter the solar spectrum (Table 3.1). In this study, we use electrospinning as a method that has been shown to have strong control over the deposition of polymer nanofibers (see section 3.3 below). Thus, polymers compatible with electrospinning are considered. Electrospinning PE is difficult and requires a complicated setup with constant heating and hazardous solvents, therefore, PE was not used in this study. Polystyrene is an easily electrospun polymer that can be used to fabricate fibers of varying morphologies,[11] however, the aromatic functional group causes undesirable absorption in the atmospheric window. Polyacrylonitrile (PAN), like polystyrene, is a commonly used polymer for electrospinning that possesses a functional group in addition to the C-H backbone. The triple nitrogen bond in PAN, however, has lower absorption intensity and lies slightly outside the atmospheric window, making it a promising candidate for a passive radiative cooling cover (Table 3.1).

Polymer	Polyethylene	Polystyrene	Polyacrylonitrile
Structure			
Optical Properties	✓ ✓	✗ ✗	✓
Electrospinning capabilities	✗ ✗	✓ ✓	✓ ✓

Table 3.1. Comparing the optical properties and electrospinning capabilities of three polymers to determine if the necessary criteria for a passive radiative cooling cover are met. The following symbols denote: "✗✗" difficult, "✓✓" excellent, and "✓" good.

3.3 Morphology Dependent Radiative Cooling of PAN Nanofibers

Electrospinning is a versatile tool that allows us to control the morphology of polymer fibers by tuning various spinning parameters. Voltage, polymer concentration, spin time, stage height, flowrate, and syringe gauge are all parameters that can affect the resulting electrospun fiber.[12] For our study, we vary the polymer solution concentration from 2.5 to 9 PAN wt% and spin time from 10 to 60 mins. These variables represent the simplest tuning parameters to change fiber morphology and film thickness. Specifically, four different concentrations of PAN (2.5 wt%, 5 wt%, 7 wt%, 9 wt%) are dissolved in dimethylformamide (DMF) and electrospun. PAN concentration directly influences the rheological properties of the solution, which in turn influences the morphology of the spun fibers.[13,14] As seen in Fig. 3.2b, the resulting nanofibers are qualitatively opaque in the visible region but transparent in the IR. These are necessary traits to scatter solar radiation but allow emission in the atmospheric windows.
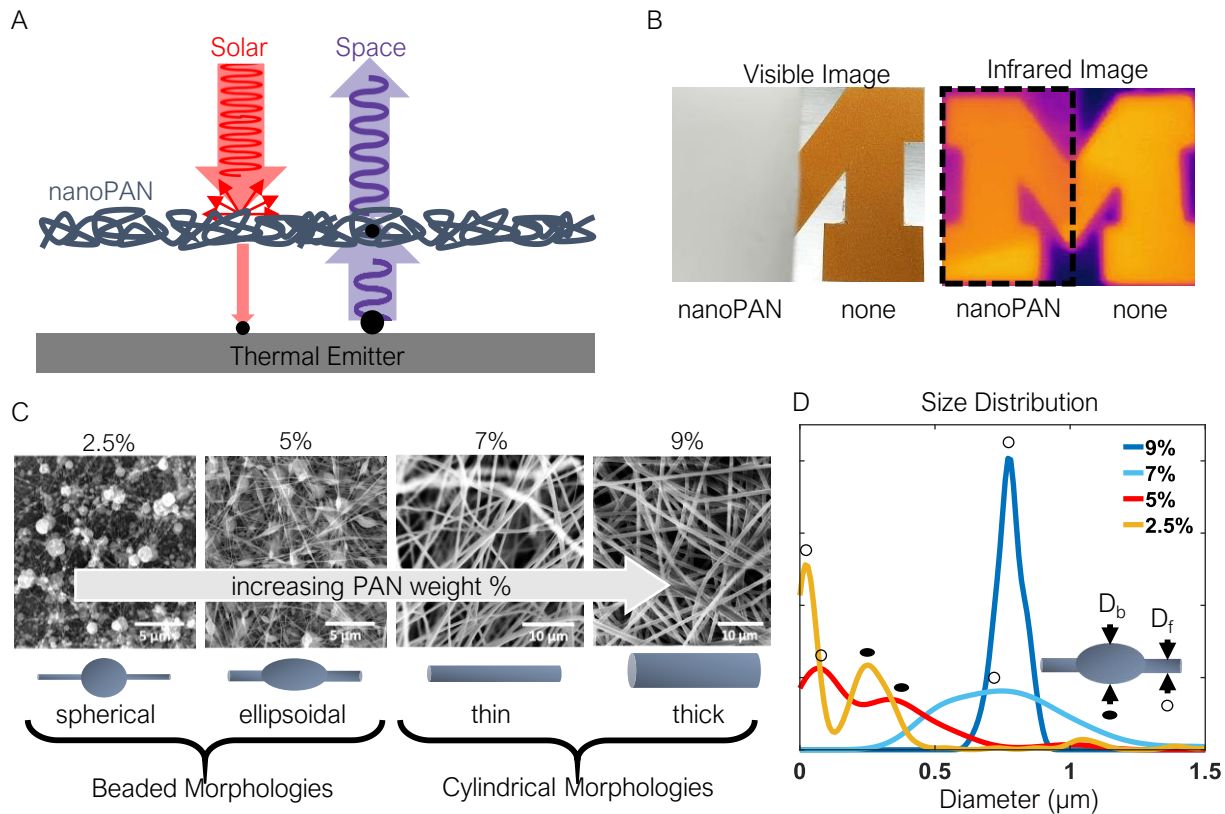
Figure 3.2. (A) Direct radiative cooling using infrared-selective transparent covers. (B) Visible and infrared images of PAN nanofiber films (nanoPAN) covering a thermally emitting block M print on top of an unpolished aluminum sheet. (C) Morphological control of polyacrylonitrile (PAN) nanofibers via electrospinning. SEM images of electrospun 2.5, 5, 7, and 9 wt% PAN fibers, with scale bars inset. (D) Size distribution of 2.5, 7, 5, and 9 wt% PAN nanofibers.

Fiber morphologies of the varying PAN concentration, imaged using SEM, are shown in Fig. 3.2c.

Both the 2.5 wt% and 5 wt% solutions produced fiber morphologies with beads and thin cylindrical

interconnections. The 5 wt% solutions resulted in more elongated beads (*i.e.*, ellipsoids). For these

relatively low concentrations, and hence viscosities, high surface tension causes instabilities in

Taylor cone formation resulting in droplets and bead formation.[15,16] In contrast, the 7 wt% and 9

wt% concentrations produced 'thin' and 'thick' cylindrical fibers, respectively. As the PAN

concentration is increased, viscous forces dominate, resulting in more uniform cylindrical

fibers.[14,15] The size distribution of the cylindrical segments and beads is shown in Fig. 3d. Both

the ellipsoidal beaded (5 wt%) and thin cylindrical (7 wt%) nanofibers feature relatively broader

48

particle/fiber size distributions compared to the spherical beaded (2.5 wt%) and thick cylindrical (9 wt%) morphologies.

3.4 Optical Dependence of Nanofiber Covers

Fig. 3.3 shows the effect of solution concentration on the optical properties of the films (for a fixed spin time of 60 mins), characterized using UV-Vis-NIR and FTIR integrating sphere measurements. The films exhibit broadband reflectance across the solar spectrum that gradually peaks in the visible/NIR, followed by a drop-off in the mid-IR (Fig. 3.3a,b). Consistent with Mie theory,[17] increasing the PAN concentration, and thus the scattering diameter, shifts the reflectance peak to longer wavelengths (see Fig. 3.4). The reflectance of the smaller diameter nanofibers (2.5 through 7 wt%) decays by ~8 μm, leaving behind the interference fringes characteristic of the supporting PE films (see Fig. 3.5). In contrast, the larger mean diameter characteristic of the thick cylindrical nanofibers results in a gradual scattering tail that extends into the main atmospheric window, producing undesirable infrared reflectance (Fig. 3.3b).
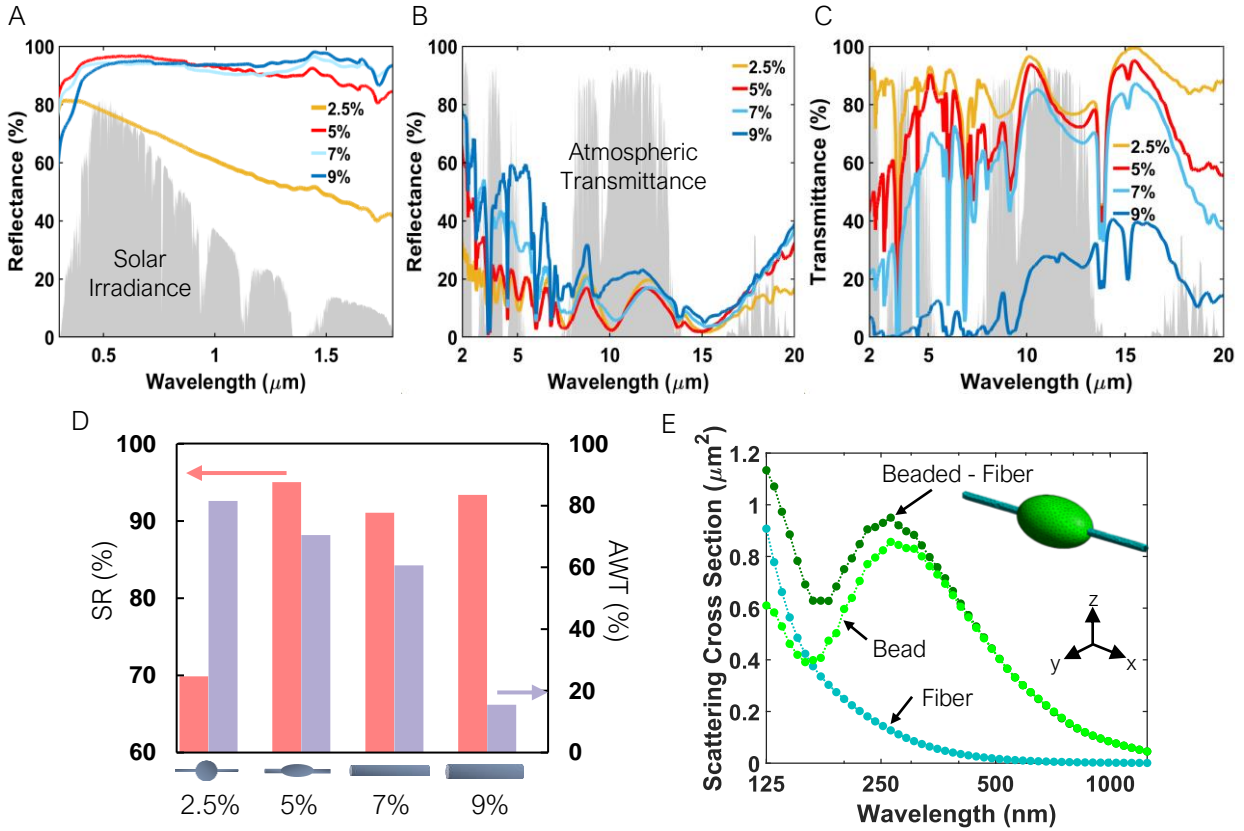
Figure 3.3. Total spectral reflectance measured using (A) UV-Vis-NIR and (B) FTIR for 60 min electrospun nanofibers. (C) Total spectral transmittance measured using FTIR. Atmospheric transmittance[18] and AM1.5G[19] spectra are shown for reference. (D) Atmospheric weighted infrared transmittance (AWT) and solar weighted AM1.5G reflectance (SR) of PAN nanofibers. (E) Simulated spectral scattering cross-section of a cylindrical fiber, ellipsoidal bead, and ellipsoidal beaded fiber using SCUFF-EM.[20,21] Minor diameter of the bead, $D_b = 436$ nm, and average diameter of the fiber, $D_f = 67.5$ nm, were chosen to match measured mean dimeters in Fig. 3.2d.

50
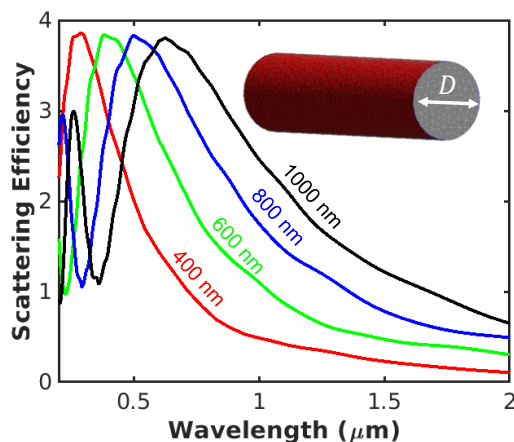
Figure 3.4. Spectral scattering efficiency of cylindrical PAN fibers with increasing diameter calculated using SCUFF-EM.[20,21] The scattering efficiency is redshifted with increased fiber diameters. The geometric cross-sections of the fibers in the x-y plane are rectangular (D*L). For all simulations, the length of the fiber was sufficiently long such that no additional cavity modes appeared in the results.
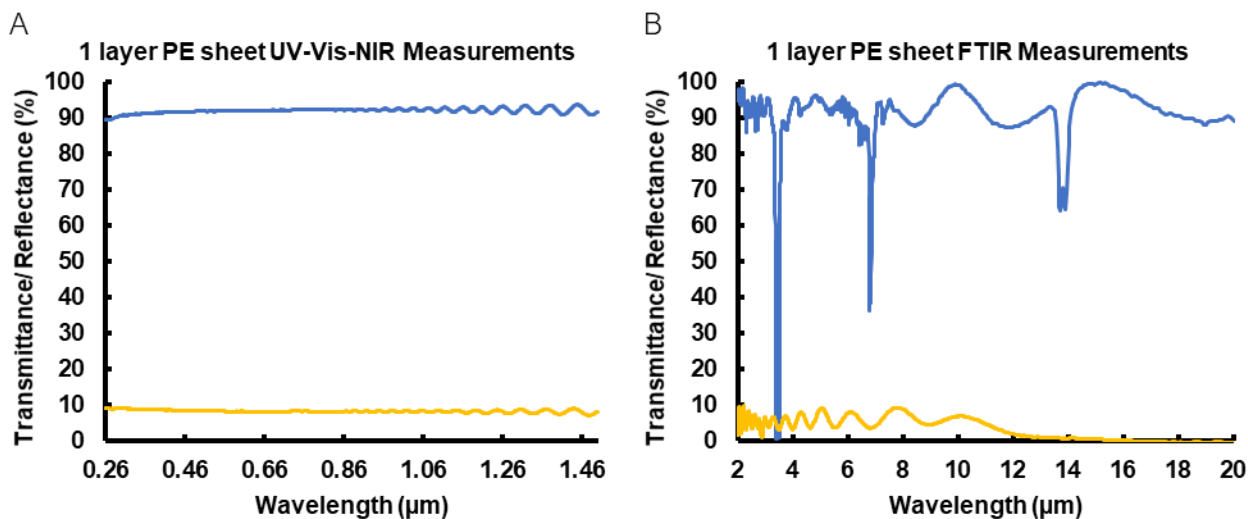
Figure 3.5. Transmittance and reflectance of a single-layer polyethylene Glad® ClingWrap film, measured using (A) UV-Vis-NIR and (B) FTIR.

The infrared transmittance generally decreases with increasing PAN concentration (Fig. 3.3c). This result is consistent with the notion that light is more likely to be attenuated by thicker materials (see Fig. 3.6, Table 3.2-3.3 for film thicknesses). Apart from the thick cylindrical

51

nanofibers (9 wt%), absorption is responsible for a nearly linear attenuation in AWT with increasing PAN. For the thick cylindrical nanofibers, on the other hand, both scattering and absorption attenuate infrared radiation, resulting in a more pronounced loss in AWT (Fig. 3.3d).
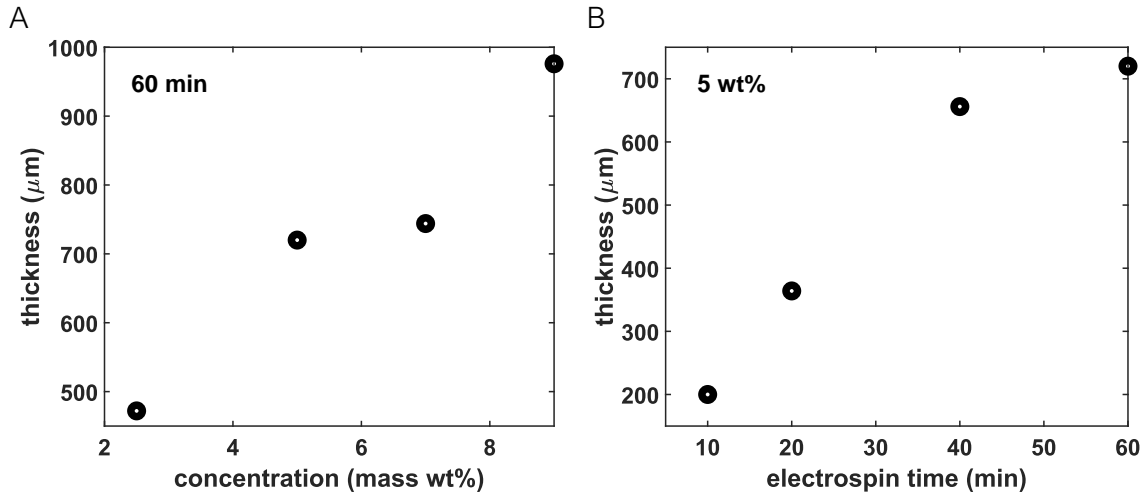
Figure 3.6. Measured nanoPAN film thicknesses as a function of (A) PAN concentration (2.5, 5, 7, 9 wt%) for 60 min electrospin time, and (B) electrospin time (10, 20, 40, 60 min) for a fixed concentration (5 wt%).

5%nanoPAN	10 min	20 min	40 min	60 min
mass/area (g/cm²)	0.0043	0.0063	0.0064	0.0072
film thickness (µm)	200	364	656	720
Volume fraction	0.1835	0.1453	0.0821	0.0841

Table 3.2. Surface density (mass/area) and film thickness for 5 wt% nanoPAN referenced in Fig. 3.12. Film thickness was measured using an optical microscope (Zeiss Axio Lab A1). The resulting PAN volume fraction increases with increasing electrospin time.

60 min	2.5%	5%	7%	9%
mass/area (g/cm²)	0.0042	0.0072	0.0075	0.0139
film thickness (µm)	472	720	744	976
Volume fraction	0.0745	0.0841	0.0849	0.1205

Table 3.3. Surface density (mass/area) and film thickness for nanoPAN referenced in Fig. 3.3 a-c. Film thickness was measured using an optical microscope (Zeiss Axio Lab A1). The resulting PAN volume fraction generally increases with increasing concentration.

Overall, the ellipsoidal beaded nanofibers (5 wt%) exhibit the best combination of radiative properties. Specifically, that morphology has an exceptional SR of 95%, which does not follow

the general trend formed by the other three morphologies (Fig. 3.3d). To understand why that specific morphology exhibits higher solar reflectance, we compare the electromagnetic response of this composite structure to its constituent structures (bead, cylinder) using SCUFF-EM.[20,21] The resulting cross-section can be largely explained by a sum of the individual cross-sections of the bead and cylinder (Fig. 3.3e). The cylindrical fibers scatter shorter wavelengths relative to the beads because of their smaller characteristic length scale. We should note, however, that the combination of structures and length scales in the ellipsoidal beaded fiber morphology results in a higher solar-weighted scattering efficiency than either the fiber or bead alone. This is due to the smaller geometrical cross-section of the beaded fiber than the sum of the constituent structures, which results from overlapping volumes in the beaded fiber. In addition to morphological effects, polydispersity can also be responsible for broadening the overall solar reflectance. However, the 5 wt% beaded morphology exhibits notably higher SR than the 7 wt% cylindrical geometry, despite having similar polydispersity. This comparison suggests that polydispersity cannot entirely explain the difference in SR. Thus, electrospinning provides us with a means to include cylindrical and bead morphologies in a mechanically interconnected system and leverage the scattering properties of both dielectric micro/nanostructures.

3.5 Outdoor Cooling Performance

We conducted outdoor experiments to compare the daytime stagnation temperature of a reference blackbody surface (BB) with and without the nanoPAN cover (see Fig. 3.7 for BB spectral measurements). Based on the UV-Vis-NIR and FTIR results, discussed in the previous section, the ellipsoidal beaded morphology (5 wt% PAN) was chosen as the best candidate for daytime cooling

tests. The nanoPAN films were scaled up from 6 to 40 cm^2 for our outdoor measurements while maintaining their spectral properties (see Fig. 3.8 for optical measurements).
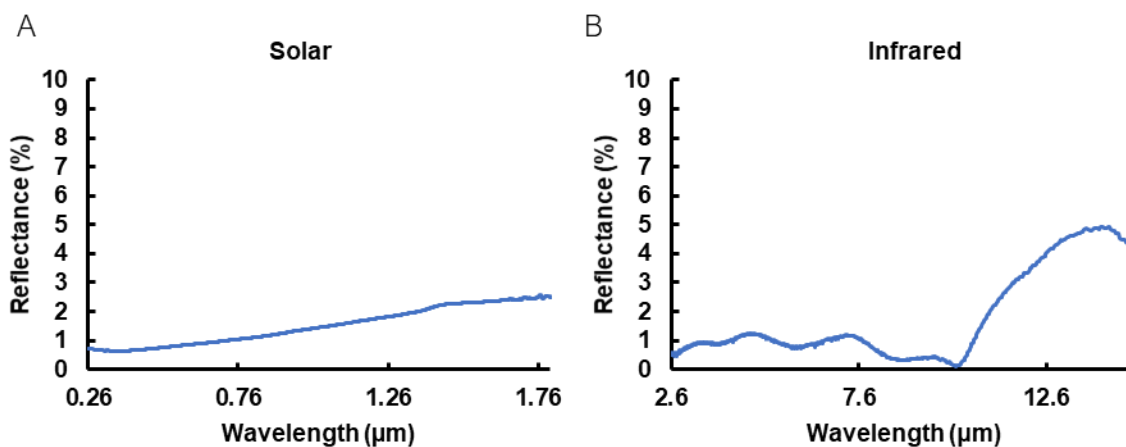
Figure 3.7. (A) Total reflectance of our reference blackbody surface (Metal Velvet^{TM} Acktar) measured using UV-Vis-NIR. (B) Specular reflectance of the blackbody surface measured using FTIR.
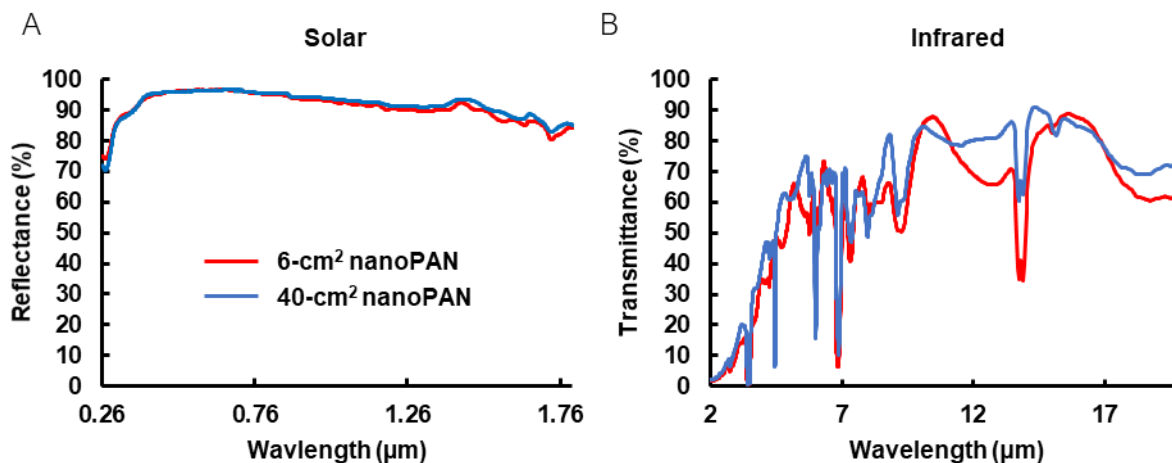
Figure 3.8. (A) Total reflectance (measured using UV-Vis-NIR) and (B) specular transmittance (measured using FTIR) of the 5 wt% scaled-up 40 cm^2 nanoPAN films (blue) used in our outdoor measurements show good agreement with the corresponding 6 cm^2 nanoPAN films (red). Differences in the IR are attributed to the presence of an additional PE sheet in the 6 cm^2 nanoPAN films, which was used to ensure that the samples were not damaged during handling and mounting within the instruments.
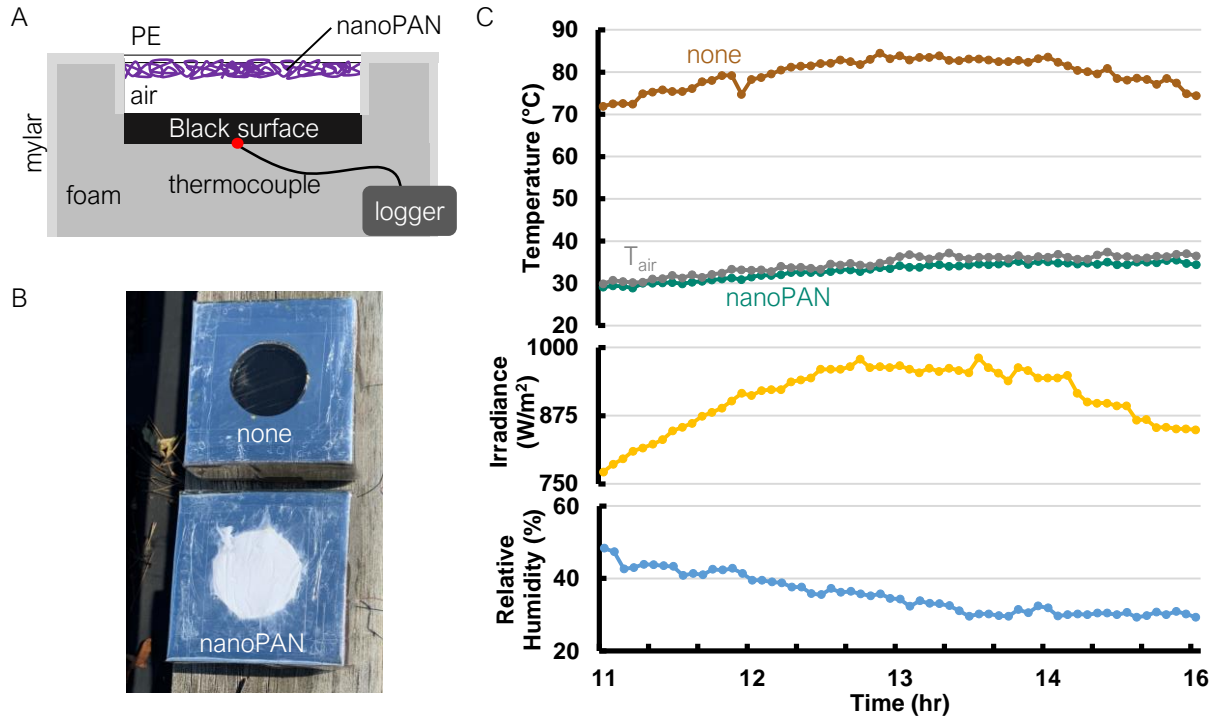
Figure 3.9. (A) Schematic and (B) images of the outdoor experimental setup used to measure the effect of the nanoPAN cover on the stagnation temperature of a reference blackbody surface (BB) under daytime solar irradiation. The thermocouple measures the temperature of the BB. A PE film is used as a convection cover in both cases (see Fig. 3.5 for PE optical measurements). (C) BB surface temperatures showing a ~50°C temperature difference between the two cases (without (none) and with nanoPAN). Also shown are the measured air temperature, solar irradiance, and relative humidity during the 4-hour test period.

The stagnation temperature of the two configurations (with and without nanoPAN) was simultaneously measured on a clear July day in Ann Arbor, Michigan. Fig. 3.9c shows a four-hour segment encompassing the peak solar hours. We note that the local air temperature (T_{air}) measured at our experimental location continues to increase throughout the day and is relatively high because the setup is mounted on a rubber roof (see Fig. 3.10a). By shielding the BB with the nanoPAN cover, a notable ~50°C reduction in stagnation temperature is observed under peak solar irradiance. Furthermore, the BB surface reaches as low as 3°C below the ambient temperature during peak solar hours despite being exposed to ~960 W/m² of solar irradiation. Our predicted stagnation temperature based on the measured optical properties of the materials and the recorded outdoor

55

condition during our experiment is in good agreement with our results (modeling details are provided in Fig. 3.10b). Overall, our results demonstrate that the addition of scattering nanofibers resulted in a significant temperature reduction for highly absorbing surfaces. Slightly lower sub-ambient temperatures may be expected with emitters that have higher SR values. Nonetheless, the versatility in the solar reflectance properties of the radiating surface, afforded by the nanoPAN cover, is important for the widespread deployment of direct radiative cooling approaches. In addition, if aesthetic considerations are deemed important, nanoPAN may also be advantageous over specular films because of its diffuse appearance.
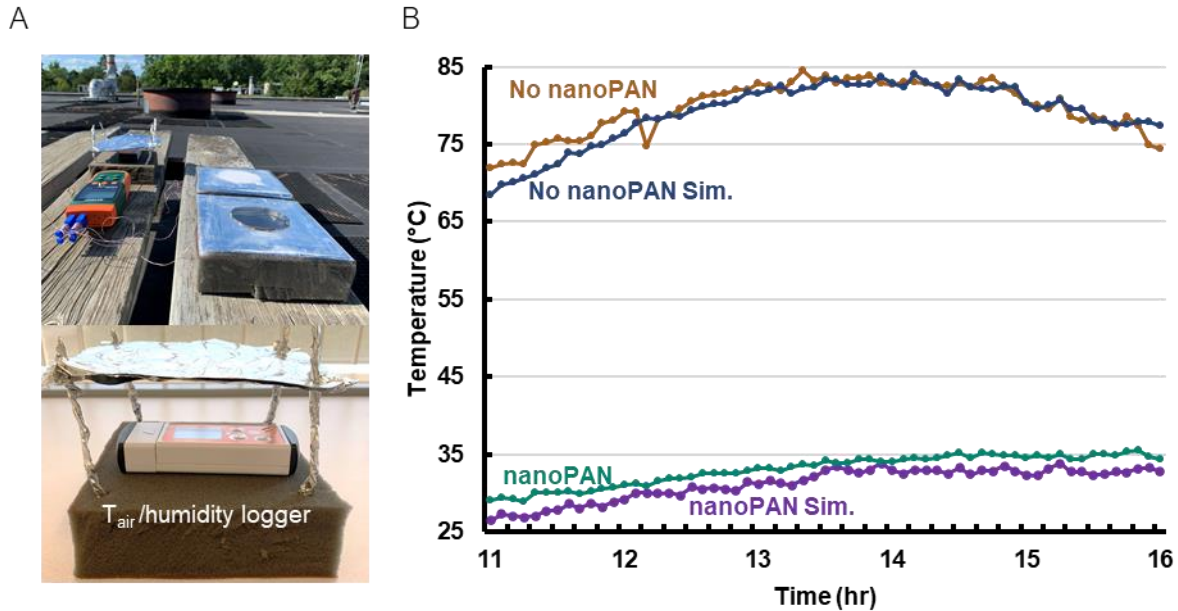
Figure 3.10. (A) Image of the outdoor rooftop experiment showing the side-by-side nanoPAN and no-nanoPAN setup and placement of the T_{air}/humidity logger under a foil sunshade. (B) Simulated time-dependent stagnation temperatures (Sim.) of the reference blackbody (BB) surface (Metal Velvet^{TM} Acktar) with and without nanoPAN under outdoor conditions corresponding to Fig. 3.9. Measured spectral properties of BB and nanoPAN are provided in Fig. 3.7 and 3.8. The effective heat transfer coefficient (h_{eff}) was used as a fitting parameter in the model. $h_{eff} = 9.5$ W/m^{2}K was determined by fitting the model to experimental data at the peak solar irradiance (for both cases). Differences between our simulated and measured values are attributed to parasitic heating of the test enclosure due to imperfect reflectance of the mylar coating and exposed foam insulation. A description of the model is provided below.

An energy balance around the emitting surface was used to calculate the net cooling power Q_{net} as seen in Fig. 3.10b:

$$Q_{net} = Q_e - Q_{sol} - Q_{amb-rad} - Q_{amb-nrad} \qquad \text{(Eq. 3.1)}$$

where Q_e is the emitted power, Q_{sol} is the absorbed solar (AM1.5G) power, $Q_{amb-rad}$ is the power due to radiative heat exchange with the ambient, and $Q_{amb-nrad}$ is the power due to nonradiative heat exchange with the ambient. The incident power from space was neglected because of its near-zero absolute temperature (~3 K).

The emitted power is a function of both temperature and wavelength as given by:

$$Q_e = 2\pi \int_0^\infty \int_0^{\pi/2} \varepsilon_{eff}(\lambda) \, I_b(T_e, \lambda) \, cos\theta \, sin\theta \, d\theta \, d\lambda \qquad \text{(Eq. 3.2)}$$

where $\lambda, \theta, T_e, \varepsilon_{eff}, I_b$ are the wavelength, polar angle, emitter temperature, the effective emissivity of the emitter and cover assembly, and blackbody intensity $I_b(T, \lambda) = \frac{2hc^2}{\lambda^5 (e^{hc/\lambda k_B T} - 1)}$ given by Planck's law, respectively.

The effective wavelength-dependent emissivity of the emitter $\varepsilon_{eff}(\lambda)$ is approximated by:

$$\varepsilon_{eff} = \frac{\varepsilon_e \tau_c}{1 - \rho_e \rho_c} \qquad \text{(Eq. 3.3)}$$

where τ_c is the transmittance of the cover, ρ_c is the reflectance of the cover, ρ_e is the reflectance of the emitter, ε_e is the emittance (1-ρ_e) of the emitter (wavelength-dependent notation is omitted for clarity).

$Q_{amb-rad}$ is given by:

$$Q_{amb-rad} = 2\pi \int_0^\infty \int_0^{\pi/2} \varepsilon_{amb}(\lambda,\theta)\, \varepsilon_{eff}(\lambda)\, I_b(T_{air},\lambda)\, cos\theta\, sin\theta\, d\theta\, d\lambda \qquad \text{(Eq. 3.4)}$$

The emissivity of the ambient (ε_{amb}) is determined assuming Kirchhoff's law where the angle-dependent emissivity is $\varepsilon_{amb}(\lambda) = 1 - \tau_{atm}(\lambda)^{1/cos\theta}$ and τ_{atm} is the atmospheric transmittance along the zenith direction, calculated using ModTran 5.[18]

The absorbed solar power considers the reflective properties of both the emitter and cover,[19] as given by:

$$Q_{sol} = \int_0^\infty \varepsilon_{eff}(\lambda)\, H_{AM1.5}(\lambda)\, cos\theta_s\, d\lambda \qquad \text{(Eq. 3.5)}$$

where $H_{AM1.5}(\lambda)$ is the AM1.5G spectral irradiance and θ_s is the time-dependent angle between the incident solar rays and the surface normal of the emitter. $H_{AM1.5}(\lambda)\, cos\theta_s$ is determined experimentally using the Vantage Pro2 weather station.[22]

The non-radiative heating term $Q_{amb-nrad}$ is given by:

$$Q_{amb-nrad} = h_{eff}(T_{air} - T_e) \qquad \text{(Eq. 3.6)}$$

where h_{eff} is the effective conductive and convective heat transfer coefficient between the emitting surface and the surrounding environment. h_{eff} of 9.5 W/m^{2}K was determined by fitting the model to experimental data at the peak solar irradiance (for both cases). T_{air} is the measured time-dependent rooftop air temperature.

3.6 Experimental Procedures

3.6.1 Fabrication of Polymer Films

PAN fibers were fabricated using a home-built electrospinning setup. PAN powder (*Polysciences, Inc.*) with an average MW of 200,000, was dissolved in dimethylformamide (*Sigma*) for 2.5, 5, 7, and 9 wt% concentrations and mixed at 40°C – 50°C overnight, or until the powder was fully dissolved. Below 2.5 wt%, the solution was not viscous enough to support fiber formation, while above 9 wt%, the solution was too viscous to be properly spun. The solution was loaded into a syringe with a 25-gauge blunt tip needle and placed in a syringe pump to ensure a constant flow rate. The PAN solution was electrospun at a flow rate of 0.4 mL/hr and stage height of 11.5 cm for 10, 20, 40, and 60 minutes for the 6 cm^2 samples. Voltage was adjusted for each concentration to ensure the formation of a Taylor cone. The substrates consisted of PE Glad® ClingWrap placed over aluminum for grounding. Post fabrication treatment included leaving the films to rest overnight and carefully placing a clean PE plastic wrap on top of the exposed PAN fibers as a protective layer. Surface density and film thickness for each of the nanoPAN shown above are reported in Tables 3.2 and 3.3.

The 5 wt% nanoPAN was scaled to 40 cm^2 for the outdoor experiments. The fibers were electrospun onto a layer of PE. All parameters were kept the same as for the 6 cm^2 samples except for the height and spin time. The height was adjusted to 14.8 cm to evenly distribute the fibers over the larger area and electrospinning was extended to 3 hours and 10 minutes to achieve a comparable thickness as before.

3.6.2 Optical Measurements and Microscopy

The optical properties of the film were measured using UV-Vis-NIR and FTIR spectrometers with integrating sphere attachments. Total reflectance was measured from 0.26 – 1.8 µm using a Shimadzu UV-3600 Plus UV-Vis. Total infrared transmittance and reflectance were measured from 2 – 20 µm using a Cary 670 benchtop FTIR. Linear interpolation was used between 1.7 µm and 2 µm when calculating SR. Optical measurements for all fabricated nanoPAN films are provided in Fig. 3.11 – 3.14. Fiber morphology was visualized using a TESCAN MIRA3 scanning electron microscope. Bead and fiber diameters were measured using TESCAN images and ImageJ software. A hundred measurements were taken for each 2.5, 5, 7, and 9 wt% nanoPAN films.
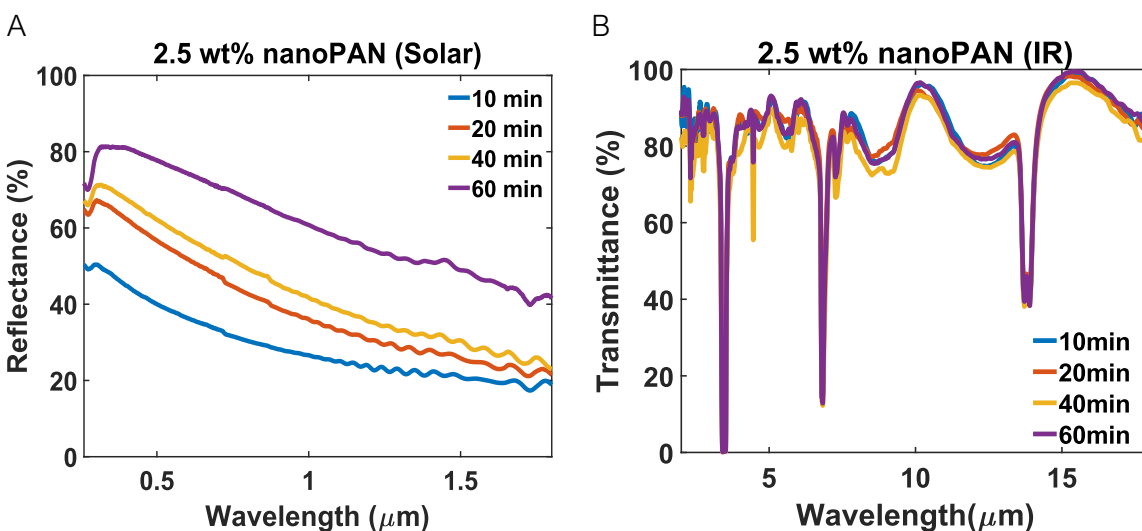
Figure 3.11. Measured (A) UV-Vis-NIR total reflectance and (B) FTIR total transmittance for the 2.5 wt% nanoPAN films varying electrospin time from 10 – 60 min.
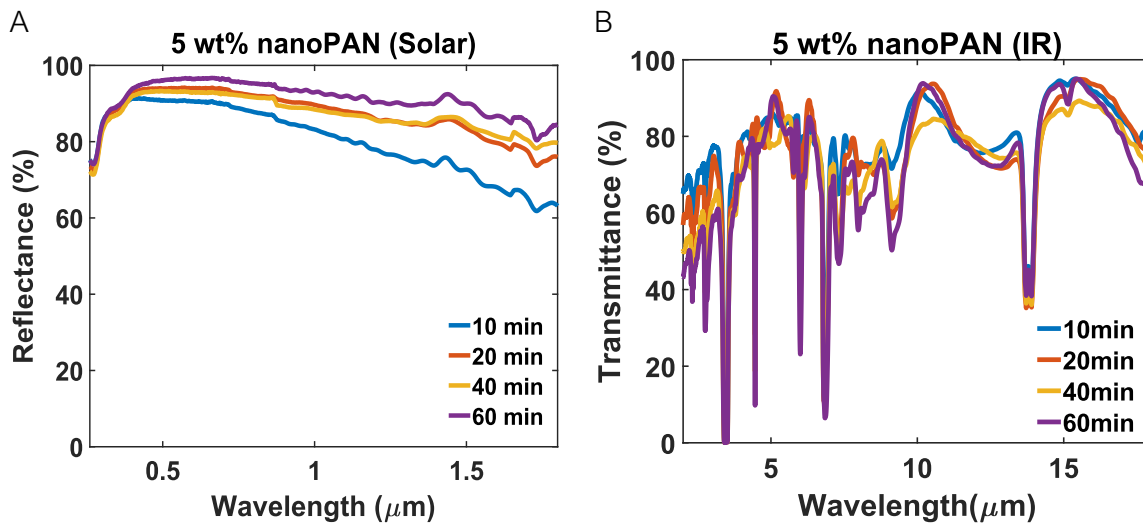
Figure 3.12. Measured (A) UV-Vis-NIR total reflectance and (B) FTIR total transmittance for the 5 wt% nanoPAN films varying electrospin time from 10 – 60 min.
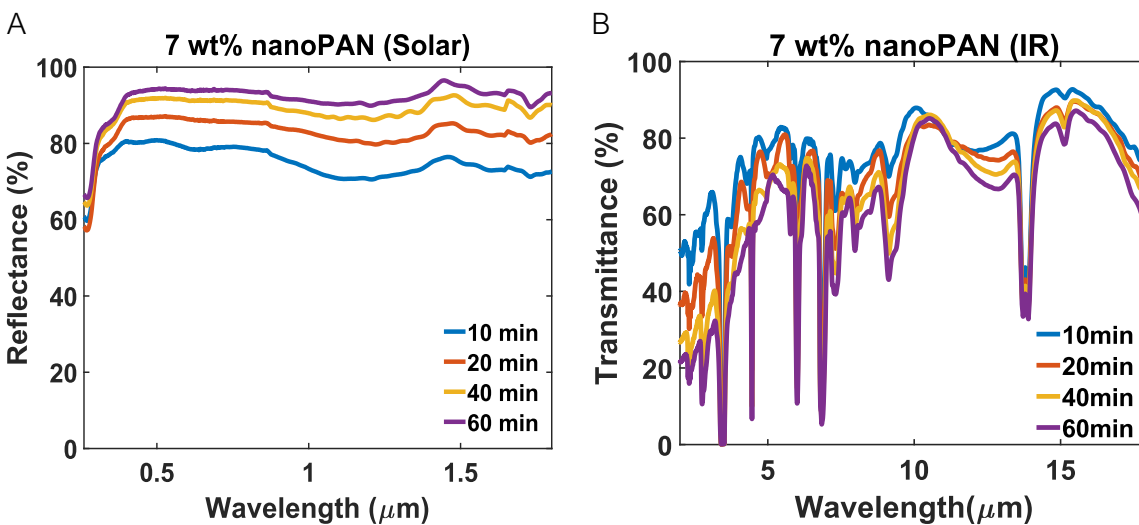
Figure 3.13. Measured (A) UV-Vis-NIR total reflectance and (B) FTIR total transmittance for the 7 wt% nanoPAN films varying electrospin time from 10 – 60 min.
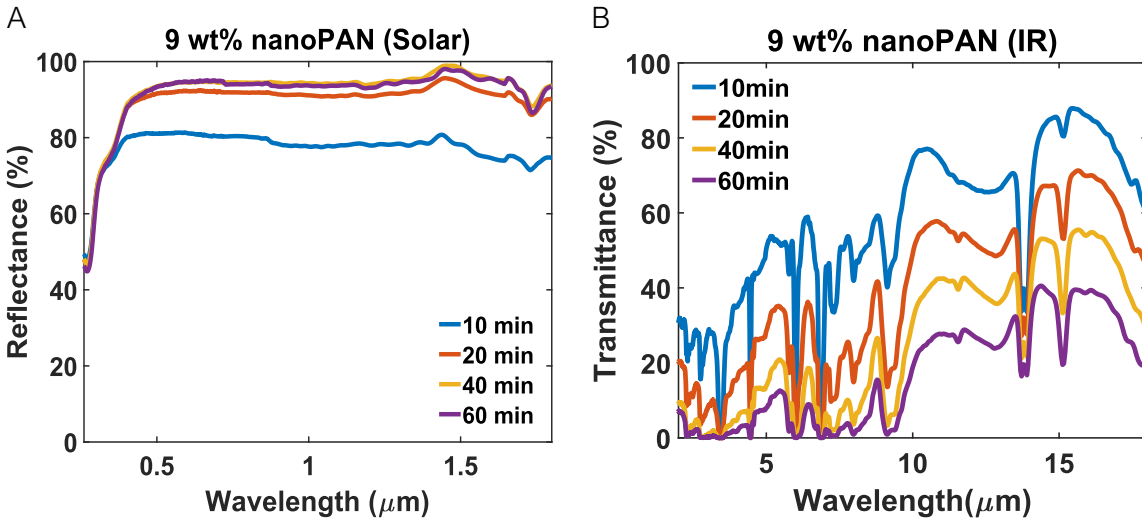
Figure 3.14. Measured (A) UV-Vis-NIR total reflectance and (B) FTIR total transmittance for the 9 wt% nanoPAN films varying electrospin time from 10 – 60 min.

3.6.3 SCUFF-EM Model

The scattering cross-sections of the cylindrical and beaded fiber morphologies were computed numerically with an open-source software implementation of the boundary-element method (BEM).[20,21] We completed mesh-refinement to ensure accurate results at smaller wavelengths. We verified the BEM by comparing our results to an analytical solution for Mie scattering via a PAN microsphere (see Fig. 3.15). Optical properties of PAN were taken from Tański *et al.*[23]

All 3D design and meshing were completed using GMSH, and an open-source finite element mesh generator.[24] The fiber meshes and material properties were then uploaded to SCUFF-EM to calculate the scattering cross-sections and efficiencies. For each simulation, a plane wave was normally incident upon the geometries in the z-direction. The wave was polarized in the x-direction with the following field amplitudes $(E_x, E_y, E_z) = (1, 0, 0)$. The MIE scattering suite of SCUFF-

EM calculates the total scattered power, $P_{scat.}$ by the fiber or bead. The scattering cross-section was determined by dividing the scattered power by the incident power flux, I.

$$\sigma_{scat.} = \frac{P_{scat.}}{I}$$

(Eq. 3.7)

The incident power flux is described by

$$I = \frac{|E_x|^2}{2Z_0}$$

(Eq. 3.8)

where Z_0 is the impedance of free space. This process was repeated for a y-polarized plane wave and the results were averaged. We averaged the x- and y-polarized results to represent normally mixed s- and p-polarized light. The scattering efficiency η was determined by normalizing the scattering cross-section by the geometric cross-section in the x-y plane.
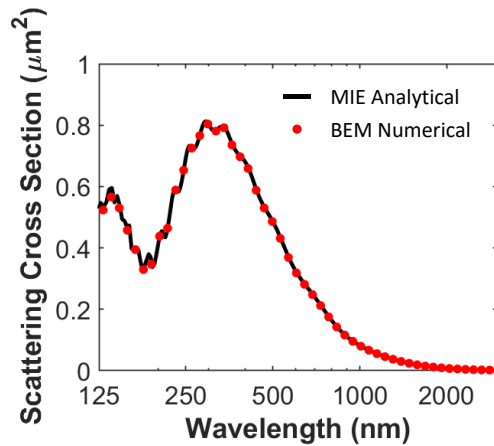
Figure 3.15. The accuracy of our EM simulations was tested by comparing the scattering cross-section of a PAN microsphere (D=750 nm) computed with SCUFF-EM[20,21] to the scattering cross-section computed by an analytical solution for Mie scattering. We completed a mesh refinement until the BEM results matched the analytical solution across the solar spectrum.

3.6.4 Outdoor Measurements

Outdoor tests were taken over four hours in Ann Arbor, Michigan on July 24. Minimal cloud coverage was observed during that time. A reference blackbody (BB) surface (Metal Velvet[TM] Acktar) was used as the emitter in both cases, *i.e.*, with and without nanoPAN. The emitter

temperature, ambient temperature, and humidity were logged as a function of time for the emitter samples. Emitter temperatures were measured using T-type thermocouples and an Extech SDL200 datalogger while transient ambient temperatures and humidity were logged using an OMEGA OM-24 logger. Solar irradiance daytime data[22] were obtained from a nearby Vantage Pro2 weather station (located approximately 1 km away). The emitters were placed in a foam enclosure to prevent bottom and side heating. The outside of the foam enclosure was wrapped with reflective mylar. A convective cover consisting of polyethylene (Glad® Cling Wrap) was placed taut over the aperture.

3.7 Conclusions

In summary, we present a systematic study investigating the role of polymer nanofiber morphology on radiative cooling properties. The additive dielectric resonances of the beaded nanofiber morphology result in favorable scattering across the solar spectrum. This decreases the amount of material needed to reach 95% total solar reflectance, allowing the film to retain good infrared transmittance (>70%). When tested under daytime outdoor conditions, nanoPAN reduces the stagnation temperature of a blackbody surface by as much as 50.8°C. The temperature reduction highlights the benefit of broadband reflectance offered by the hierarchy of the beaded nanofiber morphology. Furthermore, the approach presented here may enable the use of other materials or lower-purity feedstocks in radiative cooling covers.

3.8 References

(1)   Torgerson, E.; Hellhake, J. Polymer Solar Filter for Enabling Direct Daytime Radiative Cooling. *Sol. Energy Mater. Sol. Cells* **2020**, *206*, 110319. https://doi.org/10.1016/j.solmat.2019.110319.

(2)   Leroy, A.; Bhatia, B.; Kelsall, C. C.; Castillejo-Cuberos, A.; Di Capua, M. H.; Zhao, L.; Zhang, L.; Guzman, A. M.; Wang, E. N. High-Performance Subambient Radiative Cooling Enabled by Optically Selective and Thermally Insulating Polyethylene Aerogel. *Sci. Adv.* **2019**, *5* (eaat9480). https://doi.org/10.1126/sciadv.aat9480.

(3)   Mastai, Y.; Diamant, Y.; Aruna, S. T.; Zaban, A. TiO2 Nanocrystalline Pigmented Polyethylene Foils for Radiative Cooling Applications: Synthesis and Characterization. *Langmuir* **2001**, *17* (22), 7118–7123. https://doi.org/10.1021/la010370g.

(4)   Nilsson, T. M. J.; Niklasson, G. A.; Granqvist, C. G. A Solar Reflecting Material for Radiative Cooling Applications: ZnS Pigmented Polyethylene. *Sol. Energy Mater. Sol. Cells* **1992**, *28* (2), 175–193. https://doi.org/10.1016/0927-0248(92)90010-M.

(5)   Kim, H.; Lenert, A. Optical and Thermal Filtering Nanoporous Materials for Sub-Ambient Radiative Cooling. *J. Opt.* **2018**, *20* (084002). https://doi.org/https://doi.org/10.1088/2040-8986/aacaa1.

(6)   Incropera, F. P.; DeWitt, D. P.; Bergman, T. L.; Lavine, A. S. *Fundamentals of Heat and Mass Transfer(6th Edition)*; 2007. https://doi.org/10.1016/j.applthermaleng.2011.03.022.

(7)   Nilsson, N. A.; Eriksson, T. S.; Granqvist, C. G. Infrared-Transparent Convection Shields for Radiative Cooling: Initial Results on Corrugated Polyethylene Foils. *Sol. Energy Mater.* **1985**, *12* (5), 327–333. https://doi.org/10.1016/0165-1633(85)90002-4.

(8)   Chen, Z.; Zhu, L.; Raman, A.; Fan, S. Radiative Cooling to Deep Sub-Freezing Temperatures through a 24-h Day-Night Cycle. *Nat. Commun.* **2016**, *7*, 1–5. https://doi.org/10.1038/ncomms13729.

(9)   Chalmers, J. M. Infrared Spectroscopy in Analysis of Polymers and Rubbers. In *Encyclopedia of Analytical Chemistry*; Wiley, 2000. https://doi.org/10.1002/9780470027318.a2015.

(10)   Chen, J.; Lu, L. Development of Radiative Cooling and Its Integration with Buildings: A Comprehensive Review. *Sol. Energy* **2020**, *212* (November), 125–151. https://doi.org/10.1016/j.solener.2020.10.013.

(11)   Uyar, T.; Besenbacher, F. Electrospinning of Uniform Polystyrene Fibers: The Effect of Solvent Conductivity. *Polymer (Guildf).* **2008**, *49* (24), 5336–5343. https://doi.org/10.1016/j.polymer.2008.09.025.

(12)   Li, Z.; Wang, C. *Effects of Working Parameters on Electrospinning. In: One-Dimensional Nanostructures*; Springer, Berlin, Heidelberg, 2013. https://doi.org/10.1007/978-3-642-36427-3.

(13)   Fong, H.; Chun, I.; Reneker, D. H. Beaded Nanofibers Formed during Electrospinning. *Polymer (Guildf).* **1999**, *40* (16), 4585–4592. https://doi.org/10.1016/S0032-3861(99)00068-3.

(14)   Yang, Z.; Peng, H.; Wang, W.; Liu, T. Bead-to-Fiber Transition in Electrospun Polystyrene. *J. Appl. Polym. Sci.* **2010**, *116* (5), 2658–2667. https://doi.org/10.1002/app.

(15)   Lee, K. H.; Kim, H. Y.; Bang, H. J.; Jung, Y. H.; Lee, S. G. The Change of Bead Morphology Formed on Electrospun Polystyrene Fibers. *Polymer (Guildf).* **2003**, *44* (14), 4029–4034. https://doi.org/10.1016/S0032-3861(03)00345-8.

(16)   Deitzel, J. M.; Kleinmeyer, J.; Harris, D.; Beck Tan, N. C. The Effect of Processing Variables on the Morphology of Electrospun Nanofibers and Textiles. *Polymer (Guildf).* **2001**, *42*, 261–272. https://doi.org/https://doi.org/10.1016/S0032-3861(00)00250-0.

(17)   Kuznetsov, A. I.; Miroshnichenko, A. E.; Brongersma, M. L.; Kivshar, Y. S.; Luk'yanchuk, B. Optically Resonant Dielectric Nanostructures. *Science (80-.).* **2016**, *354* (6314). https://doi.org/10.1126/science.aag2472.

(18)   Berk, A.; Anderson, G. P.; Acharya, P. K.; Bernstein, L. S.; Muratov, L.; Lee, J.; Fox, M.; Adler-Golden, S. M.; Chetwynd, Jr., J. H.; Hoke, M. L.; Lockwood, R. B.; Gardner, J. A.; Cooley, T. W.; Borel, C. C.; Lewis, P. E.; Shettle, E. P. ModTran 5: 2006 Update. In *Proc SPIE Int Soc Opt Eng*; 2006; Vol. 6233, pp 62331F-62331F – 8. https://doi.org/10.1117/12.665077.

(19)   ASTM. Reference Solar Spectral Irradiance: Air Mass 1.5.

(20)   Reid, M. T. H.; Johnson, S. G. Efficient Computation of Power, Force, and Torque in BEM Scattering Calculations. *IEEE Trans. Antennas Propag.* **2015**, *63* (8), 3588–3598. https://doi.org/10.1109/TAP.2015.2438393.

(21)   Reid, M. T. H.; Johnson. Efficient Computation of Power, Force, and Torque in BEM Scattering Calculations. 2013.

(22)   Weather Underground https://www.wunderground.com/dashboard/pws/KMIANNAR164/graph/2020-07-24/2020-07-24/daily.

(23)   Tański, T.; Matysiak, W.; Hajduk, B. Manufacturing and Investigation of Physical Properties of Polyacrylonitrile Nanofibre Composites with SiO2, TiO2 and Bi2O3 Nanoparticles. *Beilstein J. Nanotechnol.* **2016**, *7* (1), 1141–1155. https://doi.org/10.3762/bjnano.7.106.

(24)   Geuzaine, C.; Remacle, J. Gmsh: A 3-D Finite Element Mesh Generator with Built-in Pre- and Post-Processing Facilities. *Int. J. Numer. Methods Eng.* **2009**, *79* (11), 1309–1331. https://doi.org/10.1002/nme.

Chapter 4: Near Ideal Solar Reflectance Using Electrospun Nanofibers for Passive Radiative Cooling

4.1 Motivation

Various approaches such as photonic and specular reflectors,[1–5] scattering particles,[6–12] and morphological control[13–19] have been deployed as ways to achieve high solar reflectance. On average, solar heating (~1000 W/m^2) can impart 10 times more heat than can be rejected by state-of-the-art radiative cooling technologies (~100 W/m^2). Therefore, an increase in 1% reflectance can lead to a net gain of 10 W/m^2 in cooling power.[20,21] Despite the diverse range of materials and designs, most report solar weighted reflectances (SR) in the range of 95 – 97%.[22] As such, a daytime outdoor measurement with an emitter that achieves near 100% SR has yet to be demonstrated. A specular reflecting emitter can be used to reflect sunlight, but the glare from these mirrored surfaces can cause visual impairments and is undesired in public areas. Therefore, materials with diffuse appearances are favorable for outdoor applications.

Recently, electrospinning has gained interest as a way to fabricate nanofibers with hierarchical morphologies to achieve broad reflectance across the solar spectrum.[8,14,15] Though other methods such as phase separation followed by critical point drying,[17] phase-inversion,[13,18] and sacrificial particle templating,[16] achieve solar scattering through a porous system, the lack of morphological control causes scattering to occur beyond the solar spectrum. On the other hand, electrospinning

can be used to control both the morphology and polydispersity by varying the polymer solution to enable size distributions relevant to scatter solar radiation.[14,15]

In this study, we fabricate emitters with 99(+/-0.5)% SR emitters and compare their cooling performance to the current state-of-the-art specular reflective emitters which are schematically shown in Fig. 4.1a,b. Polyacrylonitrile nanofibers (nanoPAN) are electrospun directly on a PDMS coated silver mirror to retain the high solar reflectance and visually convert the emitter from specular to diffuse appearance (*i.e.*, mirrored to opaque white) (Fig. 4.1c,d). The PDMS serves as the primary emitting layer while the silver and nanoPAN are responsible for blocking solar radiation. The nanoPAN fibers enhance reflectance in the UV and near IR regions which results in a total solar-weighted reflectance of 99%. The cooling performance of both a PDMS coated silver emitter and emitter with nanoPAN were tested outdoors in March under clear sky conditions in Ann Arbor, MI. An enhancement of ~5°C and ~30 W/m^2 for the stagnation temperature and cooling power during peak solar irradiance is observed with nanoPAN compared to the control. The results shown here demonstrate the effectiveness of nanoPAN to enhance the total solar reflectance to achieve near ideal SR and nighttime-like cooling performance during the day.
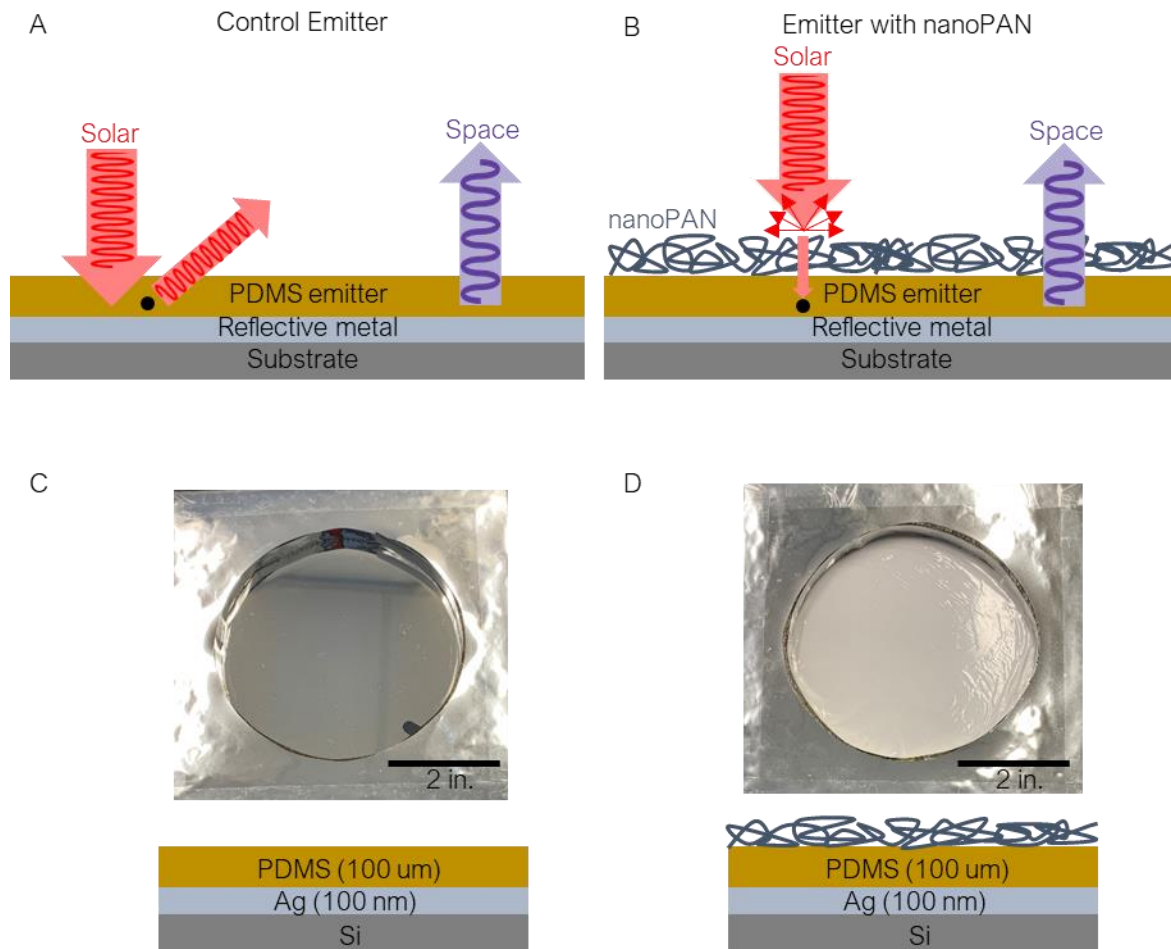
Figure 4.1. (A) Schematic of control specular reflective emitter. (B) Schematic of specular emitter paired with diffusely reflective nanoPAN fibers. (C) and (D) show images of mirrored and opaquely scattering surface of the emitters.

4.2 Optimizing Morphology and Polydispersity of PAN Nanofibers

In chapter 3, we demonstrated that nanoPAN morphology affects the scattering cross-section in solar regions by varying the polymer concentration.[15] When paired with a blackbody emitter, the nanoPAN cover provided a 95% SR that resulted in a 50°C temperature decrease from the blackbody control.[15] A similar technique was used in this work to optimize the emitter's solar scattering properties. A 6wt% PAN solution was used to fabricate beaded nanoPAN fibers via electrospinning after experimentally optimizing for high solar reflectance. Fig. 4.2a,b shows the size distribution of the beads and fibers measured using SEM images. The desired broad scattering

across the solar spectrum is a result of the hierarchical morphology of the nanofibers. The cylinders interconnecting the beads primarily scatter shorter wavelengths and the beads scatter longer wavelengths due to their respective characteristic length scales.[14,15]
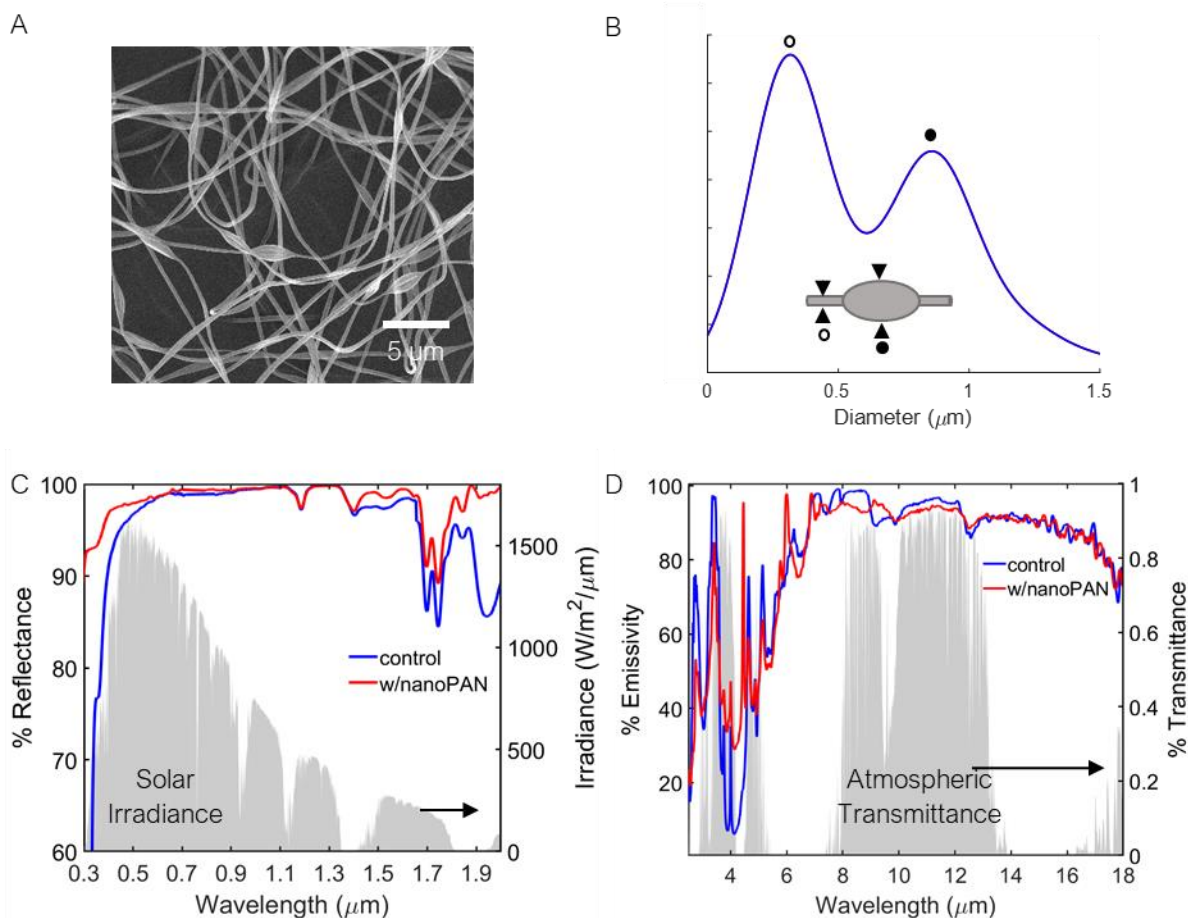
Figure 4.2. (A) SEM image of 6 wt% electrospun nanoPAN fibers. (B) Hierarchical size distribution of the interconnecting cylinder and beaded morphologies. (C) Measured total reflectance using UV-Vis of the control and emitter with nanoPAN. The AM1.5 G solar spectrum is shown for reference. (D) Measured total emissivity using FTIR for the control and emitter with nanoPAN. The atmospheric transmittance is shown for reference.[23]

Both the morphology and porous nature of the nanoPAN fibers diffusely reflect incoming solar radiation, giving the films an opaque white appearance. In this study, a PDMS coated silver mirror (here-on referred to as "control") acts as the base reflector for our emitter. The control alone has a SR of 97%, however, there is a sharp drop in reflectance at the solar irradiance peak starting around

0.5 μm, which is near the plasma frequency of sliver (Fig. 4.2c). The addition of nanoPAN increases the total SR by 2% by closing the gaps where silver is less reflective. Though this improvement may seem trivial, a 2% improvement in SR translates to ~20% improvement in cooling power at ambient temperatures for ideal conditions.

The measured total reflectance in Fig. 4.2c shows an increase in solar scattering with nanoPAN for wavelengths below 0.5 μm and above 1.4 μm, which is a result of the beaded hierarchical morphology. Specifically, increases in SR below 0.5 μm can significantly reduce solar absorption because the peak solar irradiance occurs around 0.5 μm (Fig. 4.2c). The atmospheric weighted emissivity (ε) decreases from 83% to 80% which is largely due to increased reflectance from the fibers (see Fig. 4.3), however, the benefit of increasing the SR outweighs the drop in ε.
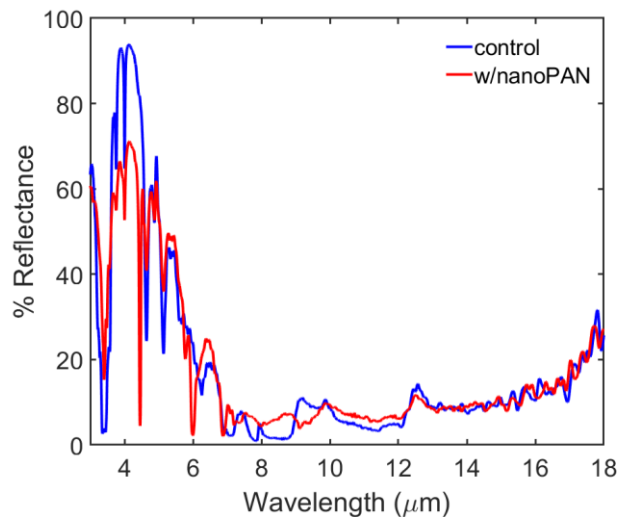
Figure 4.3 Measured total reflectance using FTIR for the control and emitter with nanoPAN.

4.3 Measuring Stagnation Temperature

The outdoor tests were conducted in Ann Arbor, MI under clear sky conditions in March. A transparent polyethylene convective cover was used to shield the emitters from the wind. The

global horizontal irradiance, as well as the on-site ambient temperature, were recorded along with the emitter temperatures. The temperature of three configurations (Fig. 4.4a,b) was measured: PDMS coated Ag mirror (control), insulated nanoPAN (w/nanoPAN), and heated nanoPAN (used to measure cooling power).

The change in emitter temperature relative to the measured ambient is shown in Fig. 4.4c ($\Delta T = T_{amb.} - T_{emit}$). During the daytime, the control stays near ambient and inversely tracks the solar irradiance while the emitter with nanoPAN consistently remains below ambient temperatures. Though the emitter with nanoPAN also follows the irradiance trend, the temperature variations are less pronounced than the control, especially when transitioning from day to nighttime. The ΔT transition from day to night for the control was ~9°C while the nanoPAN transition was ~4°C. If an emitter could reach 100% SR, we would expect to mimic nighttime conditions with minimal differences in cooling performance between the day and nighttime. Overall, our results demonstrate temperature reductions beyond the 97% SR emitter and with fewer differences between the day and nighttime. Depending on the desired application, even lower stagnation temperatures can be reached by tailoring the infrared region to selectively emit in the atmospheric windows. This can be achieved by replacing the PDMS with a selective emitter (*e.g.*, photonic structure), or modifying the nanoPAN by incorporating particles with selectivity in the atmospheric bands, as discussed in Chapter 2.
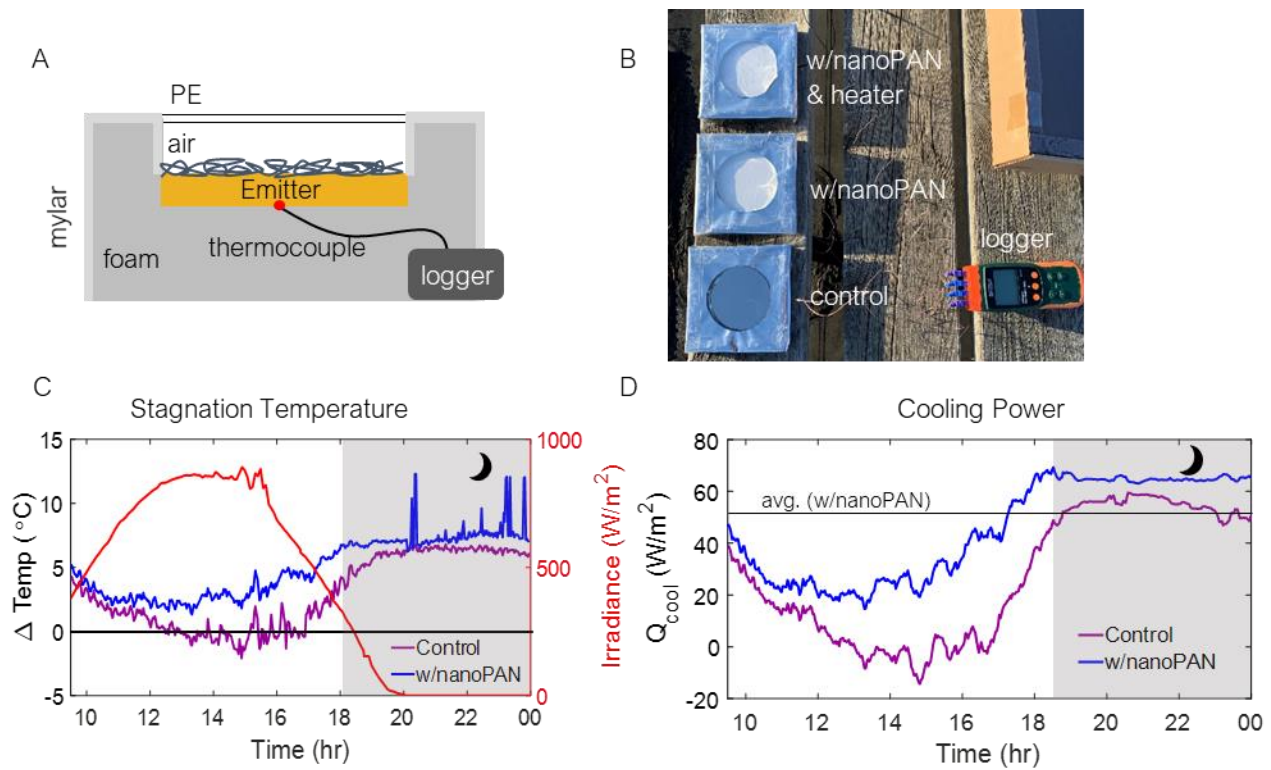
Figure 4.4. Schematic of (A) stagnation temperature and (B) outdoor setup. (C) Temperature reduction of control and emitter with nanoPAN relative to the ambient temperature during the day. (D) Corresponding cooling power at ambient temperature of emitter with nanoPAN. We applied a 10-minute moving average to the measured ambient temperature to decrease noise from local variations such as wind.

4.4 Measuring Cooling Power

The cooling power at ambient temperature was found using the measured stagnation temperatures. The setup was kept identical to the stagnation temperature measurement except a heater was attached to the emitter with nanoPAN, as seen in Fig 4.5. The cooling power of the control was not directly measured due to equipment constraints; however, we know from the stagnation temperature measurements the cooling power at high noon is near 0 because it is close to the ambient temperature. Constant power is supplied to the heater and the resulting temperature is measured. This temperature along with the stagnation temperature is used to calculate the heat transfer coefficient (*i.e.*, the slope of the cooling power curve), which is then used to find the

cooling power at ambient temperatures throughout the day (refer to experimental procedures for details).

A

B
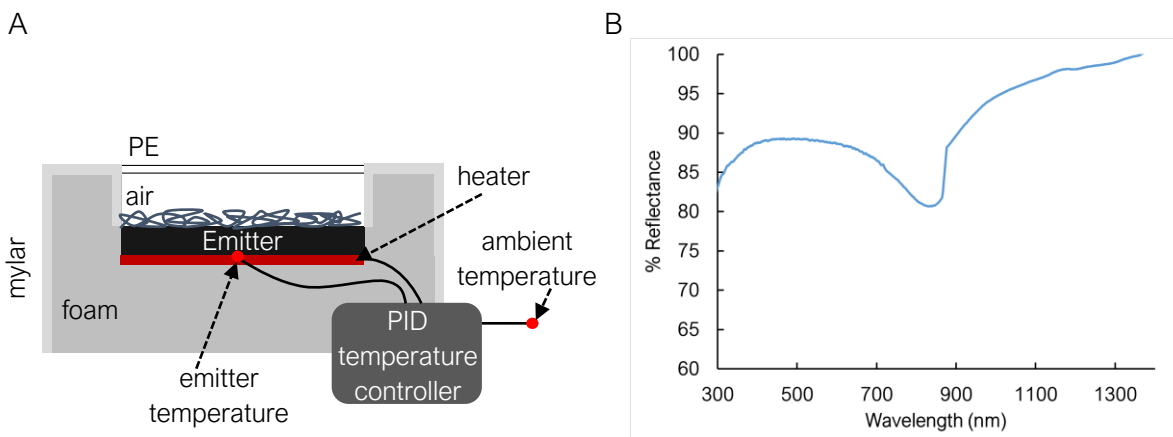
Figure 4.5 (A) Schematic of outdoor setup used to measure cooling power and (B) reflectance of mylar used to coat the foam enclosure.

The average cooling power of the emitter with nanoPAN over 14 hours was 48.2 W/m^2 (Fig. 4.4d). Our values are comparable to recently reported measured cooling powers, however, direct comparisons of performance metrics should be cautioned due to variations in outdoor conditions.[11,13] The measured cooling power shows that a ~1°C sub-ambient temperature reduction results in a ~6 W/m^2 cooling that is dependent on the effective heat transfer coefficient, which is less than the expected theoretical 10 W/m^2. The differences can be attributed to outdoor conditions, which cannot be controlled. Parasitic heating of the enclosure is also likely since the mylar is only ~95% reflective in the solar region (Fig. 4.5b).

Although the SR with nanoPAN is 99%, the reflectance near 0.45 μm and below trails off from 97%. Optimizing the size distribution of scatterers near the solar irradiance peak can further mitigate the solar heating of the emitter. This can be achieved by adding a layer of nanoPAN with

smaller characteristic length scales that will primarily act to scatter wavelengths below 500 nm. For example, 5 wt% nanoPAN can be electrospun on top of the existing 6 wt% nanoPAN to increase reflectance at shorter wavelengths while maintaining broad reflectance across the solar spectrum.

4.5 Experimental Procedures

4.5.1 Fabrication of Emitters

The control emitter was fabricated using electron beam deposition by depositing 10 nm of titanium (used as an adhesion layer) and 150 nm of silver on top of a 4 in. silicon wafer. 150 μm of polydimethylsiloxane (Dow SYLGARD^{TM} 184) was added via spinning coating on top of the silver and cured for 15 minutes at 150°C. The emitters with nanoPAN consisted of identical layers as the control with additional 530 μm of nanoPAN on top of the PDMS.

The polymer solution used for electrospinning was prepared by dissolving 6wt% of PAN powder (Polyscience, Inc.) in DMF (Sigma) at 40 – 50°C with stirring overnight or until fully dissolved. A 25-gauge blunt tip needle was used, and the PAN solution was electrospun for 5 hours at a constant flow rate of 0.4 mL/h at a stage height of 19 cm. To increase the electric field of the substrate, the PDMS was treated using a plasma cleaner (Harrick Plasma PDC-001) with air for 2 minutes before electrospinning.

4.5.2 Optical Characterization

The total reflectance in the solar region for each emitter was measured using a Shimadzu UV-3600 UV-vis-NIR with an integrating sphere attachment and PTFE reference. The total emissivity was

measured using a ThermoFisher Nicolet iS50 FTIR spectrometer also with an integrating sphere accessory. The size distribution and fiber morphology were visualized using a TESCAN MIRA3 scanning electron microscope. ImageJ software was used to measure the diameter of one hundred beads and fiber each to determine the polydispersity.

4.5.3 Outdoor Stagnation Temperature Measurements

Outdoor measurements were taken in Ann Arbor, MI on March 29, 2021, on a clear sky day. T-Type thermocouples attached to the back of each emitter were used to measure the stagnation temperature using an Extech SDL200 Datalogger. The emitters were placed in an insulating foam enclosure coated with reflective mylar to prevent bottom and side heating. A thin layer of PE (Glad Cling Wrap) was placed over the emitter with an airgap separation as a convective cover. The global horizontal solar irradiance was collected from a Vantage Pro2 weather station (located approximately 1 km away) while the transient ambient temperature was measured using a shaded T-Type thermocouple.

4.5.4 Outdoor Cooling Power Measurements

The setup used for cooling power measurements was identical to the stagnation temperature measurements with the addition of a 4-inch round heater that was placed at the bottom of an emitter with nanoPAN. This measurement was also taken at the same time and location as the stagnation temperature measurements. An external power source was used to supply a constant 85 W/m^2 to the heater (12 V with a heater resistance of 210 Ω). The temperature of the emitter with constant heating was measured using a T-type thermocouple with the same Extech SDL200 Datalogger. The stagnation temperature and heated sample were used to find the heat transfer coefficient (*i.e.*,

cooling power curve slope) for each data point in time. The heat transfer coefficient was then used to calculate the corresponding cooling power at each measured ambient temperature using the energy balance equations (refer to Eqs. 3.1 – 3.6).

4.6 Conclusions

We demonstrate the cooling performance potential of the most reflective emitter to date, a 99% SR emitter that combines diffuse reflectance with a mirrored surface. The top layer is comprised of scattering nanoPAN fibers that increase reflectance below 0.5 μm and above 1.4 μm compared to the mirrored Ag control (97% SR). The broad reflectance is a result of scattering from the hierarchical morphology of nanoPAN that is comprised of both thin fibers and larger beads.

Day and nighttime outdoor measurements show that the emitter with nanoPAN consistently achieves lower temperatures than the control while also providing sub-ambient cooling and average cooling power enhancements of 30 W/m^2 during peak solar irradiance. Though the 99% SR outperforms the current state-of-the-art 97% SR, additional improvements can be made by adding scatterers that further increase the reflectance around the solar peak of 450 nm. In addition, our work provides a basis for selectively increasing the reflectance of existing emitters by tailoring the size parameter of electrospun nanoPAN fibers.

4.7 References

(1)   Raman, A. P.; Anoma, M. A.; Zhu, L.; Rephaeli, E.; Fan, S. Passive Radiative Cooling below Ambient Air Temperature under Direct Sunlight. *Nature* **2014**, *515* (7528), 540–544. https://doi.org/10.1038/nature13883.

(2)   Chen, Z.; Zhu, L.; Raman, A.; Fan, S. Radiative Cooling to Deep Sub-Freezing Temperatures through a 24-h Day-Night Cycle. *Nat. Commun.* **2016**, *7*, 1–5. https://doi.org/10.1038/ncomms13729.

(3)   Rephaeli, E.; Raman, A.; Fan, S. Ultrabroadband Photonic Structures to Achieve High-Performance Daytime Radiative Cooling. *Nano Lett.* **2013**, *13* (4), 1457–1461. https://doi.org/10.1021/nl4004283.

(4)   Wu, D.; Liu, C.; Xu, Z.; Liu, Y.; Yu, Z.; Yu, L.; Chen, L.; Li, R.; Ma, R.; Ye, H. The Design of Ultra-Broadband Selective near-Perfect Absorber Based on Photonic Structures to Achieve near-Ideal Daytime Radiative Cooling. *Mater. Des.* **2018**, *139*, 104–111. https://doi.org/10.1016/j.matdes.2017.10.077.

(5)   Kou, J. long; Jurado, Z.; Chen, Z.; Fan, S.; Minnich, A. J. Daytime Radiative Cooling Using Near-Black Infrared Emitters. *ACS Photonics* **2017**, *4* (3), 626–630. https://doi.org/10.1021/acsphotonics.6b00991.

(6)   Zhai, Y.; Ma, Y.; David, S. N.; Zhao, D.; Lou, R.; Tan, G.; Yang, R.; Yin, X. Scalable-Manufactured Randomized Glass-Polymer Hybrid Metamaterial for Daytime Radiative Cooling. *Science (80-.).* **2017**, *355* (6329), 1062–1066. https://doi.org/10.1126/science.aai7899.

(7)   Atiganyanun, S.; Plumley, J.; Han, S. J.; Hsu, K.; Cytrynbaum, J.; Peng, T. L.; Han, S. M.; Han, S. E. Effective Radiative Cooling by Paint-Format Microsphere-Based Photonic Random Media. *ACS Photonics* **2018**, *5* (4), 1181–1187. https://doi.org/10.1021/acsphotonics.7b01492.

(8)   Wang, X.; Liu, X.; Li, Z.; Zhang, H.; Yang, Z.; Zhou, H.; Fan, T. Scalable Flexible Hybrid Membranes with Photonic Structures for Daytime Radiative Cooling. *Adv. Funct. Mater.* **2020**, *30* (5), 1–9. https://doi.org/10.1002/adfm.201907562.

(9)   Yang, J.; Gao, X.; Wu, Y.; Zhang, T.; Zeng, H.; Li, X. Nanoporous Silica Microspheres–Ploymethylpentene (TPX) Hybrid Films toward Effective Daytime Radiative Cooling. *Sol. Energy Mater. Sol. Cells* **2019**, No. 1295, 110301. https://doi.org/10.1016/j.solmat.2019.110301.

(10)   Bao, H.; Yan, C.; Wang, B.; Fang, X.; Zhao, C. Y.; Ruan, X. Double-Layer Nanoparticle-Based Coatings for Efficient Terrestrial Radiative Cooling. *Sol. Energy Mater. Sol. Cells* **2017**, *168* (November 2016), 78–84. https://doi.org/10.1016/j.solmat.2017.04.020.

(11)   Li, X.; Peoples, J.; Huang, Z.; Zhao, Z.; Qiu, J.; Ruan, X. Full Daytime Sub-Ambient Radiative Cooling in Commercial-like Paints with High Figure of Merit. *Cell Reports Phys. Sci.* **2020**, *1* (10), 100221. https://doi.org/10.2139/ssrn.3652325.

(12)   Alden, J. D.; Atiganyanun, S.; Vanderburg, R.; Lee, S. H.; Plumley, J. B.; Abudayyeh, O. K.; Han, S. M.; Han, S. E. Radiative Cooling by Silicone-Based Coating with Randomly Distributed Microbubble Inclusions. *J. Photonics Energy* **2019**, *9* (03), 1. https://doi.org/10.1117/1.jpe.9.032705.

(13)   Zhang, J.; Zhou, Z.; Tang, H.; Xing, J.; Quan, J.; Liu, J.; Yu, J.; Hu, M. Mechanically Robust and Spectrally Selective Convection Shield for Daytime Subambient Radiative Cooling. **2021**. https://doi.org/10.1021/acsami.0c21204.

(14)   Li, D.; Liu, X.; Li, W.; Lin, Z.; Zhu, B.; Li, Z.; Li, J.; Li, B.; Fan, S.; Xie, J.; Zhu, J. Scalable and Hierarchically Designed Polymer Film as a Selective Thermal Emitter for High-Performance All-Day Radiative Cooling. *Nat. Nanotechnol.* **2020**. https://doi.org/10.1038/s41565-020-00800-4.

(15)   Kim, H.; McSherry, S.; Brown, B.; Lenert, A. Selectively Enhancing Solar Scattering for Direct Radiative Cooling through Control of Polymer Nanofiber Morphology. *ACS Appl. Mater. Interfaces* **2020**, *12* (39), 43553–43559. https://doi.org/10.1021/acsami.0c09374.

(16)   Torgerson, E.; Hellhake, J. Polymer Solar Filter for Enabling Direct Daytime Radiative Cooling. *Sol. Energy Mater. Sol. Cells* **2020**, *206*, 110319. https://doi.org/10.1016/j.solmat.2019.110319.

(17)   Leroy, A.; Bhatia, B.; Kelsall, C. C.; Castillejo-Cuberos, A.; Di Capua, M. H.; Zhao, L.; Zhang, L.; Guzman, A. M.; Wang, E. N. High-Performance Subambient Radiative Cooling Enabled by Optically Selective and Thermally Insulating Polyethylene Aerogel. *Sci. Adv.* **2019**, *5* (eaat9480). https://doi.org/10.1126/sciadv.aat9480.

(18)   Mandal, J.; Fu, Y.; Overvig, A.; Jia, M.; Sun, K.; Shi, N.; Zhou, H.; Xiao, X.; Yu, N.; Yang, Y. Hierarchically Porous Polymer Coatings for Highly Efficient Passive Daytime Radiative Cooling. *Science (80-.).* **2018**, *362* (6412), 315–319. https://doi.org/10.1126/science.aat9513.

(19)   Kim, H.; Lenert, A. Optical and Thermal Filtering Nanoporous Materials for Sub-Ambient Radiative Cooling. *J. Opt.* **2018**, *20* (084002). https://doi.org/https://doi.org/10.1088/2040-8986/aacaa1.

(20)   Zhao, D.; Aili, A.; Zhai, Y.; Xu, S.; Tan, G.; Yin, X.; Yang, R. Radiative Sky Cooling: Fundamental Principles, Materials, and Applications. *Appl. Phys. Rev.* **2019**, *6* (2), 021306. https://doi.org/10.1063/1.5087281.

(21)   Hossain, M. M.; Gu, M. Radiative Cooling: Principles, Progress, and Potentials. *Adv. Sci.* **2016**, *3* (7), 1–10. https://doi.org/10.1002/advs.201500360.

(22)   Chen, J.; Lu, L. Development of Radiative Cooling and Its Integration with Buildings: A Comprehensive Review. *Sol. Energy* **2020**, *212* (November), 125–151. https://doi.org/10.1016/j.solener.2020.10.013.

(23)   Berk, A.; Anderson, G. P.; Acharya, P. K.; Bernstein, L. S.; Muratov, L.; Lee, J.; Fox, M.; Adler-Golden, S. M.; Chetwynd, Jr., J. H.; Hoke, M. L.; Lockwood, R. B.; Gardner, J. A.; Cooley, T. W.; Borel, C. C.; Lewis, P. E.; Shettle, E. P. ModTran 5: 2006 Update. In *Proc SPIE Int Soc Opt Eng*; 2006; Vol. 6233, pp 62331F-62331F – 8. https://doi.org/10.1117/12.665077.

Chapter 5: Future Directions for Passive Radiative Cooling

5.1 Comprehensive Study of Thermal Conductivity

A theoretical approach to understanding the effects of thermal conductivity on passive radiative cooling performance was presented in chapter 2. Both the optical properties and thermal conductivity needs to be considered when using a thermally insulating IR transparent layer for radiative cooling.[1] The porous nature of our nanoPAN films shows potential for providing thermal resistance in the IR in addition to scattering solar radiation via the smaller characteristic length scales of the beaded morphology.[2] Pairing a low thermal conductivity cover with an emitter would increase the potential of reaching even lower stagnation temperatures compared to an emitter with minimal insulation.[3]

Increasing thickness can help increase thermal resistance, however, since attenuation in the IR is approximated by the Beer-Lambert law ($exp\,(-\beta L)$), there is a trade-off between improving thermal properties and maintaining IR transparency. Modeling can be used to estimate the insulating layer thickness, however, the random structure and unique beaded morphology of nanoPAN can be computationally expensive to model with precision. As such, a systematic study that measures both the thermal resistance and IR transparency as a function of film thickness is recommended.

Infrared transmittance can be measured using an FTIR spectrometer, similar to experiments proposed in chapters 3 and 4. The film should enable sufficient transparency in the atmospheric windows when considering the optical properties. The thermal resistance (*i.e.*, thermal conductivity) of nanoPAN can be measured using a variable temperature hot stage and heat flux sensor as illustrated in Fig. 5.1a. Preliminary results in Fig. 5.1b show that the thermal conductivity of 5wt% nanoPAN is similar to commercial foams, however, there are large errors associated with these measurements. Recommendations for future work include improving or developing a reliable method to measure the thermal resistance of fibrous nanoPAN films. Given these results, the thermal and optical properties can be implemented into the radiative cooling energy balance (Eq. 2.1) to optimize the nanoPAN features for cooling performance.
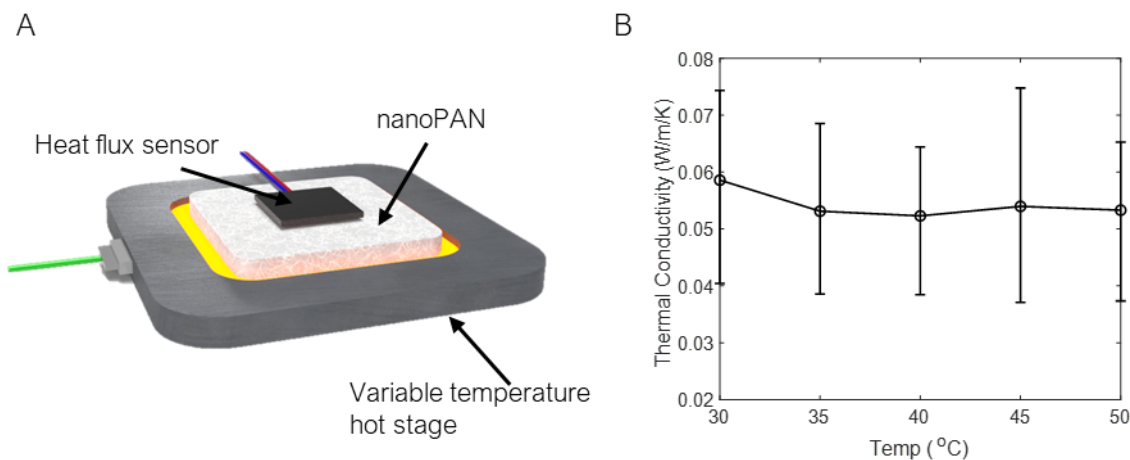
Figure 5.1 (A) Schematic of proposed thermal resistance measurements for nanoPAN films. (B) Preliminary thermal conductivity results measured using the setup shown in (A).

5.2 Incorporating Scattering Particles to Enhance Solar Reflectance

In addition to morphological control achieved by electrospinning PAN, scattering particles can be used to further enhance the solar reflectance of nanofibrous covers. If solar reflectance can be increased or retained by incorporating them into a fibrous polymer matrix, then less polymer

material would be needed. The intrinsic optical properties, size, and interactions with the polymer are all criteria to consider when choosing a scattering particle.

A material with a high refractive index mismatch to the polymer and a particle size distribution that scatters broadly in the solar region should be chosen to enhance reflectance. If the purpose of the polymer film is to act as a convective cover, then both the polymer and particles should have low absorption in the infrared (imaginary part of the refractive index) to enable transmission to outer space. If, however, the role of the film is to emit in the IR (*i.e.*, part of the overall emitter), then constraints of retaining high IR transmittance do not apply. In either case, the bulk of solar scattering will occur from the particles rather than the polymer fibers, therefore, less material would be required to reach the same SR and precise morphological control of the fibers would not be necessary.

When incorporating scattering particles into the polymer matrix, the surface chemistry of the nanoparticles should also be considered. Currently, there is a limited understanding of how surface treating scattering particles can affect the way they are distributed into fibers via electrospinning, and in turn, affect the optical properties. As illustrated in Fig. 5.2, the particles could decorate the surface of the fibers, be embedded within the fiber, form aggregates, or form any of the mentioned combinations. Understanding particle-polymer chemistry can widen the scope and design of materials for use in radiative cooling covers.
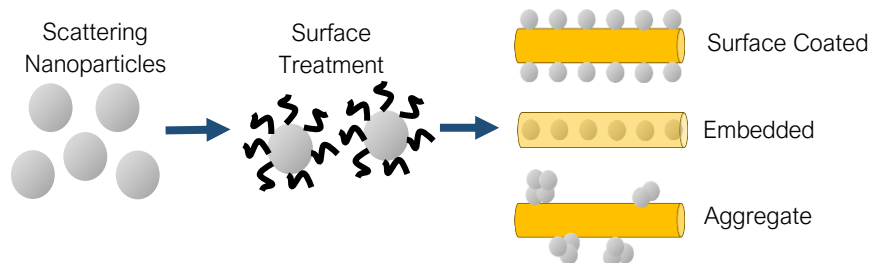
Figure 5.2. Schematic illustrating the possible ways nanoparticles may incorporate into a fibrous matrix.

## 5.3 Use of Recycled and Biodegradable Polymers for Radiative Cooling

Previous to the work presented in chapter 3, polyethylene (PE) was the only polymer material used for radiative cooling convective covers partially because of its high transmittance in the IR. PE used for convective covers has typically been high purity virgin polymers because any impurities or contamination are sources of IR absorption. The work detailed in chapter 3 was the first to demonstrate that polymers with functional groups can be effective solar scattering convective covers despite intrinsically having higher absorption in the IR than PE. IR transmittance can be retained by reducing the thickness of the cover by carefully controlling the morphology and size distribution of the polymer fibers, or incorporating scattering particles as mentioned in 5.2. Using less polymer increases the tolerance of sources of absorption that can be present. As such, a study that uses recycled PE or biodegradable polymers is recommended to quantify the impurity tolerance necessary for convective covers. Using such materials can greatly reduce waste and the carbon footprint for global-scale applications where radiative cooling is deployed in large areas.

5.4 Cooling Solar Photovoltaic Arrays for Increased Efficiency and Lifetime

The average daytime ambient temperature at a representative U.S. Southwest location is ~25°C, while the average energy production temperature of the solar PV modules is ~49°C.[4] In such sunny

and dry locations, there is a need for PV thermal management. Decreasing the operating temperature of the modules has been shown to significantly improve both module efficiency (~0.4 %/°C) and module lifetime (~7 %/°C).[4] A passive approach to reduce the module operating temperature is to use radiative cooling; however, existing radiative cooling approaches have only demonstrated 1°C of additional temperature drop relative to a conventional glass-covered module.[5,6]

A potential solution is to pair a radiation-assisted PV thermal management system with solar panels to continuously maintain module temperatures near the average daytime ambient temperature (Fig. 5.3). This would be accomplished by using a solar scattering radiator[2] between the rows of solar arrays (Fig. 5.3a) and taking advantage of stored nighttime radiative cooling/convection using a ground-based shallow coolant reservoir (Fig. 5.3b). The radiator can provide an average cooling rate of 125 W/m^2 by emitting heat through the atmosphere's infrared (IR) transparency bands. It works in tandem with natural convection from the above-ambient modules, which provides an additional average cooling rate of ~160 W/m^2. Together, these two nearly continuous modes of heat transfer exceed the solar heat gain by the solar panels as long as excess nighttime cooling energy is stored in the coolant reservoir and circulated during the day.
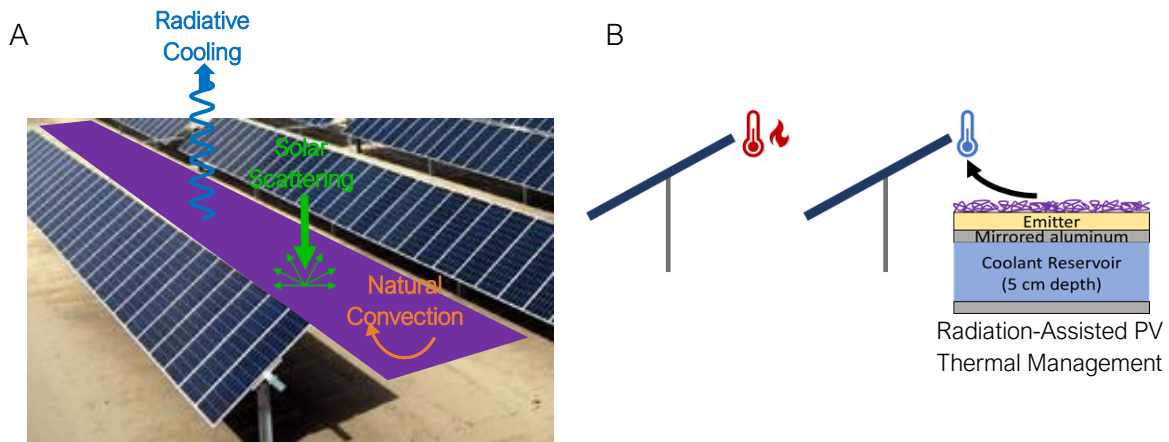
Figure 5.3. (A) The radiative cooling system would be deployed between the rows of solar arrays to cool the surrounding area and backside of the solar panels. (B) A reservoir used to store cooled liquid would provide sufficient cooling to the solar panels during the day.

In conclusion, the application space for passive radiative cooling is broad and growing. As society transitions into a renewable and sustainable future, ways to reduce and manage energy use are crucial to combat global warming. Ongoing and future work in understanding fundamental mechanisms that influence cooling performance, designing new systems with improved properties, and developing prototypes are all areas that affirm the potential impact of passive radiative cooling.

5.5 References

(1)   Kim, H.; Lenert, A. Optical and Thermal Filtering Nanoporous Materials for Sub-Ambient Radiative Cooling. *J. Opt.* **2018**, *20* (084002). https://doi.org/https://doi.org/10.1088/2040-8986/aacaa1.

(2)   Kim, H.; McSherry, S.; Brown, B.; Lenert, A. Selectively Enhancing Solar Scattering for Direct Radiative Cooling through Control of Polymer Nanofiber Morphology. *ACS Appl. Mater. Interfaces* **2020**, *12* (39), 43553–43559. https://doi.org/10.1021/acsami.0c09374.

(3)   Leroy, A.; Bhatia, B.; Kelsall, C. C.; Castillejo-Cuberos, A.; Di Capua, M. H.; Zhao, L.; Zhang, L.; Guzman, A. M.; Wang, E. N. High-Performance Subambient Radiative Cooling Enabled by Optically Selective and Thermally Insulating Polyethylene Aerogel. *Sci. Adv.* **2019**, *5* (eaat9480). https://doi.org/10.1126/sciadv.aat9480.

(4)   Dupré, O.; Vaillon, R.; Green, M. A. *Thermal Behavior of Photovoltaic Devices*; Springer, 2017.

(5)   Zhu, L.; Raman, A.; Wang, K. X.; Anoma, M. A.; Fan, S. Radiative Cooling of Solar Cells. *Optica* **2014**, *1* (1), 32–38. https://doi.org/10.1364/OPTICA.1.000032.

(6)   Li, W.; Shi, Y.; Chen, K.; Zhu, L.; Fan, S. A Comprehensive Photonic Approach for Solar Cell Cooling. *ACS Photonics* **2017**, *4* (4), 774–782. https://doi.org/10.1021/acsphotonics.7b00089.